

**FLUVIAL INFLUENCE ON ESTUARINE SEDIMENT
TRANSPORT PROCESSES AND LINKAGE OF ITS OUTFLOW
DATA TO COASTAL MODELING**

Josko Troselj

2016

**FLUVIAL INFLUENCE ON ESTUARINE SEDIMENT
TRANSPORT PROCESSES AND LINKAGE OF ITS OUTFLOW
DATA TO COASTAL MODELING**

河口土砂輸送過程に及ぼす河川の影響と海岸モデルへの河川流出情報の結合

by
Josko Troselj

A dissertation

**Submitted in partial fulfillment of the requirements for the
Degree of Doctor of Engineering**

Department of Civil and Earth Resources Engineering
Kyoto University, Japan

2016

Acknowledgements

The completion of my doctoral degree work have been demanding and life learning task which I encountered and enjoyed for the last 4 years during my stay in Takara's Laboratory. I will never forget the beautiful period of my life while I was a PhD student. I would like to acknowledge all the people and organizations who helped me on the way.

First and foremost, I would like to thank to my advisor, Professor Kaoru Takara who welcomed me in his lab and supported me all the way during the PhD degree study. He was taking care about my health and life conditions, visited me when I was in hospital and held birthday and welcome parties for me. He also provided me many chances to attend 7 international conferences and activities to communicate and study with other researchers and have employed me as Research Assistant in the Lab.

I would like to thank to Professor Yosuke Yamashiki for inviting me to study in Japan at first, and for providing me a great guidance to my research challenges. He helped me the most during my hospital days in Japan and visited me in hospital numerous times. I will be grateful to him for that forever. He was making conceptual ideas for my research, and I learned from him many lessons about how to do research.

I like to give my great gratitude to Associate Professor Takahiro Sayama for his extensive support to completion of my doctoral degree over the last year and a half. I always enjoyed fruitful discussion with him and great way of teaching that he has, always explaining even very complex matters on simple and understandable way.

I am grateful to Professor Yasuto Tachikawa for being my sub-supervisor and Thesis defense committee member and for giving me fruitful comments on the Thesis defense.

For help and assistance in many administrative and technical tasks I want to acknowledge DPRI and GCOE-ARS staff members, namely Ms. Sono Inoue, Mr. Shigeo Fujiki, Ms. Kaori Saidera, Ms. Mayumi Nishimura, Ms. Yoko Yonekawa, Ms. Yuko Takii and Ms. Saho Masuda. Because of them all my paperwork and translation from Japanese language during the doctoral course was much easier task.

I am grateful to Dr. PingPing Luo for all his help and assistance in personal and professional life, as well as to Associate Professors of GCOE-ARS Educational Unit Bin He and Masahito Ishihara, Assistant Professor Keisuke Himoto, Dr. Apip, Dr. Emmanuel Akpabio, Dr. Saima Riaz, Professor Ismail Abustan, Adjunct Associate Professor Nabsiah Abdul Wahid and Associate Professor Mahua Mukherjee.

I express my thanks to the Takara laboratory members and colleagues: Dr. Teramoto Tomoko, Dr. Nor Eliza Binti Alias, Dr. Weili Duan, Dr. Maja Ostric, Dr. Dang Quang

Khang, Dr. Bouhnieng Vilaysane, Dr. Maochuan Hu, Mr. Shota Kurokawa, Ms. Young-A Shin, Ms. Eunbi Kang, Ms. Maya Kusajima, Ms. Celia Namur, Ms. Juliane Laurendeau, Ms. Lina Kisolet Posanau, Mr. Masaki Azuma, Mr. Toshiharu Sasaki, Mr. Huy Loi Doan, Mr. Levu Antfalo, Ms. Pham Hong Nga, Ms. Chong Khain Lin, Ms. Eva Mia Siska, Ms. Shi Yongxue, Ms. Jamila Rajabi, Ms. Karlina, Mr. Han Xue, Mr. Hendy Setiawan, Mr. Pham Van Tien, Mr. Adnan Arutyunov, Mr. Shushuke Takahashi, Mr. Tsukasa Goto, Mr. Takuma Ushiro, Mr. Ryosuke Kobayashi, Mr. Kodai Yamamoto, Mr. Toma Stoyanov, Mr. Shoki Ono, Mr. Yohei Kurose, Mr. Shintaro Miyake and Mr. Yoshito Sugawara.

My deepest thanks goes to Associate Professor Shinichiro Kida for inviting me on two internships in JAMSTEC and for providing me a great training and continuous support during my study. He taught me a lot of my nowadays knowledge and I will be sincerely thankful to him for a lifetime. I also thank to Dr. Keiko Takahashi for accepting me to two internships as the Group Leader of Earth Simulation Center.

I am thankful to Mr. Christian Auel, Associate Professor Sameh Kantoush and Mr. Ryusuke Kuroki for providing great comments for Chapter 3 of the Thesis.

I gratefully acknowledge my Professors and colleagues from University of Rijeka, Croatia, where I was doing my Master of Engineering degree study. Among them, special mention goes to Professor Nevenka Ozanic, who recommended me for study in Japan through the project “Risk Identification and Land-Use Planning for Disaster Mitigation of Landslides and Floods in Croatia“, and professionally supported me during the study and when I was in hospital. I am also grateful to Professor Gordan Jelenic for his professional support and for his help and visits when I was in hospital. Special thanks is going to Mr. Nino Krvavica, for his extensive professional support in reviewing my academic papers and giving me fruitful comments for the study.

I would like to express my gratitude to the agencies and organizations which provided me financial support for the research. The Ministry of Education, Culture, Sports, Science and Technology of Japan (MEXT) for providing the scholarship for my studies and accommodation in Japan, GCOE-HSE program for giving me financial support to go to internships in JAMSTEC and to field work in University of Rijeka, to Takara Lab for supporting me to attend 7 domestic and international conferences, and to Kyoto University for granting me full tuition exemption for two semesters.

Finally, I want to thank to my family and friends, who were encouraging me to complete the doctoral course and who heartfully loved me. The biggest thanks to my parents Hermina and Nebojsa for their endless love and financial support, to girlfriend Eri Omura for wholeheartedly support and love, to Japanese father Akihiko Shimotani and to Japanese mother Reiko Shimada, who unfortunately passed away this year.

Abstract

Background

Nowadays, precipitation on the global scale is largely affected both by local and global climate change. Extreme precipitation increases its own value thus causing disastrous events to increase as well. The impact of disastrous events is significant in coastal zones, where runoff from the entire basin often reaches its peak.

Modeling of hydrodynamic and sediment transport processes in a contact zone between a river coming from potentially contaminated basin and an ocean is especially sensitive case for land-ocean coupling interaction due to significant risk of major environmental disaster which can occur in the case of contamination of the coastal zone. Therefore, it is of great importance to study and develop integrated modeling approach to comprehend the complex interaction processes in the contact zone in order to minimize disaster risk potential, which can consequently cause undesirable social and economical costs. Protection of the coastal environment in appropriate manner is important research field for engineers and thus integrated research is needed for better management of coastal environment, by providing better disaster risk management skills for both land and ocean environment.

The demand for having simulated freshwater outflow data on the river mouths is especially conspicuous in coastal modeling where fluvial influence often makes big difference in coastal salinity distribution results and in climatological modeling where fluvial influence is needed to join the oceanographic, meteorologic and hydrologic cycle into bigger comprehensive closed cycle to be used for more accurate climatological models.

Purpose

We gave more detailed insight into fate of sediment particles when they approach the interface layer between fluvial and oceanic water in order to better understand transportation mechanisms of pollutants in estuaries. The purpose of the theoretical concept and applied general ocean circulation numerical model MSSG is to show the application of vertically differentiated unidirectional freshwater flux dQ as useful for explaining the suspended sediment transport in the middle of the water column at the river mouth.

We simulated complete set of river outflow data from 9 first class Japanese river basins flowing from eastern Japanese coast to western Pacific ocean by using Cell

Distributed Runoff Model. The dataset can then be used by researchers dealing with Land-Ocean interaction. They can use it for developing joint hydrological-oceanographic models for modeling of estuarine and coastal processes, for developing more accurate climatological models where fluvial influence on the river mouth is needed to join the oceanographic, meteorologic and hydrologic cycle into bigger comprehensive closed cycle, and for developing accurate nowcasting models for real time prediction of extreme flood events for flood defense disaster prevention management.

Methodology

In chapter 3 we used z-leveled general ocean circulation numerical model MSSG solving incompressible Navier-Stokes equations to predict the flow field. The turbulent-sediment transporting flow was based on the observed turbidity data and joined with the model outputs by comparing the modeled dQ with both its theoretical concept and the observed turbidity quantities. We used the ETOPO1, 1 Arc Minute Global Relief Model for initial bathymetry conditions and the World Ocean Atlas 2005 for initial temperature and salinity data. The domain was discretized with rectangular 100×100 cells with 200 m resolution and 35 depth layers of 1 m resolution each, with model processing time increments of 10 seconds and output data time increments of 1 h from the start of the simulation. Horizontal domain was from 140.89E to 141.07E longitude and 37.96N to 38.14N latitude. The river outlet was 800 m wide and 7 m deep for high discharge and 6 m deep for low discharge. It was positioned in the central west point of the model from 140.89E to 140.92E, so the river channel was simulated to be 2.6 km long. Northern, southern and eastern boundaries were closed. At the beginning of the simulation the whole domain including the river channel was full of saltwater and afterwards freshwater is entering to the domain with constant unidirectional velocity v . We conducted two numerical simulations which correspond to extreme discharges phenomena, one with a high discharge of $Q = 5,600 \text{ m}^3/\text{s}$ with $v = 1 \text{ m/s}$ corresponding to high discharge from typhoon Roke, and one with low $v = 0.1 \text{ m/s}$ with $Q = 480 \text{ m}^3/\text{s}$.

In chapter 4 we have used cell distributed runoff model CDRMV version 3.1.1. We simulated numerical prediction of total freshwater outflow at river mouths from all of 9 first class river basins flowing from eastern Japanese coast to western Pacific ocean for targeted event typhoons Roke from 19/09/2011 at noon to 26/09/2011 at noon and Chataan from 8/07/2002 at noon to 15/07/2002 at noon. We neglected tidal effect from the calculation and observations. For Tone, Kitakami and Abukuma rivers we calculated dam effect using observed dam data, with conditions that if inflow to the dam is bigger than maximum observed outflow, then outflow from the dam becomes

maximum observed outflow. We assumed a uniform landuse because most of the area was covered by forest and its soil depth equals to 1000 mm. The other model parameters (soil roughness coefficient, river roughness coefficient, effective porosity, saturated hydraulic conductivity, effective rainfall) were optimized by using SCE-UA method. We optimized parameters based on typhoon Roke data and with validated with typhoon Chataan data and vice versa. We were searching which optimization (Roke or Chataan) shows better optimized and validated accuracy evaluation Nash-Sutcliffe (NS) coefficients.

We used JCOPE-T-NEDO model for joint hydrological-oceanographic modeling of coastal zone.

Results

The maximum dQ value is located in the river mouth vicinity in the middle of the water column due to the high discharge. The positive peak in the middle of the water column in the vicinity of river mouth is an extension of dQ peaks from lower layers of the water column. The internal interface shear layer acts as a boundary where sediment settling velocities decrease and therefore its concentration in upper columns increase. It is similar to place in the middle of the water column where was observed an unexpected peak in turbidity data. We did not explicitly show linkage of dQ and observed peak turbidity data, but their possible relation is theoretically discussed by using V_s and q_s as indicators of turbidity peaks. We assumed that, on depths where V_s is lower and q_s is higher, there should occur peaks of turbidity and showed that for our considered case it should be in the middle of water column in the vicinity of river mouth, because there dQ have its peak.

We showed total fluvial outflow (observed and simulated) and calibrated parameters for the best optimization during typhoon Roke and Chataan for each of 9 rivers in the scope of study, both for Roke calibration and Chataan validation and vice versa. Two coastal calculations were simulated by using joint hydrological-oceanographic model JCOPE-T-NEDO, one with using climatological mean monthly discharges as freshwater input from 9 rivers and the other one using our model simulated discharges as a real time freshwater input from 9 rivers. We could observe simulated significant difference of salinity in near-shore zone between the two cases, extending to almost the whole coast between Sendai bay and Tone river.

Conclusions

We conclude that dQ can be used to solve the mechanism for occurrence of the middle

water column turbidity peaks in a stratified estuary with occurrence of a stable salt wedge. Qualitatively, the suspended load peak should occur around the same place, which is supported by the theoretical fact that both $\partial v / \partial z$ and $\partial s / \partial z$ have its maximum in the middle of the water column for the given high discharge characteristic velocity and salinity profiles (Figure 3.4). This is, to our best knowledge, the first study discussing the possible linkage between hydrodynamic phase flow and suspended sediment phase flow by using dQ as the driving linkage mechanism. dQ is shown to be the driving mechanism for suspended sediment transport in the middle of the water column in vicinity of the river mouth, but its application is limited only to high discharge. Although we did not quantitatively solved the linkage between phases, we discussed meanings of dQ results and qualitatively approached theoretical governing mechanisms about how they may influence suspended sediment phase flow.

For total river outflow from all basins, calculated Nash-Sutcliffe efficiencies were very high, 0.985 for calibrated typhoon Roke and 0.858 for validated typhoon Chataan, which shows that our model calibrated on typhoon Roke can be successfully used to predict other extreme precipitation events runoff. Results for Chataan calibration and Roke validation came similar but with a little lower value. Effect of the dam for rivers Abukuma, Kitakami and Tone showed to be minor because dams are usually built in the upstream of the basins. This study included SCE-UA optimization method which significantly improved calibrated results. Our calibrated model can be used as nowcasting model for real time prediction of extreme flood events for flood defense disaster prevention management. The model used in the study has capability of simulating extreme discharge events by optimization, and proper simulation of extreme discharge events can be used to improve coastal and ocean modeling, especially modeling which is sensitive to reproducibility of the salinity distribution in coastal areas. By having ability to simulate extreme discharge events at river mouths, the study can be extended to sediment and water quality modeling in coastal areas.

Table of contents

Acknowledgements	i
Abstract	iii
Table of contents	vii
List of Tables	ix
List of Figures	xi
Chapter 1 - Introduction	- 1 -
Chapter 2 - Fluvial and sediment transport influence on modeling estuarine and coastal processes	- 3 -
2.1 Fluvial influence to estuarine sediment transport	- 3 -
2.2 Usage of total freshwater outflow data in coastal and climatological modeling	- 4 -
Chapter 3 - Linkage of vertically differentiated unidirectional salt flux and suspended sediment transport in the Abukuma river mouth	- 6 -
3.1 Estuarine mixing mechanisms and sediment transport rate	- 6 -
3.2 Numerical experiment setup	- 9 -
3.2.1 The ocean circulation numerical model	- 9 -
3.2.2. Simulation settings	- 10 -
3.3 Governing mechanism - theoretical concept	- 11 -
3.3.1 Hydrodynamic phase flow.....	- 11 -
3.3.2 Suspended sediment transport phase flow	- 14 -
3.4 Results and discussions	- 16 -
3.5 Conclusions	- 21 -
Chapter 4 - Total freshwater outflow from Japanese basins to western Pacific ocean	- 24 -
4.1 Significance of total freshwater outflow calculation in coastal and climatological modeling.....	- 24 -
4.2 Overview of Japanese basins on western Pacific ocean coast.....	- 28 -
4.3 Overview of cell distributed runoff model	- 32 -
4.4 Overview of SCE-UA optimum value search method	- 37 -

4.4.1 Calculation method	- 37 -
4.5 Observed discharge data from first class rivers	- 44 -
4.5.1 Takase river	- 44 -
4.5.2 Mabechi river	- 45 -
4.5.3 Kitakami river	- 46 -
4.5.4 Naruse river	- 48 -
4.5.5 Natori river	- 49 -
4.5.6 Abukuma river	- 50 -
4.5.7 Kuji river	- 51 -
4.5.8 Naka river	- 53 -
4.5.9 Tone river	- 54 -
4.6 Calculation conditions and methods	- 55 -
4.6.1 Initial data preparation	- 56 -
4.7 Results and discussions	- 76 -
4.7.1 Takase.....	- 76 -
4.7.2 Mabechi	- 78 -
4.7.3 Kitakami.....	- 81 -
4.7.4 Naruse	- 84 -
4.7.5 Natori.....	- 87 -
4.7.6 Abukuma	- 90 -
4.7.7 Kuji	- 93 -
4.7.8 Naka	- 96 -
4.7.9 Tone.....	- 99 -
4.7.10 Total outflow from all basins	- 102 -
4.7.11 Joint hydrological and oceanographic calculation.....	- 105 -
4.8 Conclusions	- 106 -
Chapter 5 - Conclusions and future challenges	- 110 -

List of Tables

Table 4.1	Calibrated parameters of the best optimization for typhoon Chataan	- 76 -
Table 4.2	Calibrated parameters of the best optimization for typhoon Roke	- 78 -
Table 4.3	Calibrated parameters of the best optimization for typhoon Chataan	- 79 -
Table 4.4	Calibrated parameters of the best optimization for typhoon Roke	- 81 -
Table 4.5	Calibrated parameters of the best optimization for typhoon Roke	- 82 -
Table 4.6	Calibrated parameters of the best optimization for typhoon Chataan	- 84 -
Table 4.7	Calibrated parameters of the best optimization for typhoon Roke	- 85 -
Table 4.8	Calibrated parameters of the best optimization for typhoon Chataan	- 87 -
Table 4.9	Calibrated parameters of the best optimization for typhoon Roke	- 88 -
Table 4.10	Calibrated parameters of the best optimization for typhoon Chataan	- 90 -
	-	
Table 4.11	Calibrated parameters of the best optimization for typhoon Roke....	- 91 -
Table 4.12	Calibrated parameters of the best optimization for typhoon Chataan	- 93 -
	-	
Table 4.13	Calibrated parameters of the best optimization for typhoon Roke ...	- 94 -
Table 4.14	Calibrated parameters of the best optimization for typhoon Chataan	- 96 -
	-	
Table 4.15	Calibrated parameters of the best optimization for typhoon Roke ...	- 97 -
Table 4.16	Calibrated parameters of the best optimization for typhoon Chataan	- 99 -
	-	
Table 4.17	Calibrated parameters of the best optimization for typhoon Roke .	- 100 -
Table 4.18	Calibrated parameters of the best optimization for typhoon Chataan ...	--

102 -

List of Figures

Figure 3.1 Field Observation points near Abukuma river mouth (Yamashiki et al., 2013)	- 8 -
Figure 3.2 Observed temperature, salinity and turbidity data over the water column at S1 (Yamashiki et al., 2013)	- 9 -
Figure 3.3 The free surface height and layer interface height near the river mouth. Solid lines show the sea surface, and dashed lines show the interface between the freshwater and seawater (Kida and Yamashiki, 2015)	- 11 -
Figure 3.4 Typical profiles over the water column, a)(up) velocity, b)(down) salinity. Profile in red, its derivative in green	- 12 -
Figure 3.5a Modeled results of $\partial v / \partial z$ for high unidirectional velocity $v = 1$ m/s, on 3 sections close to 140.92E river mouth (140.91E - green, 140.92E - black, 140.94E - red).....	- 13 -
Figure 3.5b Modeled results of $\partial s / \partial z$ for high unidirectional velocity $v = 1$ m/s, on 3 sections close to 140.92E river mouth (140.91E - green, 140.92E - black, 140.94E - red).....	- 14 -
Figure 3.6a Unidirectional salt flux $Q_{fw} = v*s$ [m/(s*psu)], on river mouth longitudinal.....	- 17 -
section 38.045N for $t = 8$ h; $v = 1$ m/s	- 17 -
Figure 3.6b Unidirectional salt flux $Q_{fw} = v*s$ [m/(s*psu)], on river mouth longitudinal.....	- 18 -
section 38.045N for $t = 80$ h; $v = 0.1$ m/s	- 18 -
Figure 3.7a Vertically differentiated unidirectional salt flux $dQ = \partial (v*s) / \partial z$ [m/(s*psu)/m'] on river mouth longitudinal section 38.045N for $t = 8$ hours; $v = 1$ m/s	- 19 -
Figure 3.7b Vertically differentiated unidirectional salt flux $dQ = \partial (v*s) / \partial z$ -	- 20 -
[m/(s*psu)/m'] on river mouth longitudinal section 38.045N for $t = 80$ hours; $v = 0.1$ m/s	- 20 -
Figure 4.1 Annual discharge from each coastal box [1000 m ³ /s] (Dai and Trenberth, 2003)	- 25 -
Figure 4.2 Discharge trends 1951 - 2000 for 137 global rivers (Millman et al., 2008)	- 27 -
Figure 4.3 Mean annual combined runoff field (Fekete et al., 2002).....	- 28 -

Figure 4.4 Map of targeted 9 first class Japanese river basins flowing to western Pacific ocean (ArcGis, World Imagery)	- 29 -
Figure 4.5 Northeastern Japanese Pacific coast with Takase and Mabechi rivers (http://www1.river.go.jp/)	- 30 -
Figure 4.6 Sendai bay with Kitakami, Naruse, Natori and Abukuma rivers (http://www1.river.go.jp/)	- 31 -
Figure 4.7 Southeastern Japanese Pacific coast with Kuji, Naka and Tone rivers (http://www1.river.go.jp/)	- 32 -
Figure 4.8 Conceptual diagram of the cell distributed runoff model (Kojima et al., 1998)	- 35 -
Figure 4.9 Structure of the assumed soil layer (Tachikawa et al., 2004)	- 36 -
Figure 4.10 Function form of the flow stream product relationship (Tachikawa et al., 2004)	- 36 -
Figure 4.11 Model system of SCE-UA algorithm	- 41 -
Figure 4.12 CCE Model system of algorithms	- 42 -
Figure 4.13 SCE-UA Function value transition diagram according to algorithm-	43
-	
Figure 4.14 CCE Function value transition diagram according to algorithm	- 43 -
Figure 4.15 Water level and discharge data for Takasegawa station, Takase river..	- 45 -
Figure 4.16 Water level and discharge data for Bridge station, Mabechi river..	- 46 -
Figure 4.17 Water level and discharge data for Tome station, Kitakami river ..	- 47 -
Figure 4.18 Water level and discharge data for Nobiru 1 station, Naruse river	- 49 -
Figure 4.19 Water level and discharge data for Yuriage 2 station, Natori river	- 50 -
Figure 4.20 Water level and discharge data for Iwanuma station, Abukuma river..	- 51 -
Figure 4.21 Water level and discharge data for Sakaki bridge station, Kuji river-	52
-	
Figure 4.22 Water level and discharge data for Suifu bridge station, Naka river-	53
-	
Figure 4.23 Water level and discharge data for Nunokawa station, Tone river .	- 54 -
Figure 4.24 Delineated Flow Accumulation data, with position of rainfall stations (blue dots) with belonging Thiessen polygons and observation station Ueno (red dot) for the Takase basin.....	- 58 -
Figure 4.25 Digital Elevation Model (DEM) for the Takase basin (460 m resolution)	- 59 -

Figure 4.26 Delineated Flow Direction map for the Takase basin	- 59 -
Figure 4.27 Delineated Flow Accumulation data, with position of rainfall stations (blue dots) with belonging Thiessen polygons and observation station Bridge (red dot) for the Mabechi basin	- 60 -
Figure 4.28 Digital Elevation Model (DEM) for the Mabechi basin (460 m resolution)	- 61 -
Figure 4.29 Delineated Flow Direction map for the Mabechi basin	- 61 -
Figure 4.30 Delineated Flow Accumulation data, with position of rainfall stations (blue dots) with belonging Thiessen polygons and observation stations Tome and Wabuchi (red dots) for the Kitakami basin	- 62 -
Figure 4.31 Digital Elevation Model (DEM) for the Kitakami basin (460 m resolution)	- 63 -
Figure 4.32 Delineated Flow Direction map for the Kitakami basin	- 63 -
Figure 4.33 Delineated Flow Accumulation data, with position of rainfall stations (blue dots) with belonging Thiessen polygons and observation stations Noda and Hataya (red dots) for the Naruse basin.....	- 64 -
Figure 4.34 Digital Elevation Model (DEM) for the Naruse basin (460 m resolution)	- 65 -
Figure 4.35 Delineated Flow Direction map for the Naruse basin	- 65 -
Figure 4.36 Delineated Flow Accumulation data, with position of rainfall stations (blue dots) with belonging Thiessen polygons and observation stations Natoribashi and Hirosebashi (red dots) for the Natori basin	- 66 -
Figure 4.37 Digital Elevation Model (DEM) for the Natori basin (460 m resolution)- 67 -	
Figure 4.38 Delineated Flow Direction map for the Natori basin	- 67 -
Figure 4.39 Delineated Flow Accumulation data, with position of rainfall stations (blue dots) with belonging Thiessen polygons and observation station Iwanuma (red dot) for the Abukuma basin.	- 68 -
Figure 4.40 Digital Elevation Model (DEM) for the Abukuma basin (460 m resolution)	- 69 -
Figure 4.41 Delineated Flow Direction map for the Abukuma basin	- 69 -
Figure 4.42 Delineated Flow Accumulation data, with position of rainfall stations (blue dots) with belonging Thiessen polygons and observation station Sakaki bridge (red dot) for the Kuji basin.....	- 70 -
Figure 4.43 Digital Elevation Model (DEM) for the Kuji basin (460 m spatial resolution)	- 71 -

Figure 4.44 Delineated Flow Direction map for the Kuji basin	- 71 -
Figure 4.45 Delineated Flow Accumulation data, with position of rainfall stations (blue dots) with belonging Thiessen polygons and observation station Suifu bridge (red dot) for the Naka basin.....	- 72 -
Figure 4.46 Digital Elevation Model (DEM) for the Naka basin (460 m resolution). -	73 -
Figure 4.47 Delineated Flow Direction map for the Naka basin	- 73 -
Figure 4.48 Delineated Flow Accumulation data, with position of rainfall stations (blue dots) with belonging Thiessen polygons and observation station Nunokawa (red dot) for the Tone basin.....	- 74 -
Figure 4.49 Digital Elevation Model (DEM) for the Tone basin (460 m spatial resolution)	- 75 -
Figure 4.50 Delineated Flow Direction map for the Tone basin	- 75 -
Figure 4.51 Calibrated results for typhoon Chataan (8/07/2002 13:00 - 15/07/2002 12:00).....	- 76 -
Figure 4.52 Validated results for typhoon Roke (19/09/2011 13:00 - 26/09/2011 12:00).....	- 77 -
Figure 4.53 Calibrated results for typhoon Roke (19/09/2011 13:00 - 26/09/2011 12:00).....	- 77 -
Figure 4.54 Validated results for typhoon Chataan (8/07/2002 13:00 - 15/07/2002 12:00).....	- 78 -
Figure 4.55 Calibrated results for typhoon Chataan (8/07/2002 13:00 - 15/07/2002 12:00).....	- 79 -
Figure 4.56 Validated results for typhoon Roke (19/09/2011 13:00 - 26/09/2011 12:00).....	- 80 -
Figure 4.57 Calibrated results for typhoon Roke (19/09/2011 13:00 - 26/09/2011 12:00).....	- 80 -
Figure 4.58 Validated results for typhoon Chataan (8/07/2002 13:00 - 15/07/2002 12:00).....	- 81 -
Figure 4.59 Calibrated results for typhoon Roke (19/09/2011 13:00 - 26/09/2011 12:00).....	- 82 -
Figure 4.60 Validated results for typhoon Chataan (8/07/2002 13:00 - 15/07/2002 12:00).....	- 83 -
Figure 4.61 Calibrated results for typhoon Chataan (8/07/2002 13:00 - 15/07/2002 12:00).....	- 83 -
Figure 4.62 Validated results for typhoon Roke (19/09/2011 13:00 - 26/09/2011	

12:00).....	- 84 -
Figure 4.63 Calibrated results for typhoon Roke (19/09/2011 13:00 - 26/09/2011	
12:00).....	- 85 -
Figure 4.64 Validated results for typhoon Chataan (8/07/2002 13:00 - 15/07/2002	
12:00).....	- 86 -
Figure 4.65 Calibrated results for typhoon Chataan (8/07/2002 13:00 - 15/07/2002	
12:00).....	- 86 -
Figure 4.66 Validated results for typhoon Roke (19/09/2011 13:00 - 26/09/2011	
12:00).....	- 87 -
Figure 4.67 Calibrated results for typhoon Roke (19/09/2011 13:00 - 26/09/2011	
12:00).....	- 88 -
Figure 4.68 Validated results for typhoon Chataan (8/07/2002 13:00 - 15/07/2002	
12:00).....	- 89 -
Figure 4.69 Calibrated results for typhoon Chataan (8/07/2002 13:00 - 15/07/2002	
12:00).....	- 89 -
Figure 4.70 Validated results for typhoon Roke (19/09/2011 13:00 - 26/09/2011	
12:00).....	- 90 -
Figure 4.71 Calibrated results for typhoon Roke (19/09/2011 13:00 - 26/09/2011	
12:00).....	- 91 -
Figure 4.72 Validated results for typhoon Chataan (8/07/2002 13:00 - 15/07/2002	
12:00).....	- 92 -
Figure 4.73 Calibrated results for typhoon Chataan (8/07/2002 13:00 - 15/07/2002	
12:00).....	- 92 -
Figure 4.74 Validated results for typhoon Roke (19/09/2011 13:00 - 26/09/2011	
12:00).....	- 93 -
Figure 4.75 Calibrated results for typhoon Roke (19/09/2011 13:00 - 26/09/2011	
12:00).....	- 94 -
Figure 4.76 Validated results for typhoon Chataan (8/07/2002 13:00 - 15/07/2002	
12:00).....	- 95 -
Figure 4.77 Calibrated results for typhoon Chataan (8/07/2002 13:00 - 15/07/2002	
12:00).....	- 95 -
Figure 4.78 Validated results for typhoon Roke (19/09/2011 13:00 - 26/09/2011	
12:00).....	- 96 -
Figure 4.79 Calibrated results for typhoon Roke (19/09/2011 13:00 - 26/09/2011	
12:00).....	- 97 -
Figure 4.80 Validated results for typhoon Chataan (8/07/2002 13:00 - 15/07/2002	

12:00)	- 98 -
Figure 4.81 Calibrated results for typhoon Chataan (8/07/2002 13:00 - 15/07/2002	
12:00)	- 98 -
Figure 4.82 Validated results for typhoon Roke (19/09/2011 13:00 - 26/09/2011	
12:00)	- 99 -
Figure 4.83 Calibrated results for typhoon Roke (19/09/2011 13:00 - 26/09/2011	
12:00)	- 100 -
Figure 4.84 Validated results for typhoon Chataan (8/07/2002 13:00 - 15/07/2002	
12:00)	- 101 -
Figure 4.85 Calibrated results for typhoon Chataan (8/07/2002 13:00 - 15/07/2002	
12:00)	- 101 -
Figure 4.86 Validated results for typhoon Roke (19/09/2011 13:00 - 26/09/2011	
12:00)	- 102 -
Figure 4.87 Calibrated results for typhoon Roke (19/09/2011 13:00 - 26/09/2011	
12:00)	- 103 -
Figure 4.88 Validated results for typhoon Chataan (8/07/2002 13:00 - 15/07/2002	
12:00)	- 103 -
Figure 4.89 Calibrated results for typhoon Chataan (8/07/2002 13:00 - 15/07/2002	
12:00)	- 104 -
Figure 4.90 Validated results for typhoon Roke (19/09/2011 13:00 - 26/09/2011	
12:00)	- 104 -
Figure 4.91a Sea surface salinity (PSU) in JCOPE-T model for September 26, 2011,	
22:00 JST (climatological monthly discharges).....	- 105 -
Figure 4.91b Sea surface salinity (PSU) in JCOPE-T model for September 26, 2011,	
22:00 JST (our model discharges)	- 106 -

Chapter 1 - Introduction

Nowadays, precipitation on the global scale is largely affected both by local and global climate changes. Extreme precipitation increases its own value thus causing disastrous events to increase as well. The impact of disastrous events is significant in coastal zones, where runoff from the entire basin often reaches its peak.

Modeling of hydrodynamic and sediment transport processes in a contact zone between a river coming from potentially contaminated basin and an ocean is especially sensitive case for land-ocean coupling interaction due to significant risk of major environmental disaster which can occur in the case of contamination of the coastal zone. Therefore, it is of great importance to study and develop integrated modeling approach to comprehend the complex interaction processes in the contact zone in order to minimize disaster risk potential, which can consequently cause undesirable social and economical costs.

An important issue is the sediment production from the mountain zone, which directly affects the downstream area through potential sediment deposit and flood disaster risk as well as marine environment near the outlet of a river and surrounding coastal zone, by affecting salinity and both mineral and nutrient production.

Protection of the coastal environment in appropriate manner is important research field for engineers and thus integrated research is needed for better management of coastal environment, by providing better disaster risk management skills for both land and ocean environment. This is especially important in cases of radionuclide pollution due to its high impact on environment and consequently on humans, as well as very long half-life duration of its activity, in comparing with other pollution sources.

Chapter 2 introduces fluvial and sediment transport influence on modeling estuarine and coastal processes. It describes significance of research and scientific motivation by reviewing other authors' researches in related field and their conclusions.

In chapter 3 we give more detailed insight into fate of sediment particles when they approach the interface layer between fluvial and oceanic water in order to better understand transportation mechanisms of pollutants in estuaries. The purpose of the theoretical concept and applied general ocean circulation numerical model MSSG is to show the application of vertically differentiated unidirectional freshwater flux dQ as useful for explaining the suspended sediment transport in the middle of the water column at the river mouth. It is used as a link between hydrodynamic phase and

suspended sediment transport phase in strongly stratified estuaries as a consequence of fluvial forcing during high discharge in combination with stable salt wedge formation. We suggest that for highly stratified estuaries where a stable salt wedge forms, peak suspended load transport rate will take place in river mouth vicinity on the internal interface shear layer between fluvial and oceanic water. The reason for that is that dQ has its maximum at that depth. Although we did not quantitatively solve the linkage between phases, we discussed meanings of dQ results and qualitatively approached theoretical governing mechanisms about how they may influence suspended sediment phase flow.

In chapter 4 we simulate complete set of river outflow data from 9 first class Japanese river basins flowing from eastern Japanese coast to western Pacific ocean by using Cell Distributed Runoff Model. The dataset can then be used by researchers dealing with Land-Ocean interaction. They develop joint hydrological-oceanographic models for modeling of estuarine and coastal processes, for developing more accurate climatological models where fluvial influence on the river mouth is needed to join the oceanographic, meteorology and hydrology cycle into bigger comprehensive closed cycle, and for developing accurate nowcasting models for real time prediction of extreme flood events for flood defense disaster prevention management. At the end of the chapter our simulated river outflow dataset was joined together with coastal simulation using JCOPE-T model so we could see real influence of our data to salinity reproducibility in coastal zone of the eastern Japanese coast after the typhoon Roke.

In chapter 5 we conclude our thesis, giving discussion about connections between chapters 3 and 4 and their mutual conclusions, as well as discussing future challenges and opportunities following the contents from the thesis.

Chapter 2 - Fluvial and sediment transport influence on modeling estuarine and coastal processes

2.1 Fluvial influence to estuarine sediment transport

An estuary is defined as "any embayment of the coast in which buoyancy forcing alters the fluid density from that of adjoining ocean" (Geyer and MacGready, 2014). In estuaries, sediment transport mechanisms driven by fluvial influence shows much different characteristics than in other fluvial environments. It needs to take into account influences from several different disciplines, including hydrodynamic, meteorological, biological and chemical influence. Turbulent mixing of salt and freshwater in estuaries influences salinity intrusion, stratification and biological and chemical components of estuary (Ralston et al., 2010), and also have significant impact on sediment dynamics within the estuary. The dynamics of estuarine sediment transport depends on water circulation, salinity concentration, biological and chemical interaction and type of sediment. An example of biological and chemical interaction is phenomenon typical for estuaries called flocculation, which occurs when cohesive sediments aggregate forming flocs of typical sizes of 100-200 μ m. Flocculated sediment particles have faster settling velocities due to their multiplied mass and are therefore an ongoing challenge for solving in hydrodynamic models. The density contrast between freshwater and saltwater is important factor governing estuarine and coastal circulation (Geyer et al., 2004). One of the most important phenomena for sediment trapping in estuaries is bottom convergence which often traps sediment at the most furthest point of salinity intrusion in the estuary (Geyer et al., 2004). Aggregation, settling, trapping and resuspension occurring in estuaries are major factors influencing different mechanisms of suspended sediment transport occurring there than in other fluvial environments.

Estuarine environment is very diverse and thus complicated for research, with especially hard task for researchers of making adequate parameterization in physical modeling (Geyer and MacGready, 2014). Unlike circulation in other natural environments, the estuarine circulation does not critically depend on discharge or tidal amplitudes but rather "on the relative balance among fluvial, tidal and baroclinic forcing" (Ralston et al., 2010). The relative balance among buoyancy, turbulent mixing and density gradient between fresh and salt water are specific quantities for estuaries which have major influence for estuarine circulation and mechanisms for suspended

sediment transport. Interplay among estuarine circulation, tidally averaged transport and salt flux plays a fundamental role in determining characteristics of an estuary. Fluxes near bottom and shear induced fluxes are often more dominant for the sediment transport in fluvial and estuarine environments than the surface fluxes (Geyer et al., 2004). Another quantity essentially important for estuarine suspended sediment transport is vertical mixing within the estuary. If vertical mixing is weak, less sediments reach the bottom and get adsorbed to bottom sediments. The exchange flow occurring in estuaries effectively traps particles that sink causing high sediment accumulation rates.

The radionuclide pollution coming from the Abukuma river basin can consequently cause other disasters, such as degradation of marine environment quality, flora and fauna and consequently have influence to human health and potential bigger disasters.

2.2 Usage of total freshwater outflow data in coastal and climatological modeling

The demand for having simulated freshwater outflow data on the river mouths is especially conspicuous in coastal modeling where fluvial influence often makes big difference in results and in climatological modeling where fluvial influence is needed to join the oceanographic, meteorology and hydrology cycle into bigger comprehensive closed cycle to be used for more accurate climatological models. The major obstacles in estimating continental discharge are incomplete or unmonitored discharge or water level data. Milliman et al. (2008) reported that the number of river gauging station in higher latitudes is in decreasing trend, just when continuity in long-term data is most needed. It is therefore useful to update and improve continental discharge estimates datasets and provide useful data for climate model evaluations.

On top of complex physical processes occurring close to river mouths, the appropriate model representation challenge is an additional issue to hydrodynamic and climate modeling experts. For numerically representing time dependent salinity field, we need to solve mechanism of tidal and subtidal motions and turbulence closure scheme (Warner et al., 2005).

It is important to include river flow in climate models so that climate modelers can compare their hydrologic model outputs with observed gauging stations. (Miller et al., 1994). It can also help to climate modelers to develop comprehensive hydrodynamic, meteorology and hydrology models where the global hydrologic cycle is closed. When

climate models are able to simulate river flow for the present climate more accurately, they can then be used to examine potential changes in response to climate change. Climate models could also be used for prediction of sediment transport and chemical constituents in fluvial environments (Miller et al., 1994).

References

- Geyer WR, Hill PS, Kineke GC. 2004. The transport, transformation and dispersal of sediment by buoyant coastal flows, *Continental Shelf Research* 24, pp. 927-949. Doi: 10.1016/j.csr.2004.02.006..
- Geyer WR, MacGready P. 2014. The estuarine circulation, *Annual Review of Fluid Mechanics* 46, pp. 175-197. Doi: 10.1146/annurev-fluid-010313-141302.
- Miller JR, Russel GL, Caliri G. 1994. Continental-scale river flow in climate models, *Journal of climate*.
- Milliman JD, Farnsworth KL, Jones PD, Xu KH, Smith LC. 2008. Climatic and anthropogenic factors affecting river discharge to the global ocean, 1951-2000, *Global and planetary change* 62 (3-4), pp. 187-194.
- Ralston DK, Geyer WR, Lerczak JA. 2010. Structure, Variability, and salt flux in a strongly forced salt wedge estuary, *Journal of Geophysical Research* 115, C06005. Doi: 10.1029/2009JC005806.
- Warner JC, Geyer WR, Lerczak JA. 2005. Numerical modeling of an estuary: A comprehensive skill assessment, *Journal of Geophysical Research* Vol. 110, C05001. Doi: 1029/2004JC002691.

Chapter 3 - Linkage of vertically differentiated unidirectional salt flux and suspended sediment transport in the Abukuma river mouth

3.1 Estuarine mixing mechanisms and sediment transport rate

An important issue for estuarine and coastal modeling is the sediment production from a river basin. The sediment production directly affects the downstream area through potential sediment deposit and flood disaster risk as well as marine environment near the outlet of a river and surrounding coastal zone. The sediment production also affects salinity and both mineral and nutrient production. Kida and Yamashiki (2015) stated that several years of sediment deposits can sometimes be transported during only one extreme discharge event. Sediment transport does not follow the same route like freshwater flow due to aggregation and sediment settling (Geyer et al., 2004).

The paper deals with fluvial and sediment transport influences on estuarine and coastal processes. Estuarine processes are very complicated to research because of mutual interactions between freshwater and saltwater, as well as many other factors occurring as a consequence of those interactions. In estuarine environment, the buoyancy frequency and dissipation rate are dominant effects among other factors (Geyer et al., 2008). Regardless the recent progresses in sediment transport studies in estuaries and coastal zones, we are still far away from having a capability to successfully predict sediment transport routes and deposition mechanisms (Geyer et al., 2004). The interplay among buoyancy, turbulent mixing and density gradient between freshwater and saltwater influences parameters such as salinity intrusion or stratification (Ralston et al., 2010a). The buoyancy flux, which increases horizontal density and pressure gradient, and turbulent mixing are two major processes influencing hydrodynamic and sediment transport processes in estuaries (Geyer and MacGready, 2014). Vertical mixing determines the exchange flow, the stratification and residence time of water in estuaries (Geyer et al., 2008). Estuarine turbulence greatly increases vertical transport and affects the distribution of sediments and dynamical quantities of momentum and buoyancy (MacDonald and Geyer, 2004). Warner et al. (2005) defined estuarine circulation, tidally averaged transport and salt flux as a fundamental quantities defining an estuary. There is at least four stages of sediment transport seaward of river mouth: transport by plumes, initial deposition, resuspension

and long term accumulation (Wright and Nittrouer, 1995). Although the neglect of tides limits the direct application of Geyer's simple model (Geyer, 1993) to actual estuaries, it allows the specific mechanism of turbulence suppression by stratification to be isolated. We will also neglect tidal effect in the paper for similar reasons.

Some studies dealt with various estuarine processes affecting sediment transport, such as vertical mixing, buoyancy flux, return flow, resuspension, estuarine circulation (Ralston et al., 2010b, Waner et al., 2005, Geyer et al., 2004). However, there are a few previous studies about sediment transport processes on the internal interface shear layer between freshwater and saltwater in the vicinity of river mouth. Ralston et al. (2010b) found that the concentration of suspended sediment is maximum at the interface but they did not explain the mechanism of the suspended sediment peak. The Peak concentration of suspended sediments are usually trapped near the estuarine limit of the salinity intrusion (Ralston and Stacey, 2007). The salinity field within the estuary is dependent on buoyancy flux, advection by tides, estuarine circulation and vertical mixing (Warner et al., 2005). It consequently affects sediment transport mechanism. "In strongly stratified estuaries and plumes where internal shear mixing was the dominant source of buoyancy flux, the flux Richardson number R_f approached maximum values" (Ralston et al., 2010b). Ralston et al. (2010b) found that when R_f , as a ratio between buoyancy flux and shear production, approaches its maximum values while internal shear mixing is the dominant source of buoyancy flux, then buoyancy flux increases its value a lot more than shear production value. Consequently, members of the formula for buoyancy flux become much bigger than members of the formula for shear production.

Based on field observations on 20 March 2013, distributions of radionuclides, salinity, temperature and turbidity near the Abukuma river mouth were observed (Yamashiki et al., 2013) (Figure 1). They found an unexpected vertical turbidity distribution and it showed peaks 500 m downstream of the river mouth towards the ocean at depths that correspond to the middle river water column, while freshwater inflow at those depths was not simultaneously observed. Nevertheless, the mechanism of those unexpected peaks was not explained in their study.

The objective of this study is to give more detailed insight into fate of sediment particles when they approach the interface layer between fluvial and oceanic water in order to better understand transportation mechanisms of pollutants in estuaries. The purpose of this theoretical concept and applied z-leveled general ocean circulation numerical model MSSG (Kida, 2011) is to show the application of dQ as useful for explaining the suspended sediment transport in the middle of the water column at the

river mouth. It is used as a link between hydrodynamic phase and suspended sediment transport phase in strongly stratified estuaries as a consequence of fluvial forcing during high discharge in combination with stable salt wedge formation (hereafter referred as "high discharge"). We considered suspended sediment peak found near the estuarine limit of the salinity intrusion, and qualitatively described newly introduced hydrodynamic mechanism, vertically differentiated unidirectional salt flux dQ , as an indicator for finding such a peak in the middle of the water column in vicinity of the river mouth. We tried to find the specific mechanism which led to the observed peak of turbidity on station 1 at a depth of 4.5 m, while freshwater intrusion was not observed at the same depth (Yamashiki et al., 2013) (Figure 2). Salt wedge estuaries, which are estuaries with high density stratification, are occurring in microtidal environments with high river discharges which successfully maintains the stratification (Dyer, 1973). The study site is the estuary zone affected by the river inflow and associated sediment transport from the Abukuma river basin in Japan.

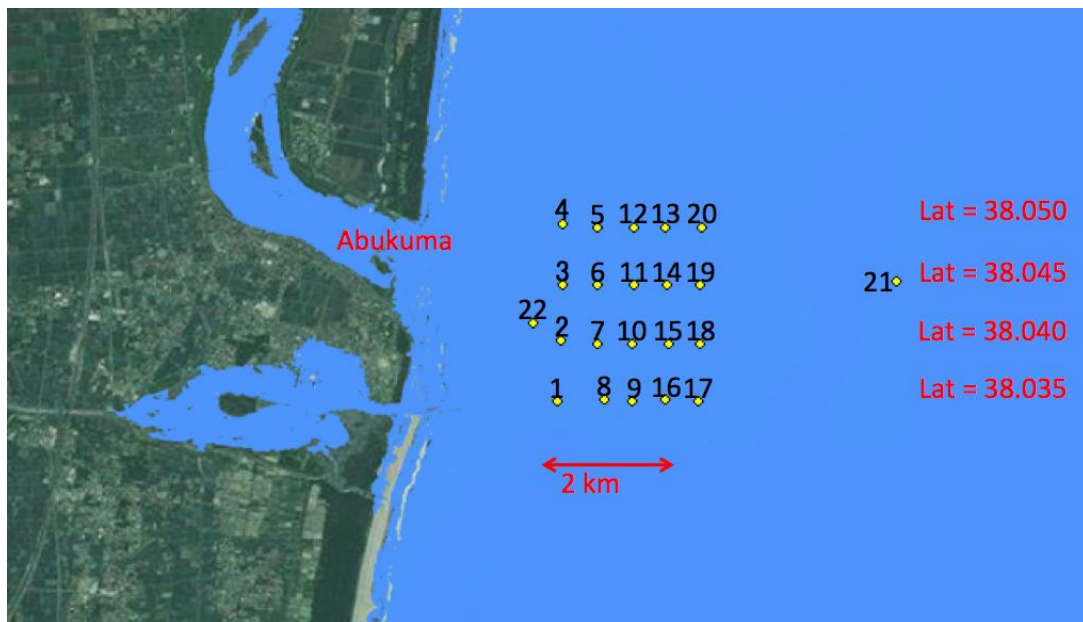


Figure 3.1 Field Observation points near Abukuma river mouth (Yamashiki et al., 2013)

Our hypothesis is that for highly stratified estuaries where a stable salt wedge forms, peak suspended load transport rate will take place in river mouth vicinity on the internal interface shear layer between fluvial and oceanic water. We expect that dQ will have the maximum value at that depth for given high discharge conditions and that maximum of suspended load transport rate will consequently be occurring around the same depth.

3.2 Numerical experiment setup

3.2.1 The ocean circulation numerical model

We used z-leveled general ocean circulation numerical model MSSG solving incompressible Navier-Stokes equations to predict the flow field. The turbulent-sediment transporting flow was based on the observed turbidity data (Figure 3.2) and joined with the model outputs by comparing the modeled dQ with both its theoretical concept and the observed turbidity quantities.

As our major intention was to consider influence of fluvial inflow towards the ocean, we defined various boundary conditions mostly from the river side and only briefly from the ocean in order to find an oceanic response to diverse fluvial conditions. Major emphasis was put on diverse hydrodynamic processes during rising limb stage of an extreme fluvial discharge event, with the biggest focus on high discharge. We also modeled a low discharge case and compared the results with a high discharge case.

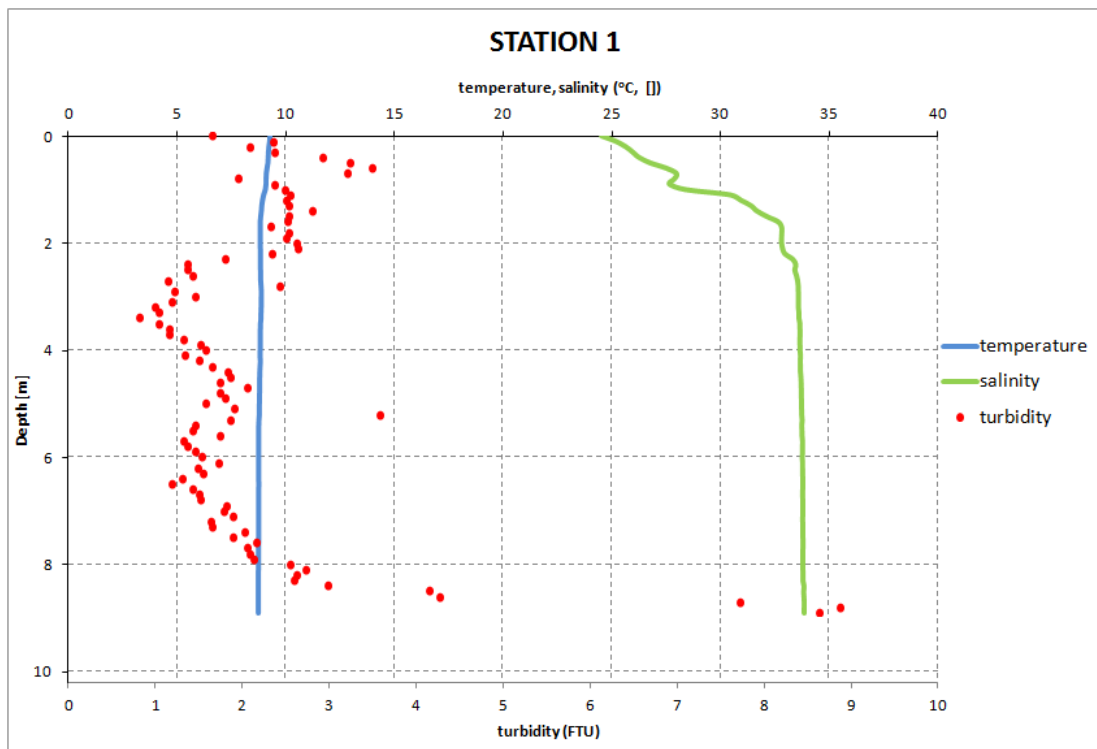


Figure 3.2 Observed temperature, salinity and turbidity data over the water column at S1 (Yamashiki et al., 2013)

3.2.2. Simulation settings

We used the ETOPO1 (Amante and Eakins, 2009), 1 Arc Minute Global Relief Model for initial bathymetry conditions and the World Ocean Atlas 2005 (NODC, 2007) for initial temperature and salinity data. The domain was discretized with rectangular 100×100 cells with 200 m resolution and 35 depth layers of 1 m resolution each, with model processing time increments of 10 seconds and output data time increments of 1 h from the start of the simulation. Horizontal domain was from 140.89E to 141.07E longitude and 37.96N to 38.14N latitude. The river outlet was 800 m wide and 7 m deep for high discharge and 6 m deep for low discharge. It was positioned in the central west point of the model from 140.89E to 140.92E, so the river channel was simulated to be 2.6 km long. The middle of the river channel was placed at 38.045N latitude, which corresponds to the position where all modeled results will be shown. Northern, southern and eastern boundaries were closed. At the beginning of the simulation the whole domain including the river channel was full of saltwater and afterwards freshwater is entering to the domain with constant unidirectional velocity v . Thus, the simulation needed some time to obtain realistic results, defined as the time from the beginning of the simulation until equilibrium state establishment between saltwater and incoming freshwater.

We focused the study on typhoon Roke in September 2011, where estimated 61% of total radiocesium load was being exported from the river basin (Yamashiki et al., 2014). In particular, we focused on two different discharges during the typhoon Roke (Figure 3.3), a low from September 19 (red lines) and a high one from September 21 (blue lines). The movement of the interface between the freshwater and seawater near the river mouth is well captured in Figure 3.3 (Kida and Yamashiki, 2015). We conducted two numerical simulations which correspond to extreme discharges phenomena (Figure 3.3), one with a high discharge of $Q = 5.600 \text{ m}^3/\text{s}$ with $v = 1 \text{ m/s}$ corresponding to high discharge from typhoon Roke, and one with low $v = 0.1 \text{ m/s}$ with $Q = 480 \text{ m}^3/\text{s}$.

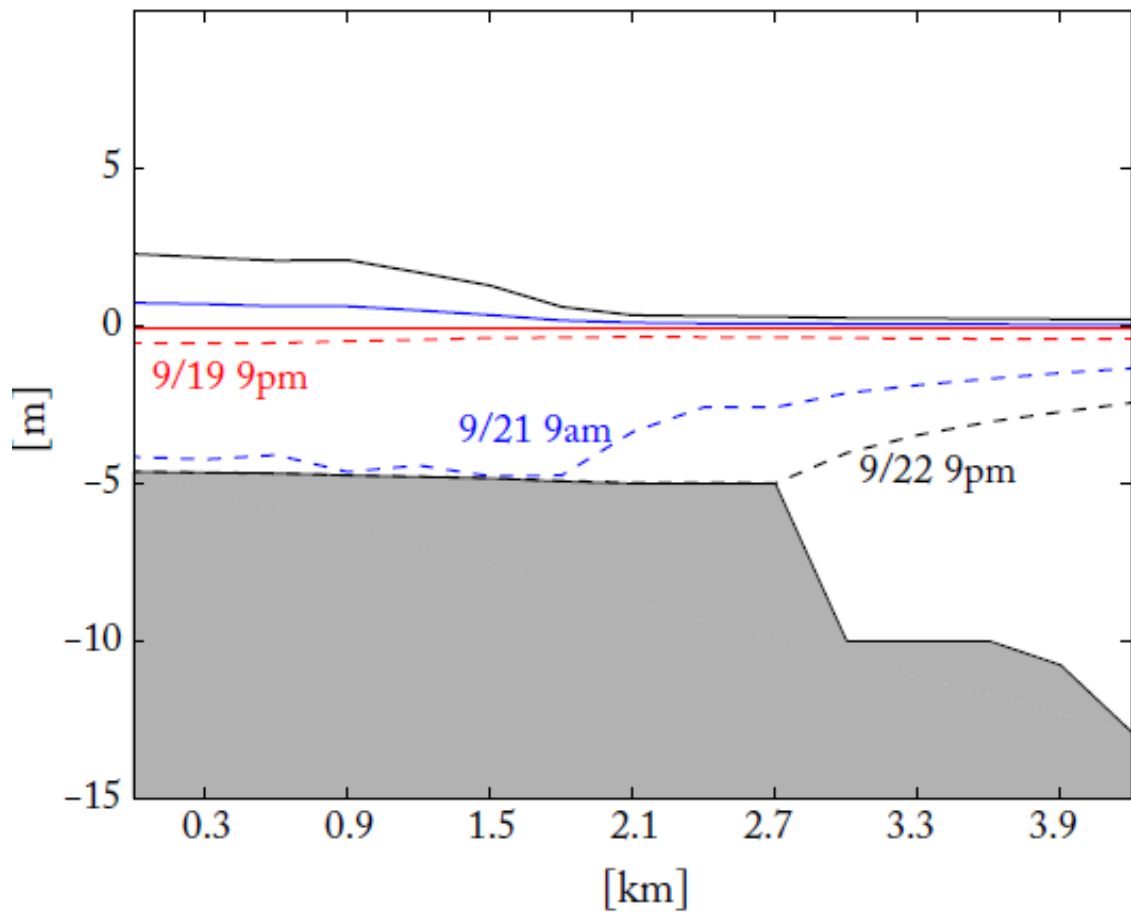


Figure 3.3 The free surface height and layer interface height near the river mouth. Solid lines show the sea surface, and dashed lines show the interface between the freshwater and seawater (Kida and Yamashiki, 2015)

3.3 Governing mechanism - theoretical concept

3.3.1 Hydrodynamic phase flow

dQ may be expressed as vertical derivation of the unidirectional salt flux $Q_{fw} = (vs)$ as:

$$dQ = \frac{\partial(vs)}{\partial z} \quad (3.1)$$

where s = salinity and z = vertical direction perpendicular to the bed, positive in downward direction. The theoretical concept for introducing that parameter will be explained in the following using its basic terms $\partial v / \partial z$ and $\partial s / \partial z$. We plotted typical profiles of velocity and salinity for high and low discharges, from which we derived $\partial v /$

∂z and $\partial s/\partial z$. We drew some conclusions of their meaning as well as a qualitative linking with the suspended sediment transport. Figure 3.4 shows typical velocity (a) and salinity (b) profiles and its derivatives with respect to z for high discharge, which correspond to values when a stable salt wedge begins to form and higher.

In order to see magnitudes of $\partial v/\partial z$ and $\partial s/\partial z$ peaks from Figure 3.4, modeled results of $\partial v/\partial z$ and $\partial s/\partial z$ for high $v = 1$ m/s at the Abukuma river mouth are presented in Figure 3.5. We can conclude that for high discharge, both $\partial v/\partial z$ and $\partial s/\partial z$ have peaks at the middle of the water column.

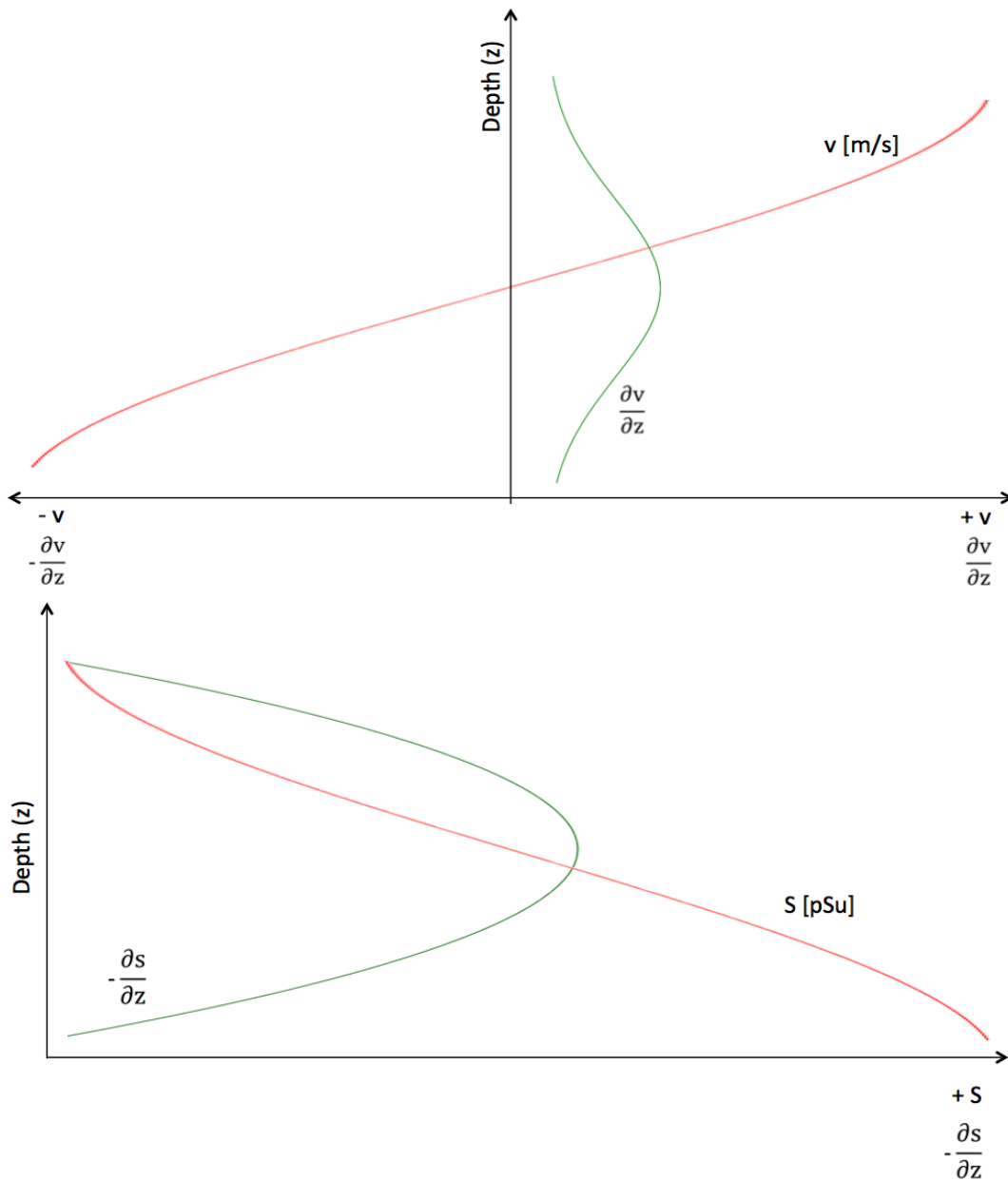


Figure 3.4 Typical profiles over the water column, a)(up) velocity, b)(down) salinity. Profile in red, its derivative in green

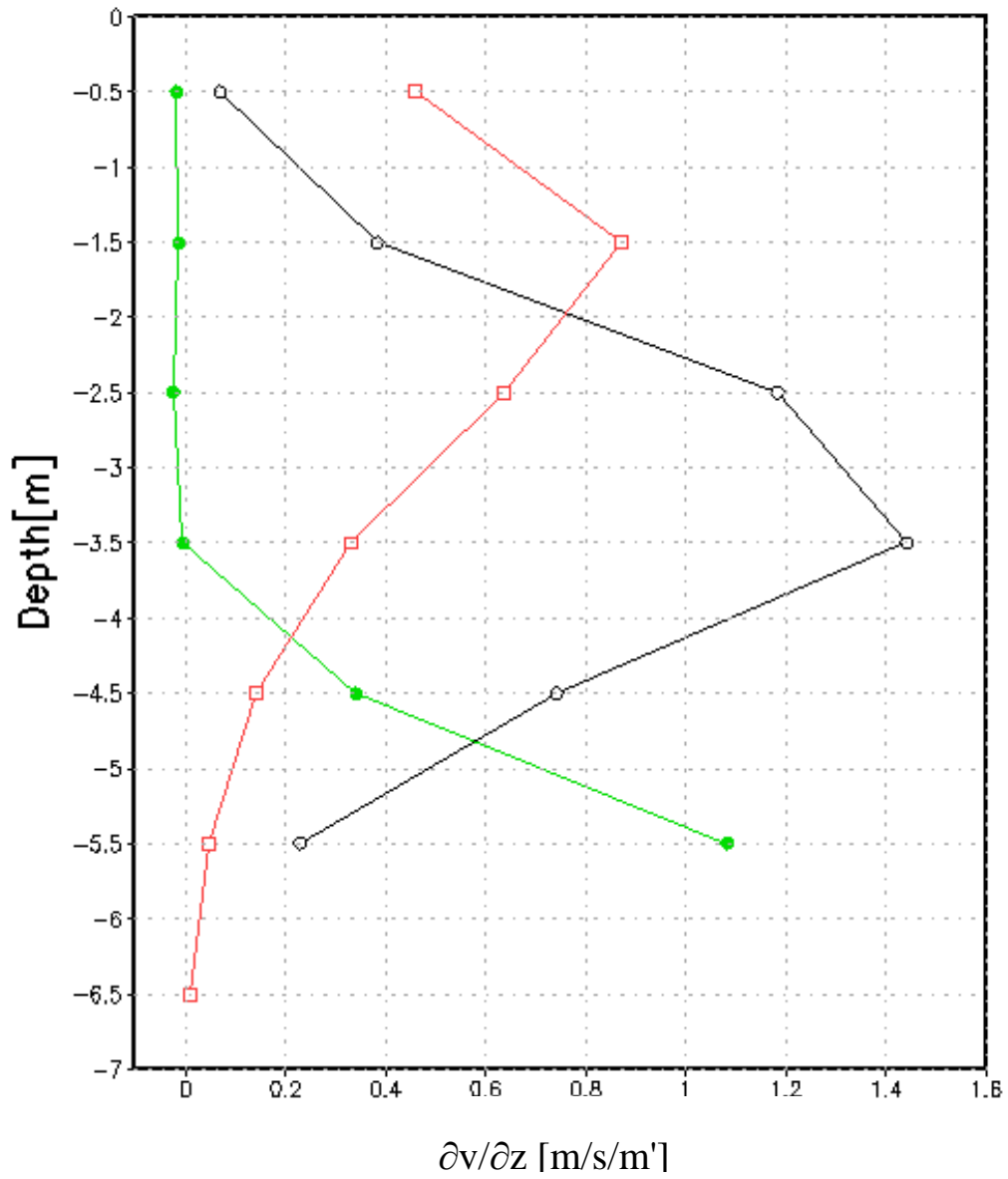


Figure 3.5a Modeled results of $\partial v / \partial z$ for high unidirectional velocity $v = 1$ m/s, on 3 sections close to 140.92E river mouth (140.91E - green, 140.92E - black, 140.94E - red)

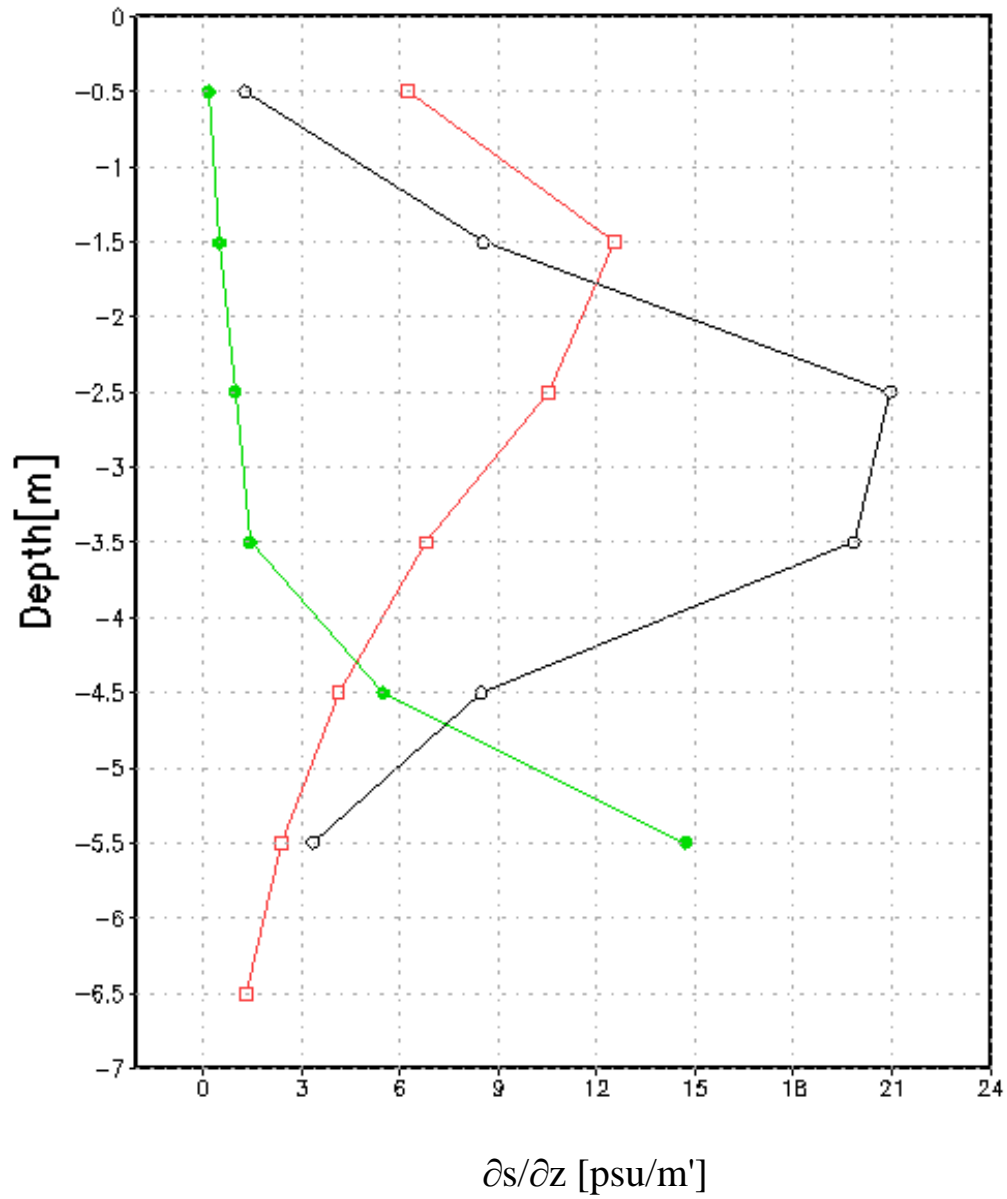


Figure 3.5b Modeled results of $\partial s / \partial z$ for high unidirectional velocity $v = 1$ m/s, on 3 sections close to 140.92E river mouth (140.91E - green, 140.92E - black, 140.94E - red)

3.3.2 Suspended sediment transport phase flow

In order to link conclusions from hydrodynamic phase flow with suspended sediment transport, we used basic theoretical approach to show possibilities of linkage between two phases and applicability of conclusions from hydrodynamic phase flow to formulas of suspended sediment transport phase flow. We compared the hydrodynamic results

with a formula for the terminal settling velocity of a spherical object moving under creeping flow conditions (Lamb, 1994):

$$V_s = \frac{g(\rho_p - \rho_f)d^2}{18\mu} \quad (3.2)$$

where V_s = terminal settling velocity, g = gravitational acceleration, ρ_p = particle density, ρ_f = fluid density, d = particle diameter, and μ = dynamic viscosity. The peak of $\partial s / \partial z$ (Figure 3.4b) in the middle of water column causes both an increase in ρ_f and μ and a decrease in V_s , because there is occurring a sudden boundary between freshwater and saltwater. To quantify our claim from the hypothesis, we will use example where $\rho_p = 2500 \text{ kg/m}^3$, $\rho_{f,\text{fresh}} = 1000 \text{ kg/m}^3$, $\rho_{f,\text{salt}} = 1030 \text{ kg/m}^3$, $\mu_{\text{fresh}} = 0.001002 \text{ Ns/m}^2$ and $\mu_{\text{salt}} = 0.00108$ (for temperature of 20°C). With the above numbers, the quantity $1 - V_{s,\text{salt}}/V_{s,\text{fresh}}$ corresponds to 9.1% anomaly of the settling velocity. If we use another example where $\rho_p = 1500 \text{ kg/m}^3$, the anomaly increases to 12.8%, which are relatively significant anomalies of sediment settling velocities.

Another important fundamental factor which causes a decrease in V_s is the internal shear driven mixing ($\partial v / \partial z$), which is creating a large buoyancy flux Q_b in the middle of the water column (Ralston et al., 2010b)

$$Q_b = g\beta K_H \frac{\partial s}{\partial z} \quad (3.3)$$

where β = coefficient of saline contraction, and K_H = eddy diffusivity. An increase of $\partial v / \partial z$ causes increase of $\partial s / \partial z$ as g , β and K_H are constants. As the $\partial s / \partial z$ is the governing factor of the equation (3), large Q_b causes both an increase in ρ_f and μ , and a decrease in V_s . In order to additionally support our claims, we show and explain meaning of the following quote: "In strongly stratified estuaries and plumes where internal shear mixing was the dominant source of buoyancy flux, the Flux Richardson number $Rf = B/P$ approached maximum efficiency" (Ralston et al., 2010b). Formula for buoyancy flux B is Q_b from equation (3), and P is the shear production

$$P = -\overline{u'w'} \frac{\partial u}{\partial z} - \overline{v'w'} \frac{\partial v}{\partial z} \quad (3.4)$$

When internal shear mixing is the dominant source of buoyancy flux then Rf approaches maximum efficiency means that when P is big then B is even bigger because within equation for P is internal shear mixing and Rf approaches its maximum. Therefore, increasing of $\partial v / \partial z$ in strongly stratified estuaries causes even bigger increase of $\partial s / \partial z$.

Therefore, peaks of both $\partial v / \partial z$ and $\partial s / \partial z$ in the middle of water column highly

contribute to a V_s reduction in that place. However, for low discharge periods when a salt wedge is not occurring, characteristic profiles of $\partial v / \partial z$ and $\partial s / \partial z$ look different showing no significant peaks in the middle of the water column. Hence, the dQ mechanism can only be applied for high discharge periods. V_s reduction in the middle of water column should contribute to accumulation of slower sediment particles around that zone, consequently causing bigger turbidity there.

Basic correlations among dQ and V_s were theoretically and qualitatively discussed by using Equations (3.2) to (3.4) and quantitatively evaluated with a simple example by using the most common values for all parameters. We analyzed behavior of basic terms of Equation (3.1), $\partial v / \partial z$ and $\partial s / \partial z$, for high discharge conditions and their influence to V_s in order to show how an increase of dQ causes a decrease of V_s . Therefore, for high discharge conditions peak of turbidity should occur on depths where are found maximum values of dQ because when dQ is on its maximum on the interface layer between freshwater and saltwater then V_s is maximally reduced around that zone so sediment particles are settling slower at the interface than below the interface so it contributes to accumulation of slower sediment particles at the interface layer and therefore peak of turbidity is occurring around the interface layer.

3.4 Results and discussions

Figure 3.6a shows Q_{fw} 8 h after starting the simulation for high $v = 1$ m/s. Similarly, Figure 3.6b shows Q_{fw} 80 h after starting the simulation for low $v = 0.1$ m/s. We used 10 times longer output simulation time because v is 10 times lower in the second run. Figures 3.7a and 3.7b similarly show the results for dQ for the same high and low velocity simulations, respectively. As dQ is plotted 0.5 meters above the interface of two vertically neighboring grids, total number of depths in Figures 3.7a and 3.7b is lower by 1 m than in Figures 3.6a and 3.6b.

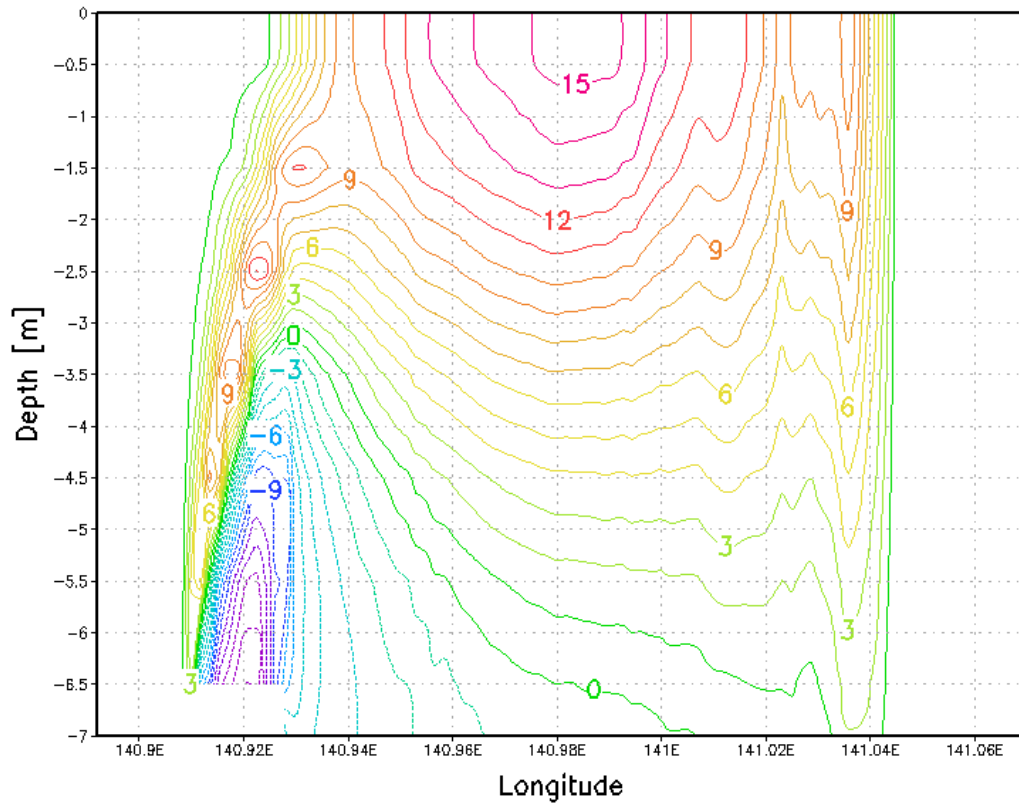


Figure 3.6a Unidirectional salt flux $Q_{fw} = v \cdot s$ [$\text{m}/(\text{s} \cdot \text{psu})$], on river mouth longitudinal section 38.045N for $t = 8$ h; $v = 1$ m/s

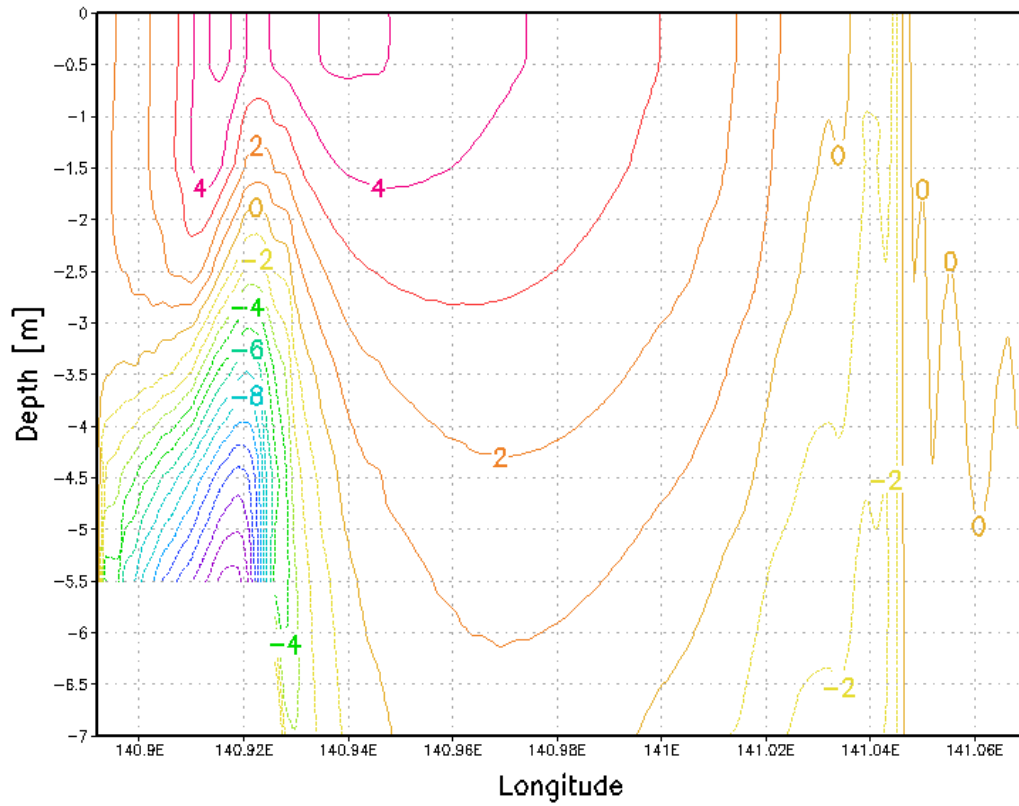


Figure 3.6b Unidirectional salt flux $Q_{fw} = v \cdot s$ [m/(s*psu)], on river mouth longitudinal section 38.045N for $t = 80$ h; $v = 0.1$ m/s

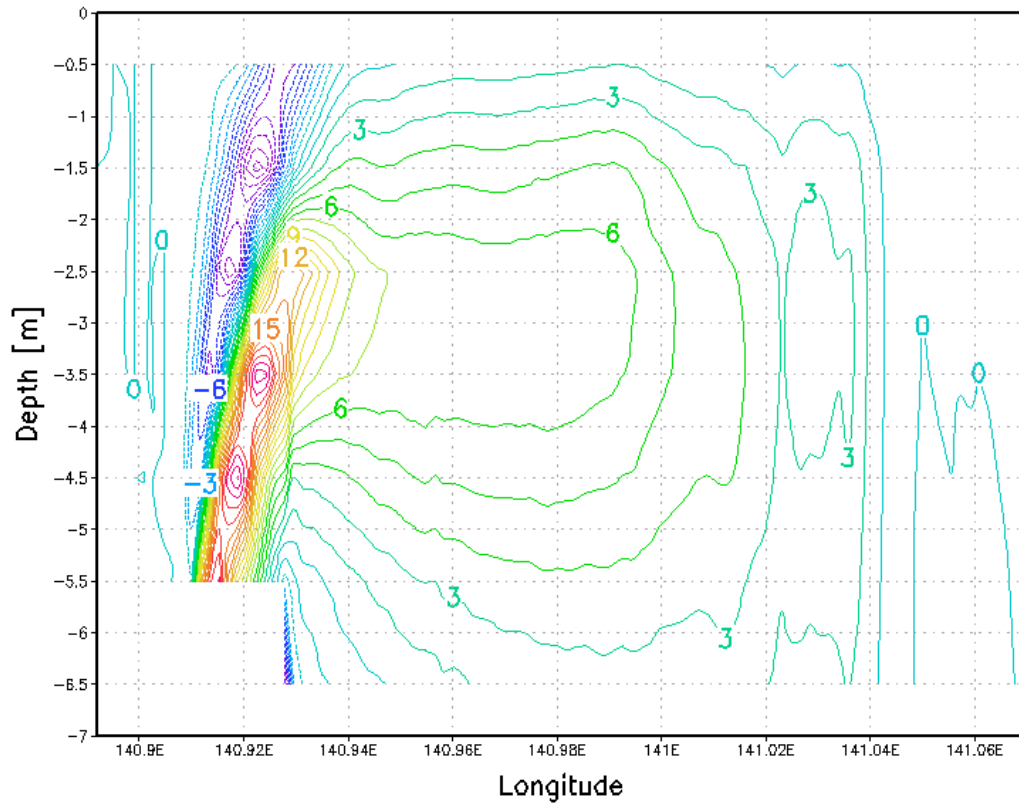


Figure 3.7a Vertically differentiated unidirectional salt flux $dQ = \partial (v*s) / \partial z$ [m/(s*psu)/m'] on river mouth longitudinal section 38.045N for $t = 8$ hours; $v = 1$ m/s

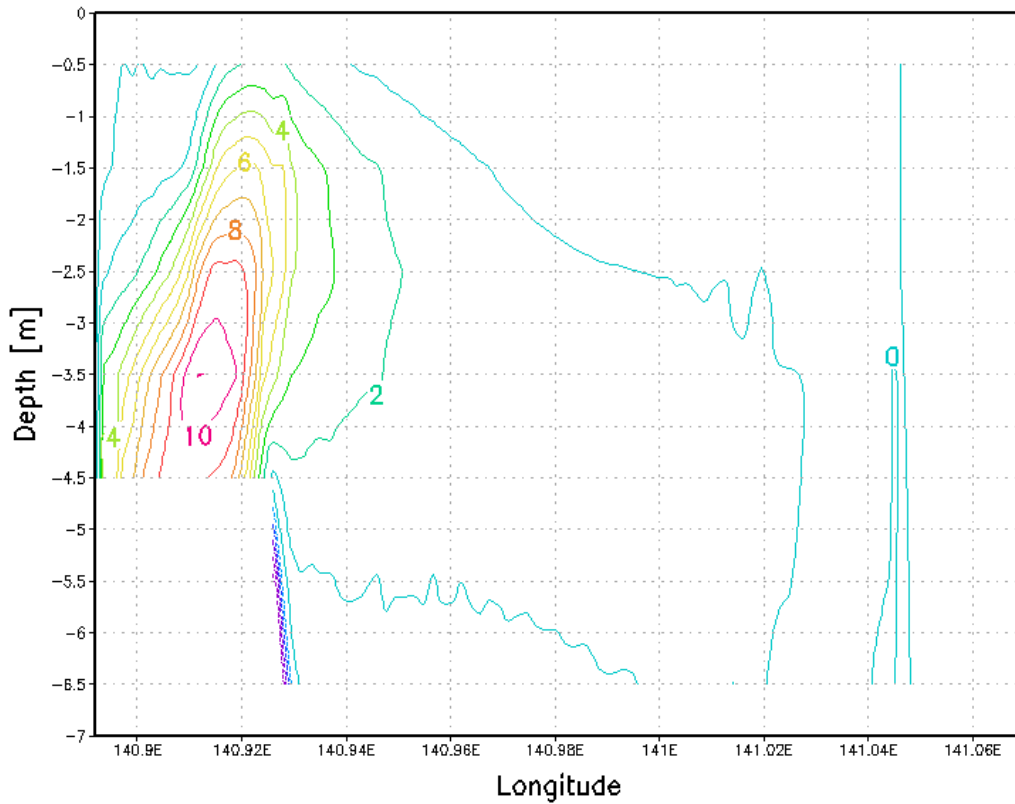


Figure 3.7b Vertically differentiated unidirectional salt flux $dQ = \partial (v*s)/\partial z$

[m/(s*psu)/m] on river mouth longitudinal section 38.045N for $t = 80$ hours; $v = 0.1$ m/s

Figures 3.6a and 3.6b are presented in order to give information about modeled unidirectional salt flux for high and low discharges, respectively in order to give insight into important differences between occurrence of a salt wedge type of estuarine circulation (Figure 3.6a) and a partially mixed estuary (Figure 3.6b). dQ highly depends on Qfw being its derivative over the vertical column, which Figures 3.7a and 3.7b show for high and low discharges, respectively. In Figure 3.6a we can see that results on depth -3 m and 140.92E longitude are the most densely placed relative to each other, which means that dQ has its maximum there, as can be seen in Figure 3.7a. We expect that peak of suspended load transport rate will occur at that place, which is not the case for low Qfw (Figure 3.6b), because a different type of suspended sediment transport is occurring when there is not a salt wedge type of estuarine circulation.

Figure 3.7a shows the most important result of the study. The maximum dQ value is located in the river mouth vicinity in the middle of the water column due to the high

discharge. The positive peak in the middle of the water column in the vicinity of river mouth is an extension of dQ peaks from lower layers of the water column. The internal interface shear layer acts as a boundary where sediment settling velocities decrease and therefore its concentration in upper columns increase. It is similar to place in the middle of the water column where was observed (Yamashiki et al., 2013) an unexpected peak in turbidity data (Figure 3.2). In contrast, Figure 3.7b shows the dQ peak only in the bottom of the water column, where its significance in suspended sediment transport is lower compared to the influence of bottom boundary layer.

Figure 3.7a does not explicitly show linkage of dQ and observed peak turbidity data (Figure 3.2), but their possible relation is theoretically discussed by using V_s as indicator of turbidity peaks. We assumed that, on depths where V_s is lower, there should occur peaks of turbidity and showed that for our considered case it should be in the middle of water column in the vicinity of river mouth on the internal interface shear layer between fluvial and oceanic water, because there dQ have its peak.

3.5 Conclusions

The salt wedge type of estuarine circulation for the given high discharge causes a strong vertical stratification of freshwater and saltwater fluid densities. We neglected the tidal effect in order to isolate the specific mechanism of turbulence suppression by stratification to focus solely on fluvial influence to suspended sediment transport. Modeled results of dQ for high discharge have positive peak in the middle of the water column in vicinity of the river mouth on the internal interface shear layer between fluvial and oceanic water. This corresponds to the same depth where the turbidity peak was found (Yamashiki et al., 2013) by field observations (Figure 3.2).

We have focused just on only one point data because it is the only station point where observed salinity data is decreased in upper water column. On all other station points salinity is constant from top to the bottom so station 1 is exact position where river inflow enters the ocean.

We conclude that dQ can be used to solve the mechanism for occurrence of the middle water column turbidity peaks in a stratified estuary with occurrence of a stable salt wedge. Qualitatively, the suspended load peak should occur around the same place, which is supported by the theoretical fact that both $\partial v / \partial z$ and $\partial s / \partial z$ have its maximum in the middle of the water column for the given high discharge characteristic velocity and salinity profiles (Figure 4).

This is, to our best knowledge, the first chapter discussing the possible linkage between hydrodynamic phase flow and suspended sediment phase flow by using dQ as

the driving linkage mechanism. dQ is shown to be the driving mechanism for suspended sediment transport in the middle of the water column in vicinity of the river mouth, but its application is limited only to high discharge. Although we did not quantitatively solved the linkage between phases but only showed a simple quantitative example, we discussed meanings of dQ results and qualitatively approached theoretical governing mechanisms about how they may influence suspended sediment phase flow.

Solving dQ as a function of relative influence of fluvial and tidal forcing or in different environments would be an interesting follow up of the research, as well as possibly providing quantitative approach towards its linkage with suspended sediment phase flow.

References

- Amante C, Eakins BW. 2009. ETOPO1 1 Arc-Minute Global Relief Model: Procedures, Data Sources and Analysis, NOAA Technical Memorandum NESDIS NGDC-24., *National Geophysical Data Center*, NOAA. Doi:10.7289/V5C8276M.
- Dyer KR. 1973. Estuaries: a physical introduction, *John Wiley & Sons: London*. ISBN 0471-22905-9.
- Geyer WR. 1993. The importance of suppression of turbulence by stratification on the estuarine turbidity maximum, *Estuaries* Vol. 16, No. 1, pp. 113-125.
- Geyer WR, Hill PS, Kineke GC. 2004. The transport, transformation and dispersal of sediment by buoyant coastal flows, *Continental Shelf Research* 24, pp. 927-949. Doi: 10.1016/j.csr.2004.02.006.
- Geyer WR, Scully ME, Ralston DK. 2008. Quantifying vertical mixing in estuaries, *Environmental Fluid Mechanics* 8, pp. 495-509. Doi: 10.1007/s10652-008-9107-2.
- Geyer WR, MacGready P. 2014. The estuarine circulation, *Annual Review of Fluid Mechanics* 46, pp. 175-197. Doi: 10.1146/annurev-fluid-010313-141302.
- Kida S. 2011. The impact of open oceanic processes on the Antarctic bottom water outflows, *Journal of Physical Oceanography* Vol. 41, pp. 1941-1957. Doi: dx.doi.org/10.1175/2011JPO4571.1.
- Kida S, Yamashiki Y. 2015. A layered model approach for simulating high river discharge events from land to the ocean, *Journal of Oceanography* 71, pp. 125-132. Doi: 10.1007/s10872-014-0254-4.
- Lamb H. 1994. Hydrodynamics (6th edition). *Cambridge University Press*, pp. 599, ISBN 978-0-521-45868-9.
- MacDonald DG, Geyer WR. 2004. Turbulent energy production and entrainment at a highly stratified estuarine front, *Journal of Geophysical Research* Vol. 109, C05004. Doi:

10.1029/2003JC002094.

National Oceanographic Data Center (NODC, 2007) World Ocean Atlas 2005. Available online at https://www.nodc.noaa.gov/OC5/WOA05/pr_woa05.html. Last access: December 28, 2015.

Ralston DK, Stacey MT. 2007. Tidal and meteorological forcing of sediment transport in tributary mudflat channels, *Continental Shelf Research* 27(10-11), pp. 1510-1527. Doi: 10.1016/j.csr.2007.01.010.

Ralston DK, Geyer WR, Lerczak JA. 2010a. Structure, Variability, and salt flux in a strongly forced salt wedge estuary, *Journal of Geophysical Research* 115, C06005. Doi: 10.1029/2009JC005806.

Ralston DK, Geyer WR, Lerczak JA, Scully M. 2010b. Turbulent mixing in a strongly forced salt wedge estuary, *Journal of Geophysical Research* 115, C12024. Doi: 10.1029/2009JC006061.

Warner JC, Geyer WR, Lerczak JA. 2005. Numerical modeling of an estuary: A comprehensive skill assessment, *Journal of Geophysical Research* Vol. 110, C05001. Doi: 1029/2004JC002691.

Wright LD, Nittrouer CA. 1995. Dispersal of river sediments in coastal seas: six contrasting cases, *Estuaries* Vol. 18, No. 3, pp. 494-508.

Yamashiki Y, Pratama A, Varlamov S, Miyazawa Y, Yamazaki H, Ishida M, Niwa Y. 2013. Field observation on physical characteristic of Abukuma river estuary in Sendai Bay, *Proceedings of GCOE-ARS Final symposium* 64-65.

Yamashiki Y, Onda Y, Smith HG, Blake WH, Wakahara T, Igarashi Y, Matsuura Y, Yoshimura K. 2014. Initial flux of sediment-associated radiocesium to the ocean from the largest river impacted by Fukushima Daiichi Nuclear Power Plant, *Scientific Reports* 4:3714. Doi: 10.1038/srep03714.

Chapter 4 - Total freshwater outflow from Japanese basins to western Pacific ocean

4.1 Significance of total freshwater outflow calculation in coastal and climatological modeling

Coastal and climatological models do not usually use freshwater outflow data from river's estuaries because they either neglect the data as insignificant or have difficulties to implement these data into their models. River inflow to oceans is the most important component of global hydrologic cycle, as it connects the oceanic and continental water (Shiklomanov, 2009). We need to estimate freshwater discharge in order to properly study about global water cycle (Dai and Trenberth, 2003). In addition, appropriate simulations of freshwater inflow to oceans are becoming very important in global climate models (Miller et al. 1994). It is important to include river flow in climate models because it supplies oceans with freshwater and affects ocean convection and circulation (Miller et al., 1994). Figure 4.1 shows annual discharge from each coastal box for the World ocean (Dai and Trenberth, 2003).

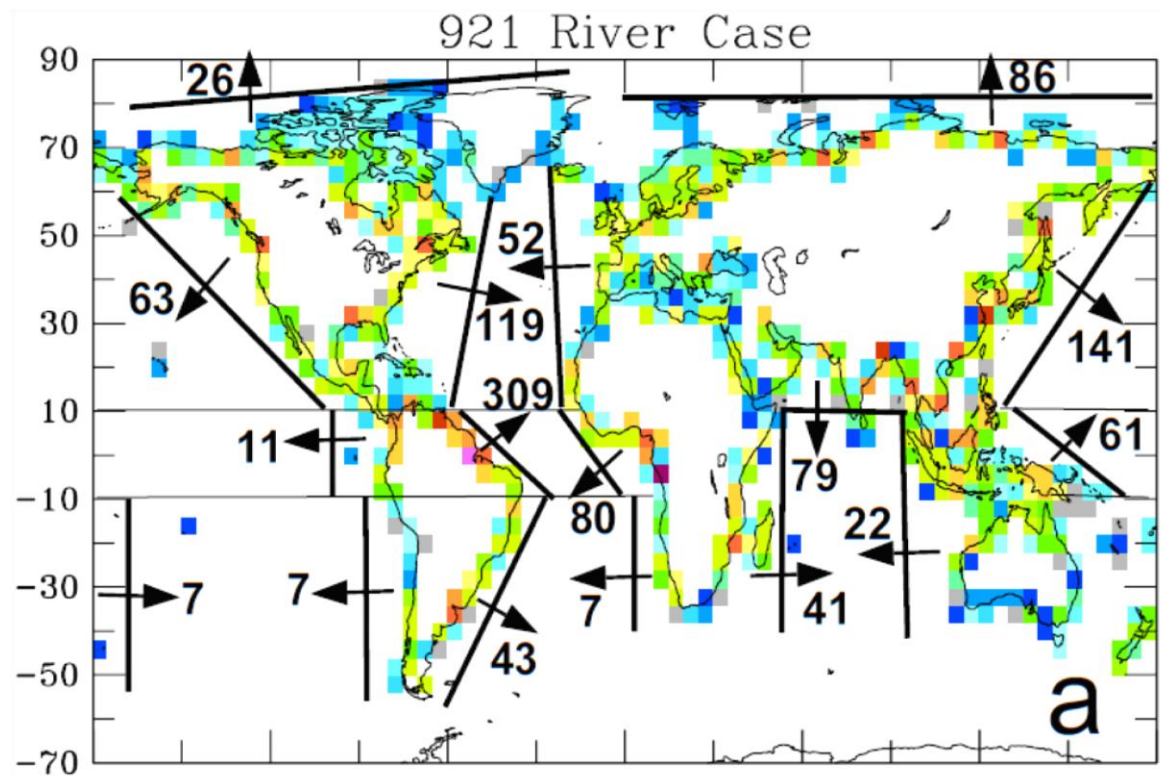


Figure 4.1 Annual discharge from each coastal box [$1000 \text{ m}^3/\text{s}$] (Dai and Trenberth, 2003)

River runoff to oceans have been estimated since 1880s with different accuracy levels (Shiklomanov, 2009). More recently, studies about hydrodynamic, biological and chemical processes have served for huge improvement in understanding of the estuarine processes at seasonal and smaller scales (Knowles, 2002). Milliman et al., (2008) found that "during the last half of the 20th century, cumulative annual discharge from 137 representative rivers to the global ocean remained constant, although annual discharge from about one-third of these rivers changed by more than 30%". River flow is

useful indicator of freshwater resources and availability which makes it useful for indication of climate changes and increasing flooding events. (Falloon and Betts, 2006). Freshwater inflow to oceans is mostly concentrated at the mouth of rivers, which provides local freshwater inflow forcing oceans regionally by changes in density. (Dai and Trenberth, 2002). Freshwater flux into the ocean surface changes the stratification of near-surface layer and temperature of the mixed layer (Carton, 1991). One of the most important effect of freshwater inflow in estuarine and coastal zone is that surface salinity distribution gets lowered near the mouth of major rivers (Talley, 2002). Large rivers do not only influence salinity distribution in coastal zone but it can influence the distribution far away from its mouth (Urakawa et al., 2015). Freshwater flux anomalies on ocean surface have impact on the stratification of the tropical mixed layer. (Carton, 1991). Global climate models do not have closed hydrologic cycle, because they often neglect freshwater inflow to the oceans. Their scales are much larger than the catchment basin scales which are often used in hydrologic models (Miller et al., 1994). Thus, in order to have enclosed hydrologic cycle in global climate models, the total river outflow data towards the ocean is needed. Figure 4.2 shows 1951 - 2000 discharge trends for 137 global rivers (Milliman et al., 2008).

Dai et al. (2008) stated that the discharge from rivers plays a key role in the global biogeochemical cycles. Extreme freshwater inflow can induce significant buoyancy and salinity anomalies in the ocean (Kida and Yamashiki, 2015). Coastal waters of Japan have extremely low salinities due to freshwater fluxes. (Urakawa et al., 2015). We need to have a precise dataset of freshwater fluxes for realistic coastal ocean modeling. (Urakawa et al., 2015). Urakawa et al. (2015) investigated the effect of river runoff on salinity along the coasts of Japan however they focused on normal average discharge while our study simulated peak discharge and also we used SCE-UA optimization method as advancement of our study. Freshwater inflow in ocean is relatively small compared to total ocean volume, but it is very important for water balance and for physical processes occurring in oceans (Shiklomanov, 2009). River discharge data can provide the most accurate quantitative information about global water cycle, but it is not yet properly adopted in global atmospheric and ocean models (Fekete et al., 2002). A river transport model that connects the global circulation with river mouths is needed (Dai and Trenberth, 2002). Freshwater discharge occurs locally at the mouths of rivers and forces ocean circulations regionally through changes in density (Dai et al., 2008). Dai and Trenberth (2003) estimated the river mouth outflow from the world's large rivers by adjusting the streamflow rate at the farthest downstream station using the ratio of simulated flow rates at the river mouth and the

station. Fekete et al. (2012) demonstrated the potential of combining observed river discharge information with climate-driven water balance model outputs to develop composite runoff fields. Salinity changes due to freshwater inflow have many important effects on the dynamics of mixed layer, especially where the discharge is big. (Carton, 1991). Figure 4.3 shows global mean annual combined runoff field (Fekete et al., 2002).

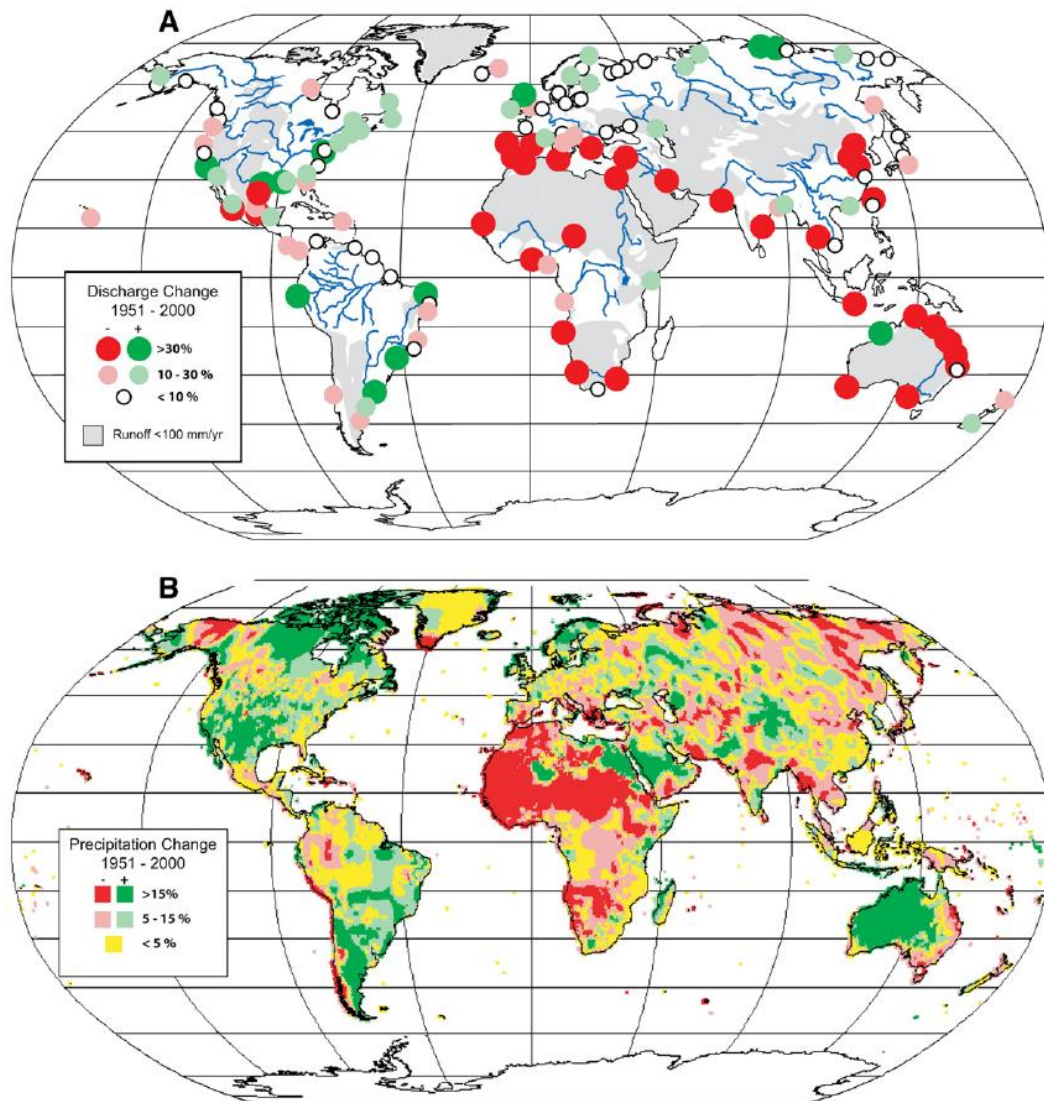


Figure 4.2 Discharge trends 1951 - 2000 for 137 global rivers (Milliman et al., 2008)

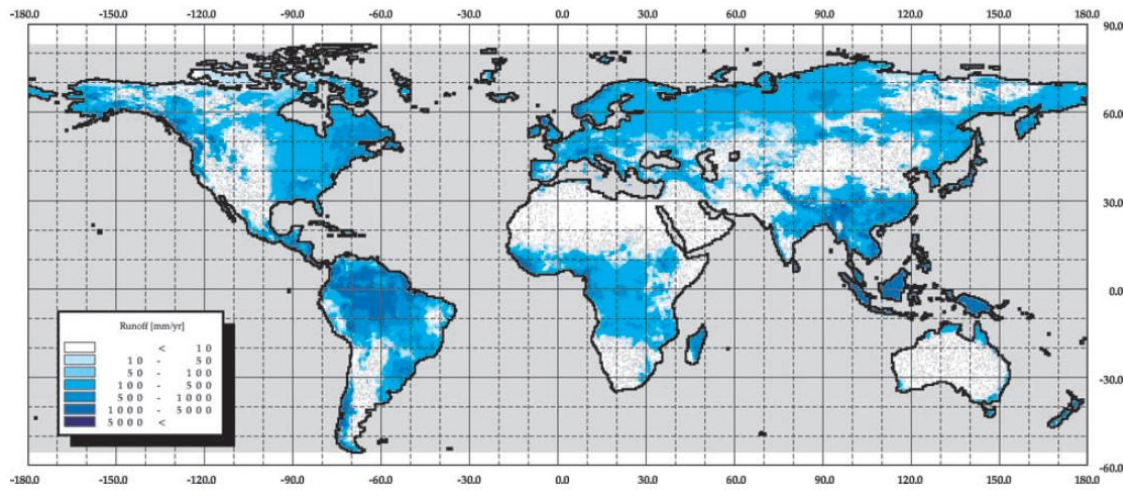


Figure 4.3 Mean annual combined runoff field (Fekete et al., 2002)

The objective of the chapter is to create complete set of simulated river outflow data from 9 first class Japanese river basins to western Pacific ocean, in order that the data can be used by researchers dealing with Land-Ocean interaction who are developing joint hydrological-oceanographic models for modeling of estuarine and coastal processes, or for developing more accurate climatological models where fluvial influence on the river mouth is needed to join the oceanographic, meteorology and hydrology cycle into bigger comprehensive closed cycle, or for developing accurate nowcasting models for real time prediction of extreme flood events for flood defense disaster prevention management.

4.2 Overview of Japanese basins on western Pacific ocean coast

In this study our focus is on first class rivers flowing from eastern Japanese coast basins into western Pacific ocean. Japanese river systems are characterized by relatively short reaches, steep elevation, and higher rainfall intensity than in many other countries (Luo et al., 2011). There are 9 first class rivers flowing from eastern Japanese coast basins into western Pacific ocean, from north to south Takase, Mabechi, Kitakami, Naruse, Natori and Abukuma under the control of Tohoku Regional Bureau, and Kuji, Naka and Tone under the control of Kanto Regional Bureau. Figure 4.4 shows ArcGIS flow accumulation map of 9 targeted basins. Figures 4.5, 4.6, 4.7 (<http://www1.river.go.jp/>) show the map of 9 rivers, Figure 4.5 shows Takase and Mabechi, Figure 4.6 shows Sendai bay with Kitakami, Naruse, Natori and Abukuma and Figure 4.7 shows Kuji, Naka and Tone rivers.

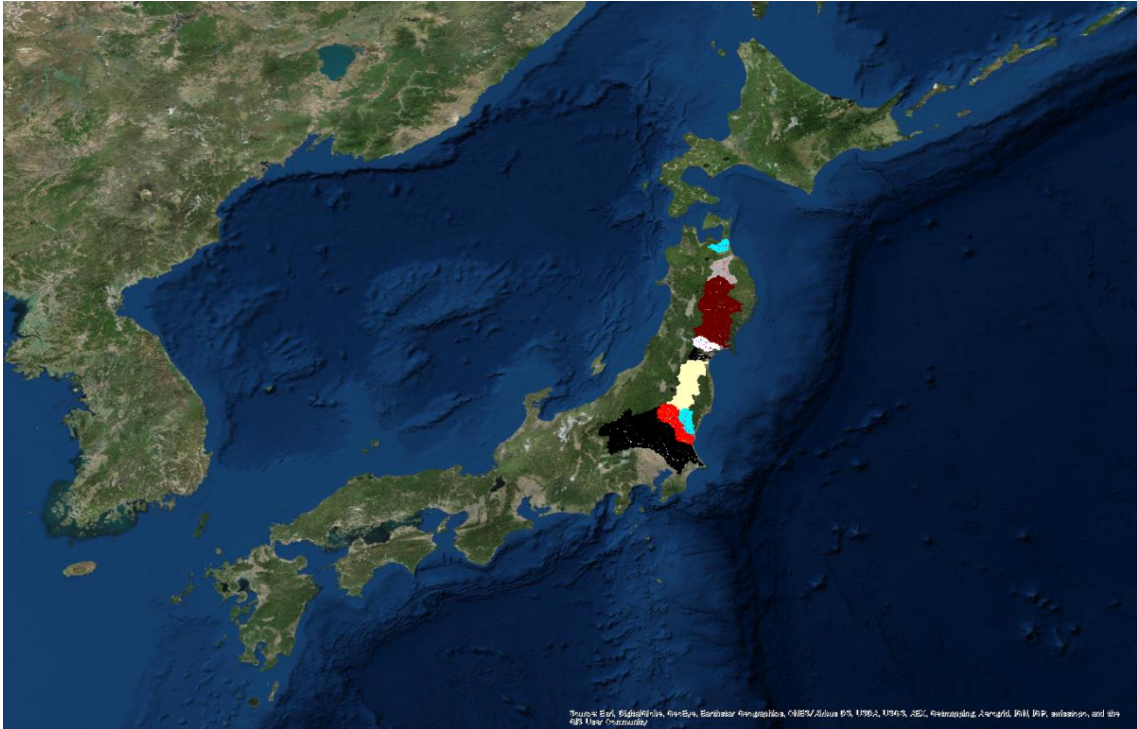


Figure 4.4 Map of targeted 9 first class Japanese river basins flowing to western Pacific ocean (ESRI, World Imagery, 2016)

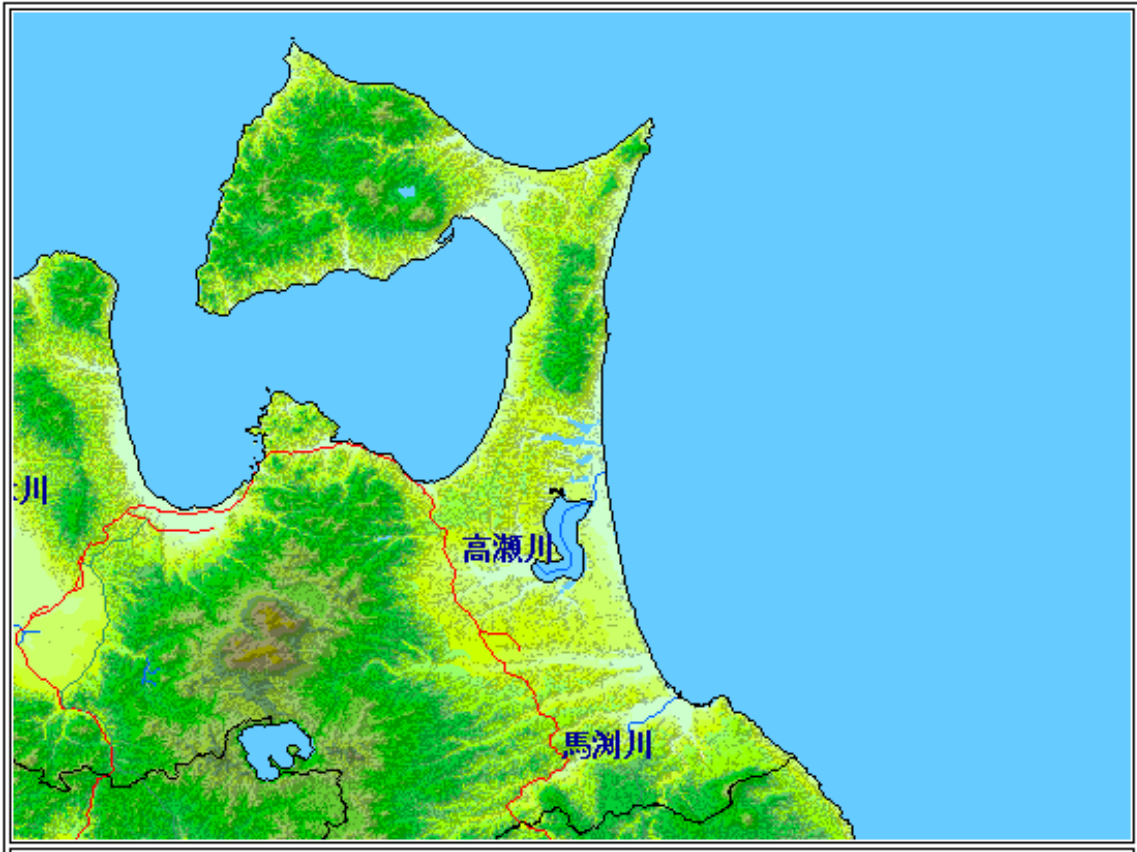


Figure 4.5 Northeastern Japanese Pacific coast with Takase and Mabechi rivers
(<http://www1.river.go.jp/>)

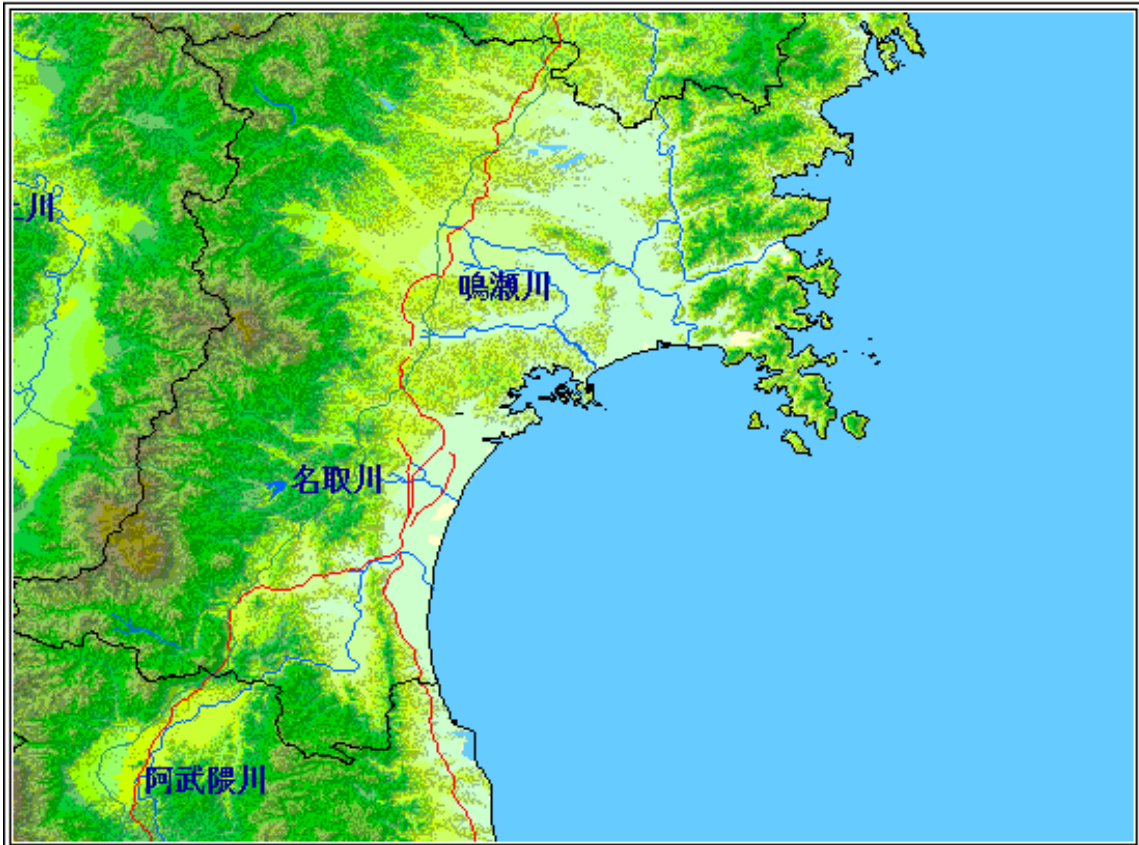


Figure 4.6 Sendai bay with Kitakami, Naruse, Natori and Abukuma rivers
(<http://www1.river.go.jp/>)

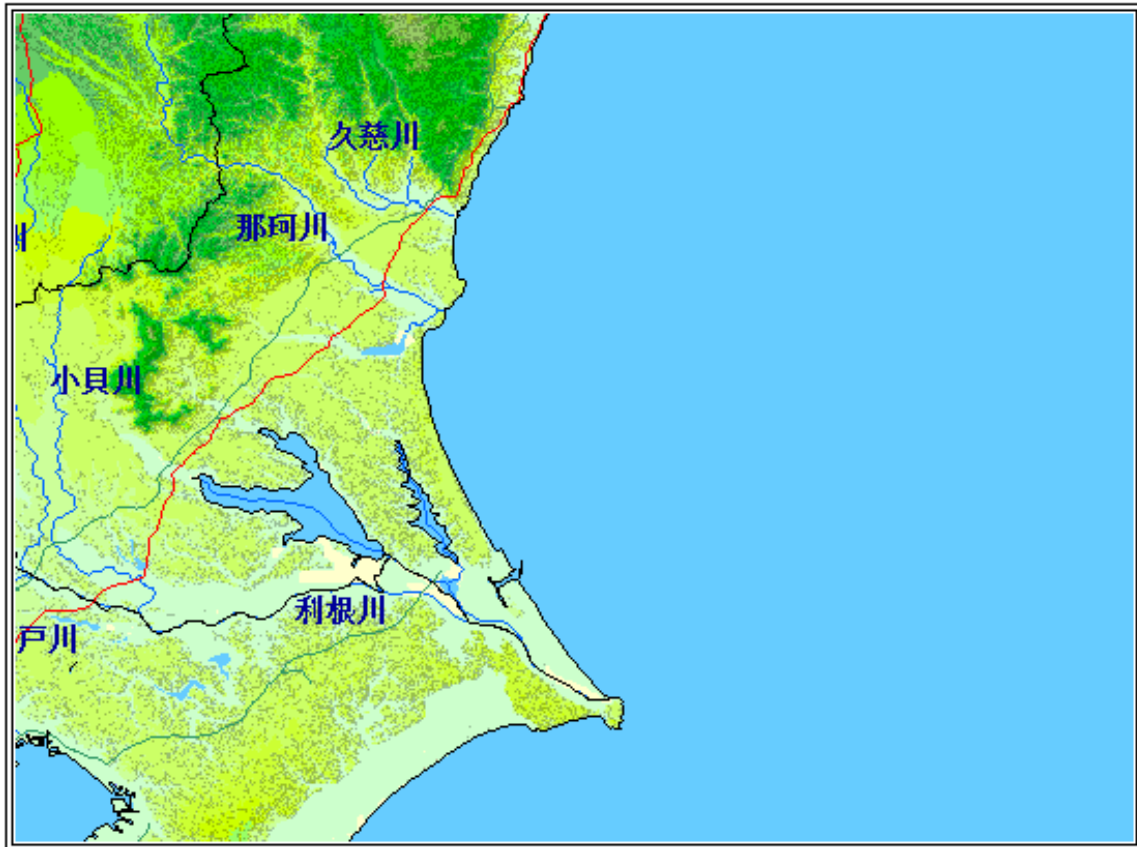


Figure 4.7 Southeastern Japanese Pacific coast with Kuji, Naka and Tone rivers
 (<http://www1.river.go.jp/>)

Based by catchment area, rivers are classified as follows:

Tone (12.458 km²), Kitakami (7.869 km²), Abukuma (5.625 km²), Naka (2.552 km²), Mabechi (2.024 km²), Kuji (1.442 km²), Naruse (1.158 km²), Takase (867 km²), Natori (776 km²).

4.3 Overview of cell distributed runoff model

In the cell distributed runoff model version 3.1.1. (www.flood.dpri.kyoto-u.ac.jp/previous_page/product/cellModel/cellModel.html; Sasaki, 2014; Luo et al., 2014; Sayama and McDonell, 2009; Tachikawa et al., 2004; Nishiumi, 1998, Kojima et al., 1998), multiplied by a mesh (net) in the basin, we track the rain that falls on every single square section (rectangular cell) of the net into the steepest gradient direction. Each cell is forest, farmland, urban area, and represent a unit area, including rivers, rain water flows down in each cell, and is considered to flow out into

the cell directly below it. (Figure 4.8) has specific way of thinking, as follows.

- DEM surrounding $dm \times dm$ of elevation values (grid intersection), that is considered a DEM of the combined square of area one partial basin to the resolution (cell), the entire basin square of partial basin (cell) gathered a large number.
- We determined the steepest gradient direction of the surrounding eight directions of DEM of elevation values and drew a waterfall diagram in that direction. If there is more than one the steepest gradient direction, it draws a drainage line average elevation value of grid intersection in the surrounding eight directions above area to the lowest direction.
- In each cell, we input a uniform effective rainfall in the cell, and the upstream end inflow by summing the flow from the upstream side cells, and it calculates the flow amount by the Kinematic Wave method. Basic equations of (surface flow only) slope flow of a single element is represented by the following equation.

$$\begin{cases} \frac{\partial h}{\partial t} + \frac{\partial q}{\partial x} = r_e \\ q = f(h) = \frac{\sqrt{S}}{N} h^m \end{cases} \quad (4.1.)$$

In each individual cell, q : unit width flow rate, h : water depth, r_e : effective rainfall, S : slope gradient, N : the equivalent roughness, m : the slope constant ($=3/5$). Slope S is obtained from the DEM, the equivalent roughness N is generally a value or observations used in the Kinematic Wave method where it is treated as a model parameter by setting the upper limit.

- If you think about the surface layer of high permeability on the slope, the matrix section is dominated by unsaturated underground flow in the surface layer, and is divided into a large void portion where gravitational water dominates, and with further integration with the ground surface flow analysis it is possible to schematically model the soil layer (Figure 4.9). The soil layer thickness is a D , which considers a value representing the maximum water content of the matrix portion in depth d_m , the maximum depth which may be present in the surface soil, including gravitational water and d_a , the following flow rates and flow volume relationship which can be assumed (Tachikawa et al., 2004):

$$q = \begin{cases} v_m d_m \left(\frac{h}{d_m} \right)^\beta, & 0 \leq h \leq d_m \\ v_m d_m + v_a (h - d_m), & 0 \leq h \leq d_a \\ v_m + v_a (h - d_m) + \frac{\sqrt{i}}{n} (h - d_a)^m, & d_a < h \end{cases} \quad (4.2.)$$

The relationship between q and h is represented by the formula shown in Figure 4.10. This makes it possible to make the propagation speed, and becomes possible to track the rainwater in combination with the continuous basic equations.

- Cell distributed model performs the flow calculation using a Kinematic Wave method as the flow of river for cell representing a river. In other words, the entire basin is made from the cell that represents the cell and the river that represents the slope.

We mentioned an overview of the cell distributed runoff model and more. The model parameters are roughness coefficient N , layer corresponding to the total gap thickness d_a , the layers of matrix section thickness d_m , saturated hydraulic conductivity k_a of the large gap, the ratio of saturated hydraulic conductivity and the matrix portion of the large gap β and so on.

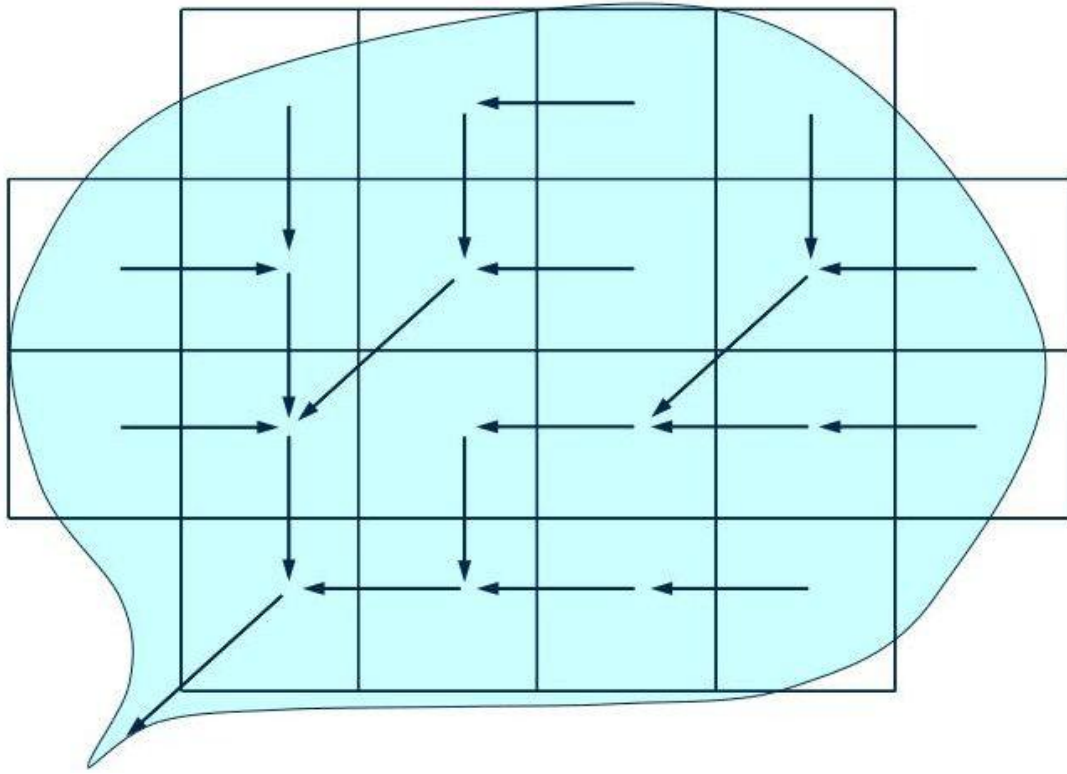


Figure 4.8 Conceptual diagram of the cell distributed runoff model (Kojima et al., 1998)

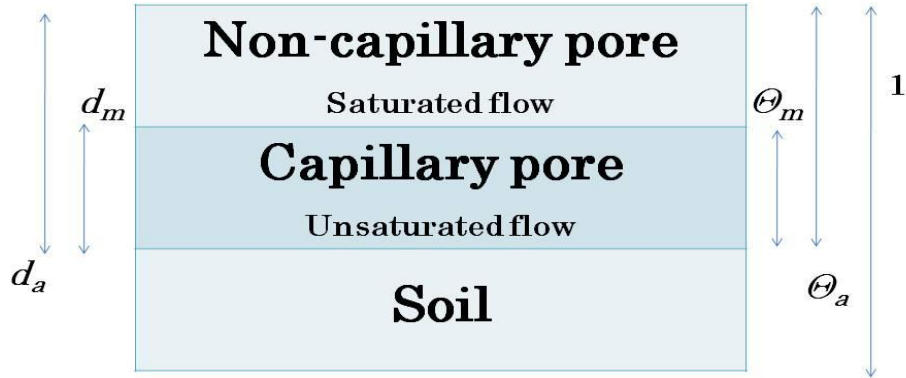


Figure 4.9 Structure of the assumed soil layer (Tachikawa et al., 2004)

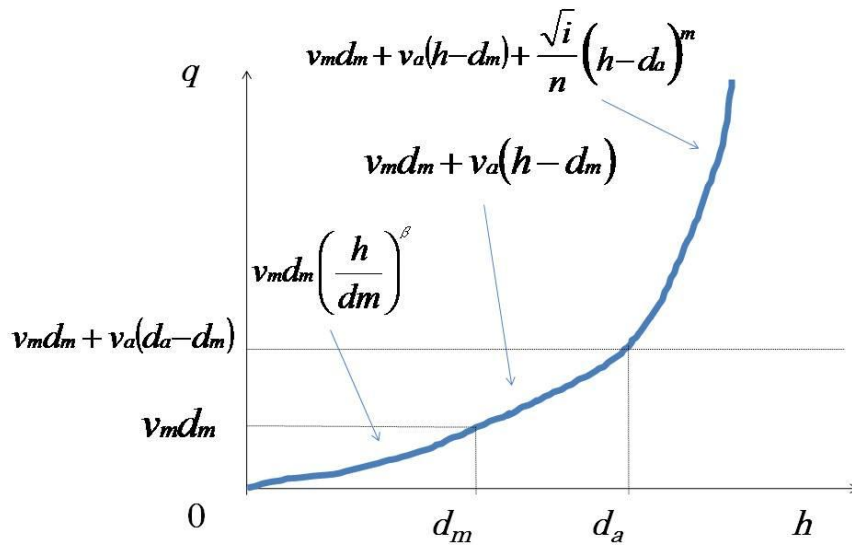


Figure 4.10 Function form of the flow stream product relationship (Tachikawa et al., 2004)

4.4 Overview of SCE-UA optimum value search method

In the present study, Nash-Sutcliffe coefficient NS (Nash and Sutcliffe, 1970) was used as accuracy evaluation index of outflow calculation. NS is the accuracy evaluation index widely used particularly in Europe and the United States. NS represents the high adaptability of the calculated values and even more the observed value closer to 1, as long as reproducibility of the calculation is $NS \geq 0,7$ for different basins and rainfall events, it is highly compatible.

NS at the time of parameter identification of calculation flow rate is given in the following manner.

$$NS = 1 - \frac{\sum_{i=1}^N (Q_o(i) - Q(i))^2}{\sum_{i=1}^N (Q_o(i) - \overline{Q_o})^2} \quad (4.3)$$

Where N : the number of time steps, $Q_o(i)$: observation flow rate, of the time i , $Q(i)$: calculated flow rate in time i , $\overline{Q_o}$: is the average value of the observed flow rate.

Developed by Hydrological Department of University of Arizona (Gupta et al., 1992, Gupta et al., 1993), SCE-UA method (Sasaki, 2014; Harada et al., 2006; Gupta et al., 1994) is similar to the genetic algorithm, a kind of global optimum search method that combines the concept of a set mixing. Rather than representing each individual genotype as genetic algorithms, if the parameters to be searched are n , it is regarded as the point on the n -dimensional space with respective individual of the respective parameters as axes. This n caused the initial point group on dimensional space, are arranged in the objective function value order, such as Nash-Sutcliffe coefficient. Then all the point cloud is divided into groups, and the evolution of the population so as to improve the objective function in accordance with CCE (Competitive Complex Evolution) algorithm, and performs the convergence judgment. Mirror image step, which will be described later in CCE algorithm performs operation of contraction step and mutation step, to evolve the population. A point closer to the less optimal value of the error by CCE algorithm has lesser evolution number. Large point errors conversely have a high probability of performing such steps, to approach the optimal solution that will evolve. By repeating such operations, it is required to perform solution or the optimal solution for a given problem.

4.4.1 Calculation method

In describing the calculation method assuming n number of model parameters we want to optimize, parameters set the objective function indicates a minimum value and

the optimal solution of the model. The model step of SCE-UA method is shown in Figure 4.11 After we described overall algorithm Calculation SCE-UA method, the following describes how to calculate the CCE algorithm as a submodel, and a simple example will be specifically described.

Step 1. Number of population p , The number m in each population $p \geq 1, m \geq n+1$ is selected so as to meet criteria.

Step 2. For such as the existence range of the optimal solution of the search space of interest, in the normal case there is no prior knowledge, search space $\Omega \subset R_n$

Extracts randomly s ($s = pm$) number of points from $x_i, i = 1, 2, \dots, s-1, s$ and calculates the objective function value f_i at x_i . Objective function value s number of points is the minimum point as first place, and arranged from smaller ones in order.

Step 3. Divide these points to p number of population $A_k, k = 1, \dots, p$. Population A_k is intended to include the m points $x_{k+p(j-1)}, j = 1, \dots, m$.

Step 4. Evolve by CCE algorithm which will be described later for each population.

Step 5. By mixing the points to be included in all populations objective function value s number of points is the minimum point at first place to the convergence determination side by side from the smaller ones. Until satisfied convergence criterion is terminated, otherwise it goes back to step 3.

In the step 4., we described the method of calculating CCE in the algorithm. CCE algorithm evolves each population, ie population $A_k, k = 1, \dots, p$ where it is a sub-model to reduce (improve) the objective function value of m points that are included in the population. The model step of CCE algorithm is shown in Figure 4.12.

CCE 1. To show evolving for the number q , we selected α, β number of iterations, where is $2 \leq q \leq m, \alpha \geq 1, \beta \geq 1$.

CCE 2. The selection probability is given by the following trapezoidal distribution for each assigned ρ_i point contained in the A_k .

$$\rho_i = \frac{2(m+1-j)}{m(m+1)}, \quad j=1, \dots, m \quad (4.4)$$

CCE 3. From A_k according to the selection probability that is defined earlier the different q number of points are randomly selected to determine the respective objective function values. It should be noted, these points and the objective function value should be stored as an array. A point that is included in this array as a parent generates a descendant in accordance with the following procedure.

- a. from the selected point q , I find the center of gravity G of all the points except the U point the biggest objective function value of $(q-1)$.
- b. determine the point of symmetry R of the point U on the center of gravity G by the following equation (mirror image step).

$$R = 2G - U \quad (4.5.)$$

Here, if the point R is included in the search space, the procedure calculates the function values $f(R)$ of the point R and proceeds to the calculated step c. Otherwise, it calculates the smallest polyhedron with all points A_k and selects one random point, to the point R and so on (mutation steps).

- c. If $f_R < f_U$, it replaces the point U at the point R and proceeds to step e. Otherwise, it obtains a middle point C of the point U and the center of gravity G , to calculate the function value $f(C)$ of the middle point C (shrinking step).
- d. If $f_C < f_U$, it replaces the point U to point C , and proceeds to step e. Otherwise, it calculates the smallest polyhedron with all points A_k to select one point at random, to the point R and so on (mutation steps).
- e. Point a. From the point e. Repeat α times.

CCE 4. Replace a point after the evolving point as a parent who elected from A_k (descendants), aligning the m points in the A_k in the objective function value order.

CCE 5. Repeat CCE 2 to CCE 4 up to β times.

Here, the number of parameters is X , for there is the second objective function of Y (objective function) where the number of population is 2, we will give as an example a case in which the set to a population is the number 5. Figure 4.13 and Figure 4.14, respectively, show the objective function value transition diagram according to SCE-UA algorithm and the objective function value transition diagram according to CCE

algorithm.

Curves in each figure represent the objective function value by parameters X and Y , when $X = 4, Y = 2$, the minimum value is the optimal solution of the objective function. $X = 1, Y = 3$ Objective function value is minimum value, the higher the possibility of ending the search at this point is a local optimum value search method. The same black dot indicates that a point represented by an asterisk is the same group.

Figure 4.13a is obtained and distributed according to the number of groups in accordance with an objective function value order where all 10 points were randomly generated. Figure 4.13b is the distribution of the objective function value of 10 points after each population has evolved through the steps of the predetermined number of times by CCE algorithm. Population of black spots close to the global optimum, the population of the asterisk is seen with the approach to locally optimal solution. Here is again arranged in the objective function value order as 10 points did not meet the convergence condition, and the distribution in accordance with the number of population.

Figure 4.13c represents the 10 points after the second group classification, obtains 10 points as in Figure 4.13d through the evolution of CCE algorithm. All 10 points while reducing the efficient search space share the whole information by the population distributed over again. After Figure 4.13d, in order to meet the calculated conditions, converged conditions are again arranged in the objective function value order to form a new evolving population.

Meanwhile, Figure 4.14 is point that is distributed to the population to find how to evolve the CCE algorithm, the objective function value indicates whether it is going to change. Here it was 3 evolution points group and q. 3 point that form a triangle in the figure evolved for point cloud. It is chosen randomly according to the selection probability as described above. That reduces the chance that the objective function value is involved in the global optimum value to about fewer selection probability evolution, the greater the higher the selection probability objective function value away from the global optimum value increases, it is treated as the worst point possibility to increase. Also we have set the number of iterations and α was set to 5. From Figure 4.14a to Figure 4.14e it shows the population that have evolved by the mirror image step, shrinkage step or mutation step, and Figure 4.14f shows the population after five times iterations.

Figure 4.14a shows the evolution by mirror image step in Figure 4.14b and also in Figure 4.14d. Select the worst point of the three point forming a triangle, was replaced with the worst point since the improved objective function value is considered

contrasting point to the center of gravity of the remaining two point which is not a worst point (consequently center), and it is obtained by evolution.

Figure 4.14c shows the evolution due to shrinkage step. Considering the midpoint between the center of gravity of the remaining two points which are not at the worst point and the worst point, it calculates the objective function value at that point, if the result from the objective function value at the worst point is good, and replaces the worst point group and a step of evolution.

Figure 4.14e represents the evolution by mutation steps of those evolved to substituted force.

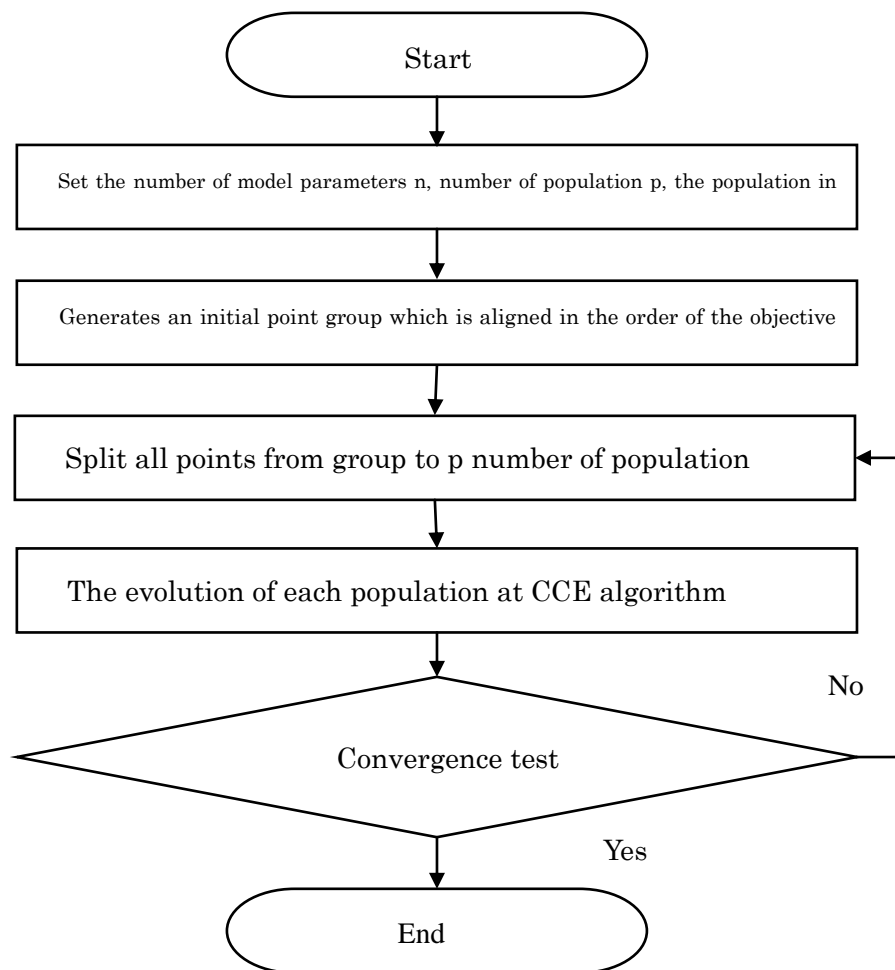


Figure 4.11 Model system of SCE-UA algorithm

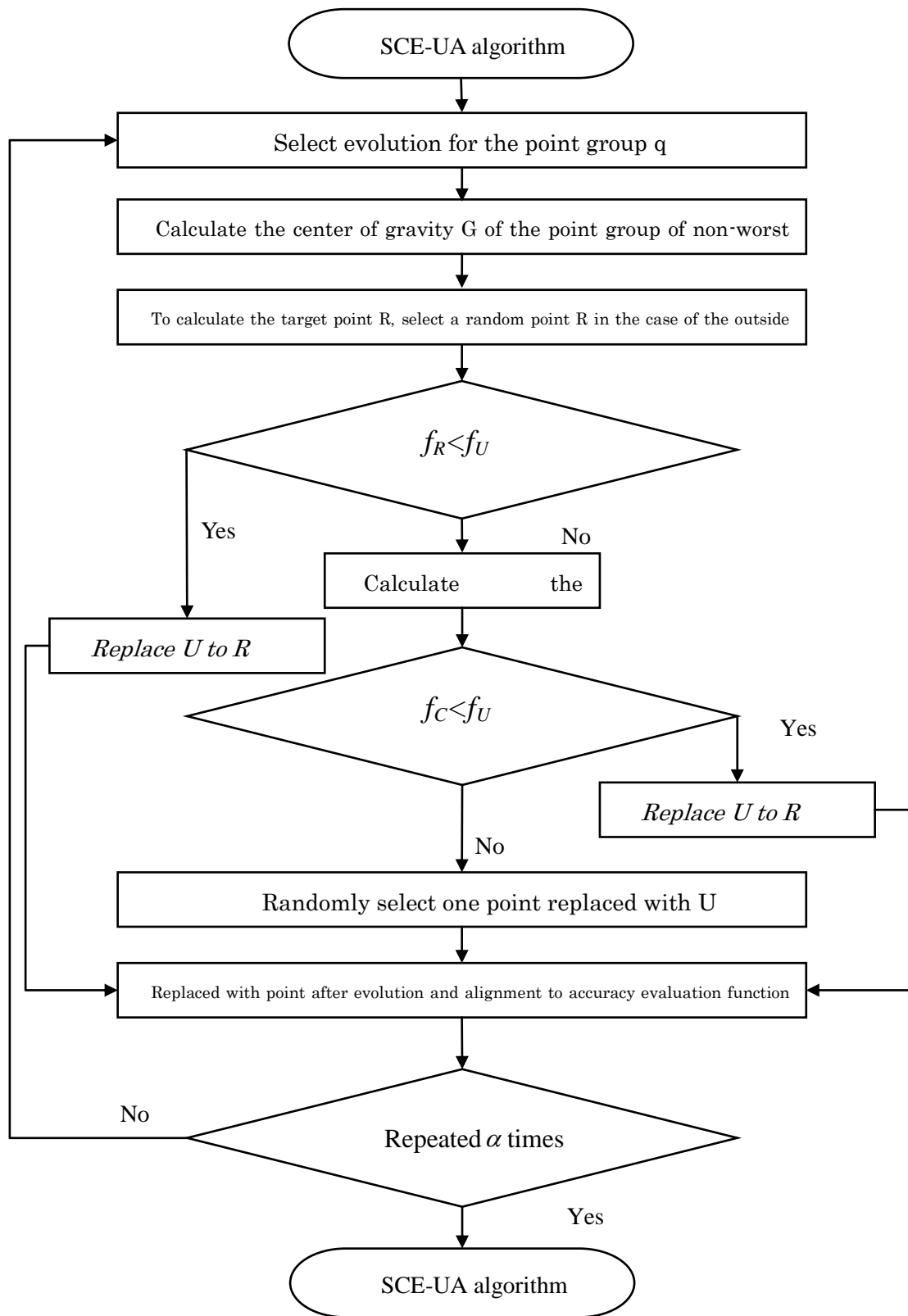


Figure 4.12 CCE Model system of algorithms

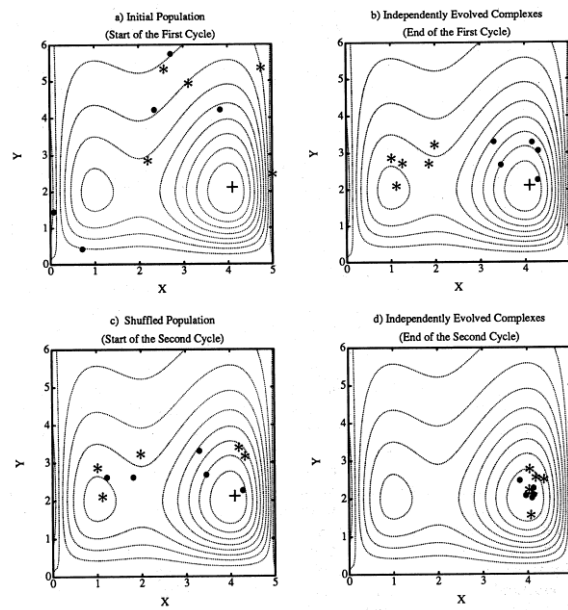


Figure 4.13 SCE-UA Function value transition diagram according to algorithm

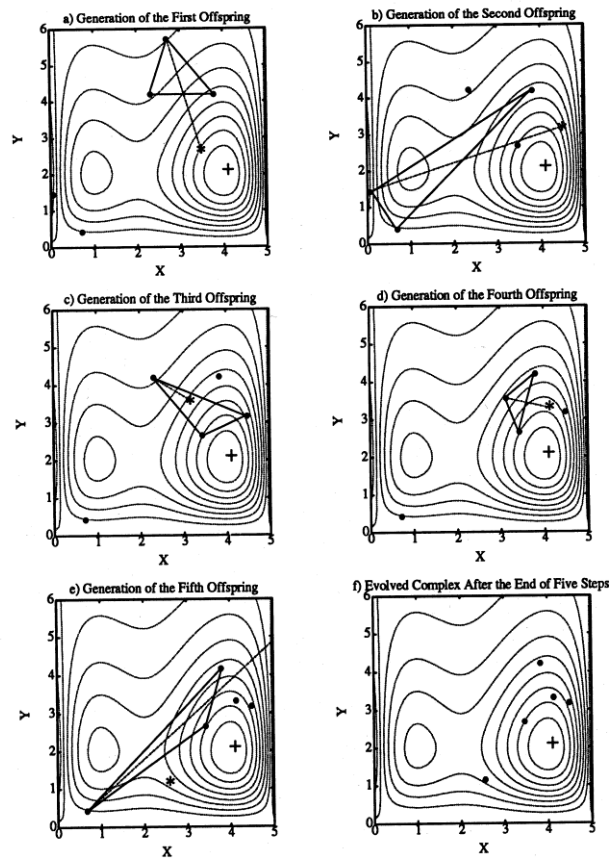


Figure 4.14 CCE Function value transition diagram according to algorithm

4.5 Observed discharge data from first class rivers

The overview of all the collected data from 9 first class rivers on Japanese Eastern Pacific coast will be given in this subchapter. All data was collected from online source of Ministry of Land, Infrastructure, Transport and Tourism (<http://www1.river.go.jp/>). For all rivers, we tried to collect the most downstream discharge and water level data station which was available. Our goal was to collect discharge and water level data for period 2008-2015 for all rivers, with exception of two the biggest rivers Tone and Abukuma where we collected data for period 2000-2015.

4.5.1 Takase river

We collected water level data from Takasegawa station, which is located 5.45 km from the river mouth and have basin area of 805.4 km². The available data was from 2008 to 2015. Discharge data was not available downstream from lake Ogawara, so we collected the data from 6 tributaries upstream of the lake Ueno, Dojogawa, Akagawa, Sadorogawa, Nakatsugawa and Anenumagawa, with total cumulative basin area of 600.3 km², of which 344.2 km² is from Ueno station from the main stream. The discharge data was available for period 2008 to 2012, so we obtained $Q-H$ curve for that period on the way that we combined total cumulative discharge data from 6 tributaries upstream of the lake Ogawara with water level data from Takasegawa station downstream from the lake Ogawara. We got projected rating curve formula $y = 323.85x^2 - 150.14x + 32.199$ with $R^2 = 0.4388$ and used it to obtain discharge data for period of 2013 to 2015, while for period 2008 to 2012 we used the total cumulative discharge data upstream from the lake Ogawara. Figure 4.15 shows water level and discharge data for Takasegawa station.

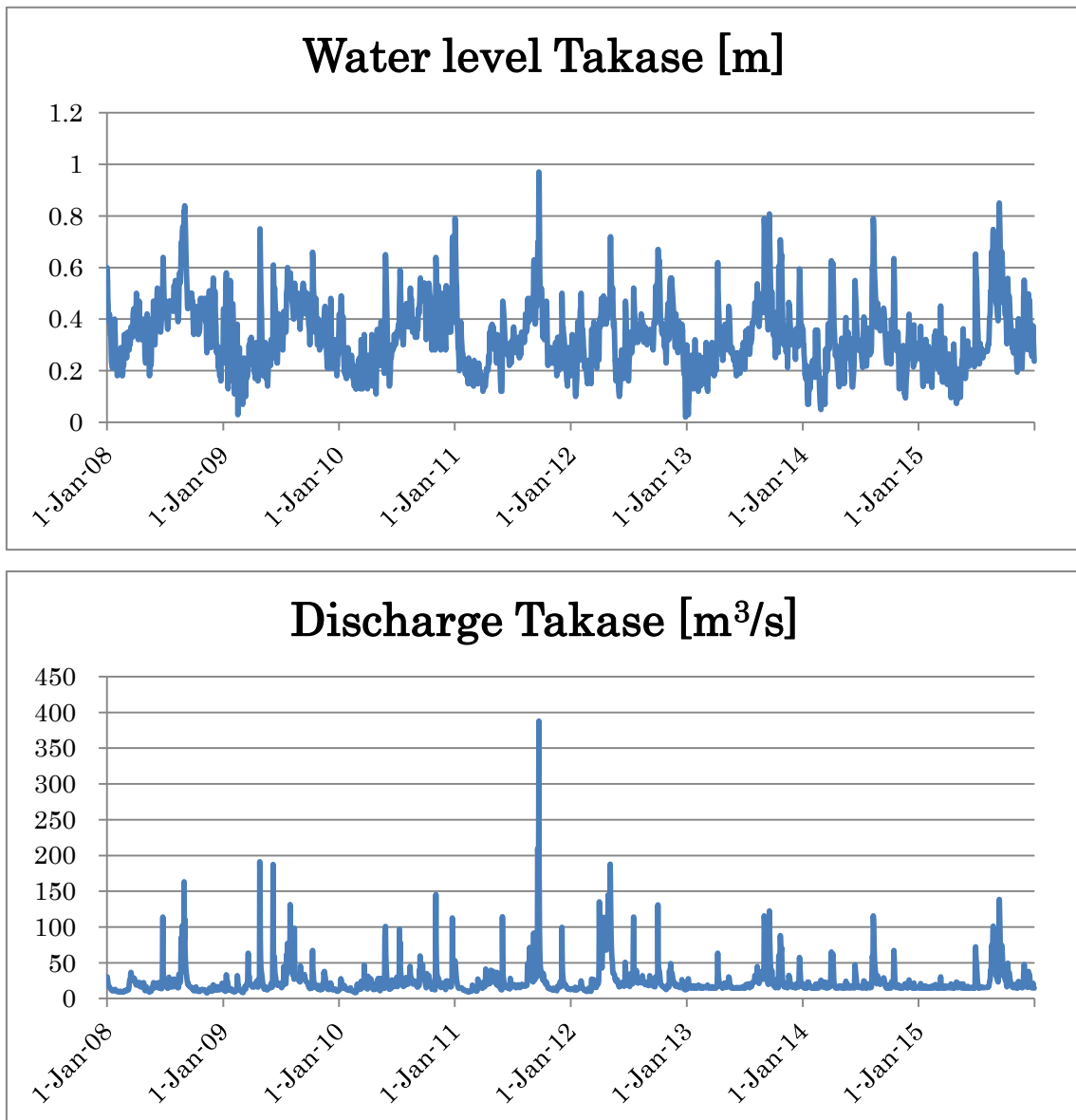


Figure 4.15 Water level and discharge data for Takasegawa station, Takase river

4.5.2 Mabechi river

We collected both water level and discharge data from Bridge station, which is located 4 km from the river mouth and have basin area of 2024 km². The available discharge data was from 2009 to 2013, and projected data for 2008, 2014 and 2015 based on observed water level data and Q-H curve. We obtained Q-H curve for the observed data and got projected rating curve formula $y = 49.422x^2 + 82.169x + 57.067$ with $R^2 = 0.9926$ and used it to obtain discharge data for 2008, 2014 and 2015. Figure

4.16 shows water level and discharge data for Bridge station.

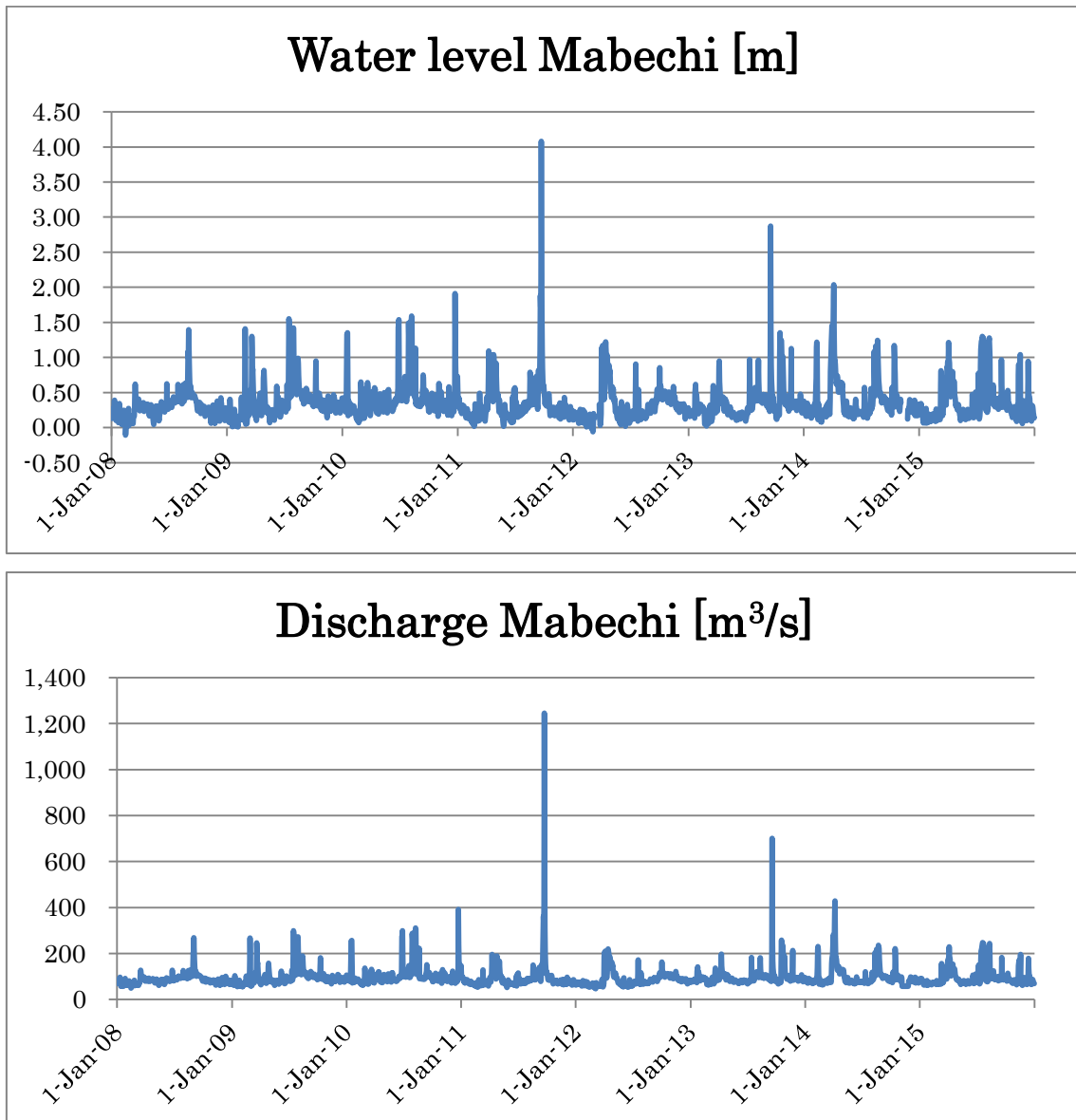


Figure 4.16 Water level and discharge data for Bridge station, Mabechi river

4.5.3 Kitakami river

We collected both water level and discharge data from Tome station, which is located 32.07 km from the river mouth and have basin area of 7869.4 km². The available discharge data was from 2008 to 2012, and projected data from 2013 to 2015 based on observed water level data and Q-H curve. We obtained Q-H curve for the observed data and got projected rating curve formula $y = 38.147x^2 + 182.49x - 988.92$ with $R^2 = 0.9816$

and used it to obtain discharge data from 2013 to 2015. Figure 4.17 shows water level and discharge data for Tome station. As Kitakami river has two river mouths, one natural and one artificial, we also collected data from station Wabuchi, which is located 21.78 km from the river mouth and have basin area of 1846.5 km². The data from Wabuchi station are not shown because we only collected data for targeted events Roke and Chataan which had available data so we didn't need to calculate Q-H relations for Wabuchi station.

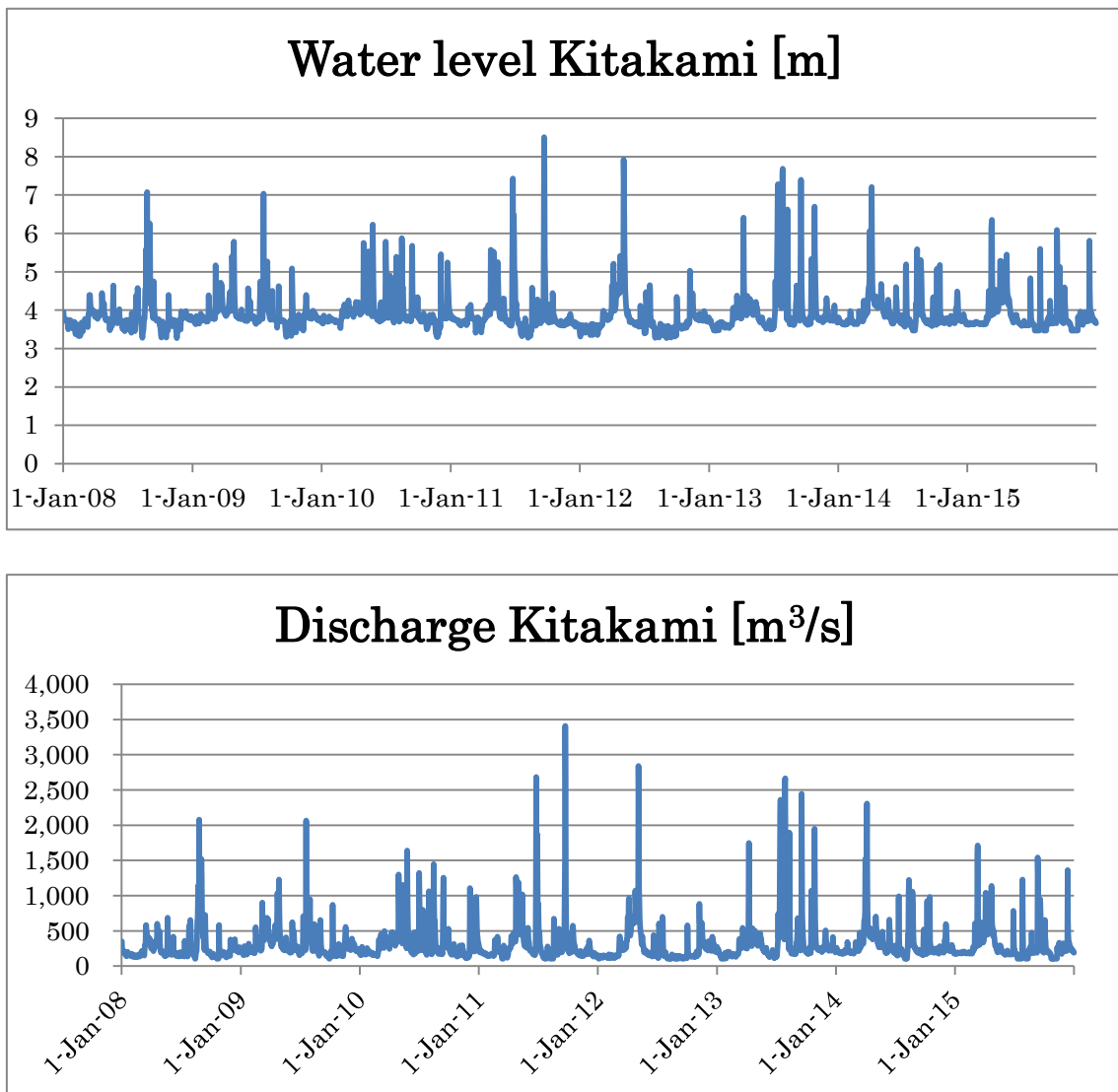


Figure 4.17 Water level and discharge data for Tome station, Kitakami river

4.5.4 Naruse river

We collected both water level and discharge data from two tributaries, Noda bridge and Hataya stations. Noda bridge is located 24.6 km from the river mouth and have basin area of 707 km² and Hataya is located 13.6 km from the river mouth and have basin area of 335 km². The available discharge data was from 2008 to 2012, and projected data from 2013 to 2015 based on observed water level data and Q-H curve. We obtained Q-H curve for the observed data and got projected rating curve formula $y = 45.982x^2 + 22.939x - 2.1185$ with $R^2 = 0.9834$ for Noda bridge and $y = 13.382x^2 - 3.472x - 13.021$ with $R^2 = 0.9897$ for Hataya and used it to obtain discharge data from 2013 to 2015. The main tributary station Nobiru 1 located 0.5 km from the river mouth and have basin area of 1158.4 km² had available water level data from 2008 to 2015, and we projected discharge data from 2008 to 2015 as a sum of discharge data from Noda bridge and Hataya stations. Figure 4.18 shows water level and discharge data for Nobiru 1 station.

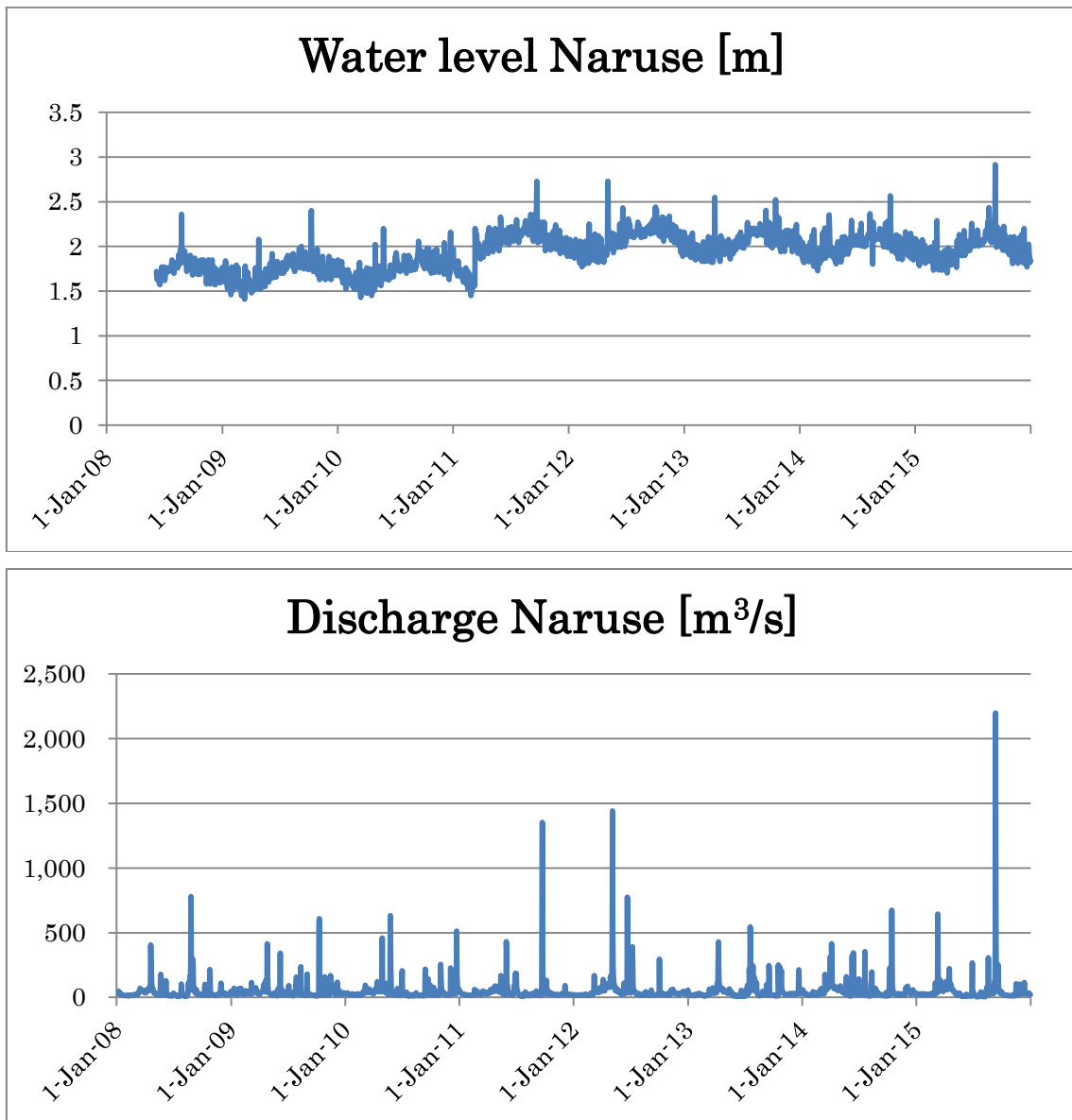


Figure 4.18 Water level and discharge data for Nobiru 1 station, Naruse river

4.5.5 Natori river

We collected both water level and discharge data from Yuriage 2 station, which is located 0.69 km from the river mouth and have basin area of 776 km². The available discharge data was from 2008 to 2009 and first half of 2013, and projected data from 2010 to 2015 except first half of 2013 based on observed water level data and Q-H curve. We obtained Q-H curve for the observed data period from 2008 to 2009 and got projected rating curve formula $y = 320.07x^2 + 287.54x + 81.172$ with $R^2 = 0.8888$ and used it to

obtain discharge data from 2010 to 2015. Figure 4.19 shows water level and discharge data for Yuriage 2 station.

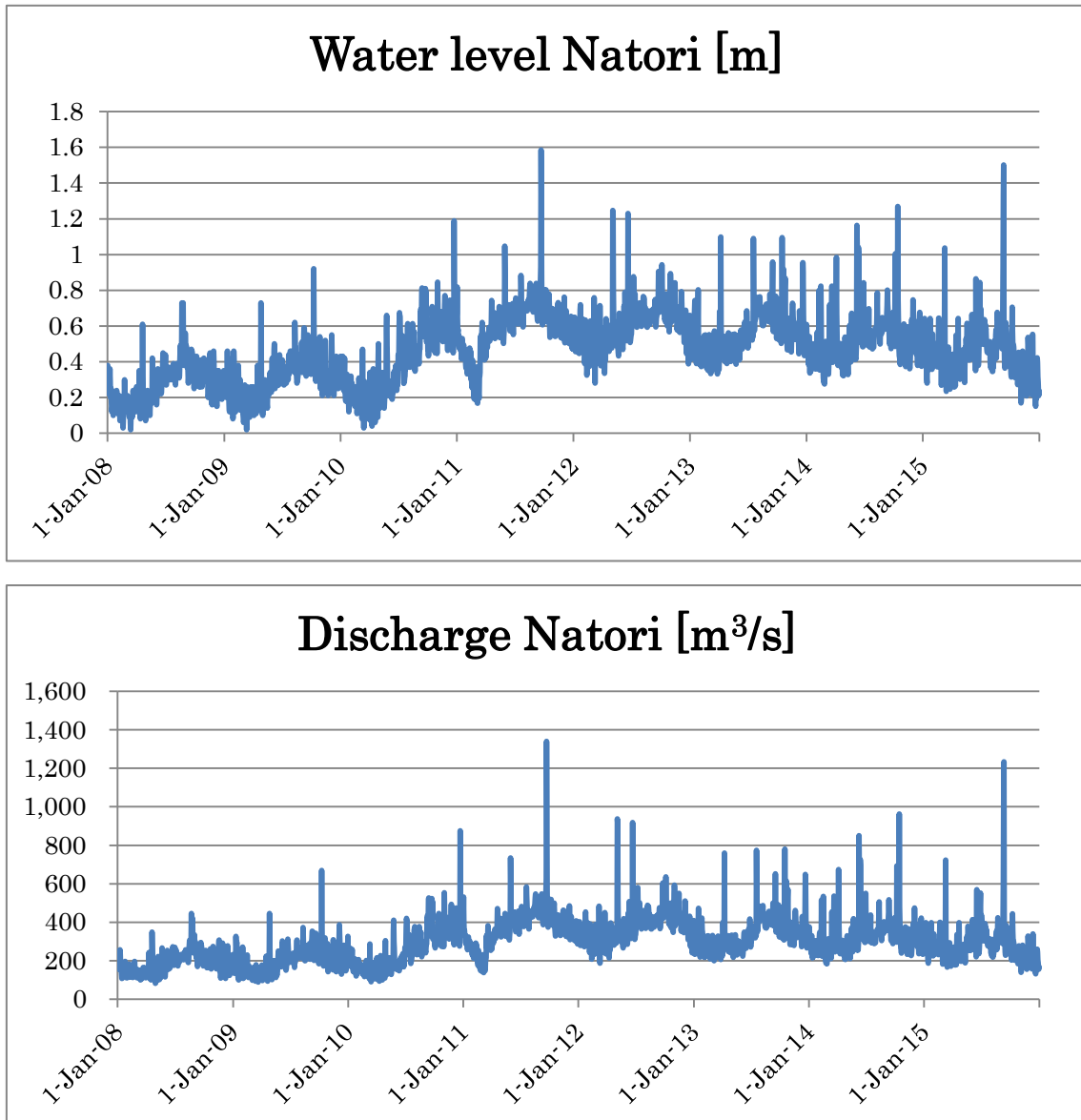


Figure 4.19 Water level and discharge data for Yuriage 2 station, Natori river

4.5.6 Abukuma river

We collected both water level and discharge data from Iwanuma station, which is located 8.07 km from the river mouth and have basin area of 5625 km². The available discharge data was from 2001, 2008, 2009 and first half of 2013, and projected data the remaining periods from 2000 to 2015 based on observed water level data and Q-H curve.

We obtained Q-H curve for the observed data period from 2008 to 2009 and got projected rating curve formula $y = 117x^2 + 213.1x + 114.56$ with $R^2 = 0.9643$ and used it to obtain remaining discharge data from 2000 to 2015. Figure 4.20 shows water level and discharge data for Iwanuma station.

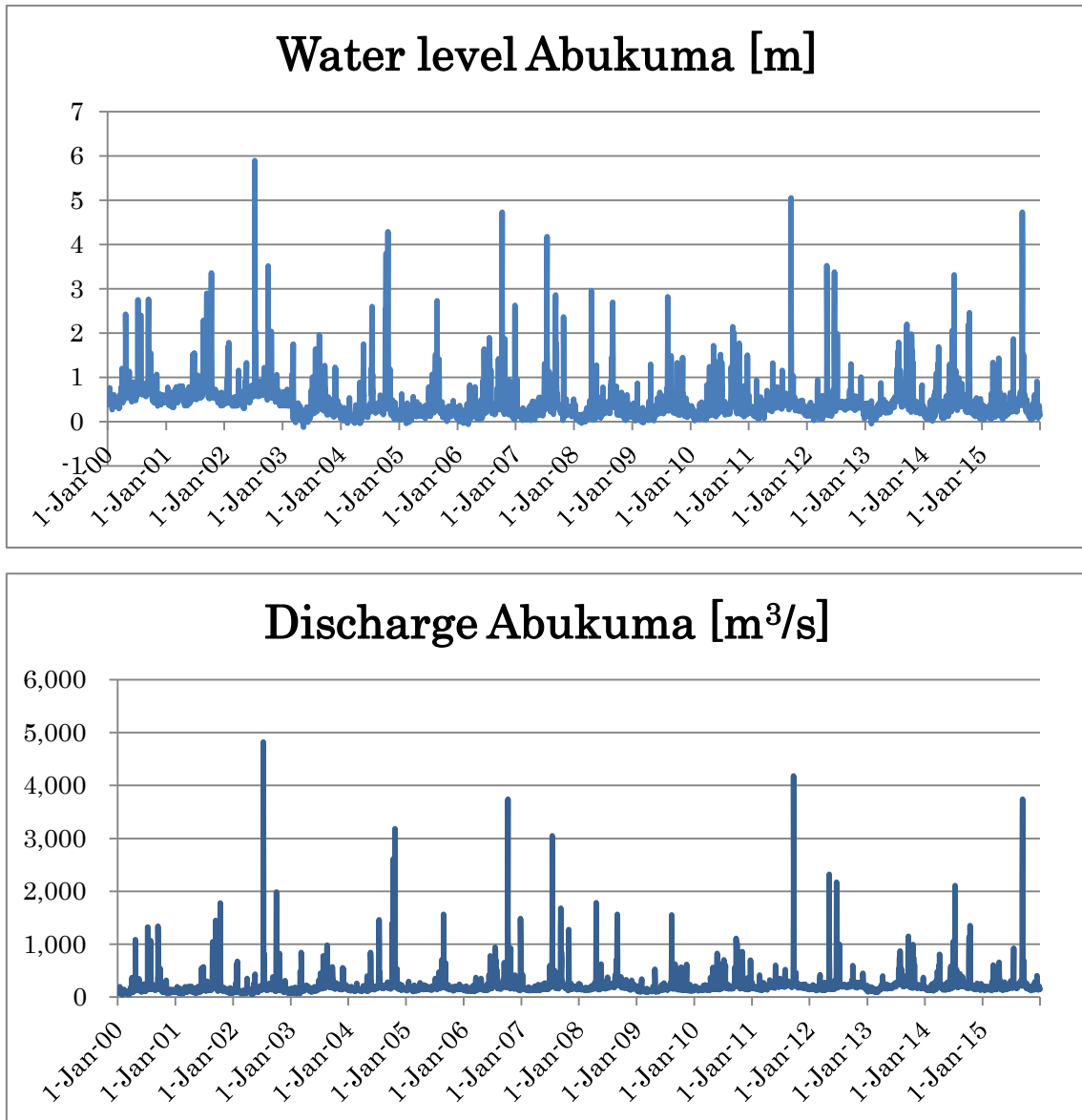


Figure 4.20 Water level and discharge data for Iwanuma station, Abukuma river

4.5.7 Kuji river

We collected both water level and discharge data from Sakaki bridge station, which is located 4.5 km from the river mouth and have basin area of 1442 km². The

available discharge data was from 1999 to 2001, and projected data from 2008 to 2015 based on observed water level data and Q-H curve. We obtained Q-H curve for the observed data period from 1999 to 2001 and got projected rating curve formula $y = 64.54x^2 + 27.797x + 4.4875$ with $R^2 = 0.9866$ and used it to obtain remaining discharge data from 2008 to 2015. Figure 4.21 shows water level and discharge data for Sakaki bridge station.

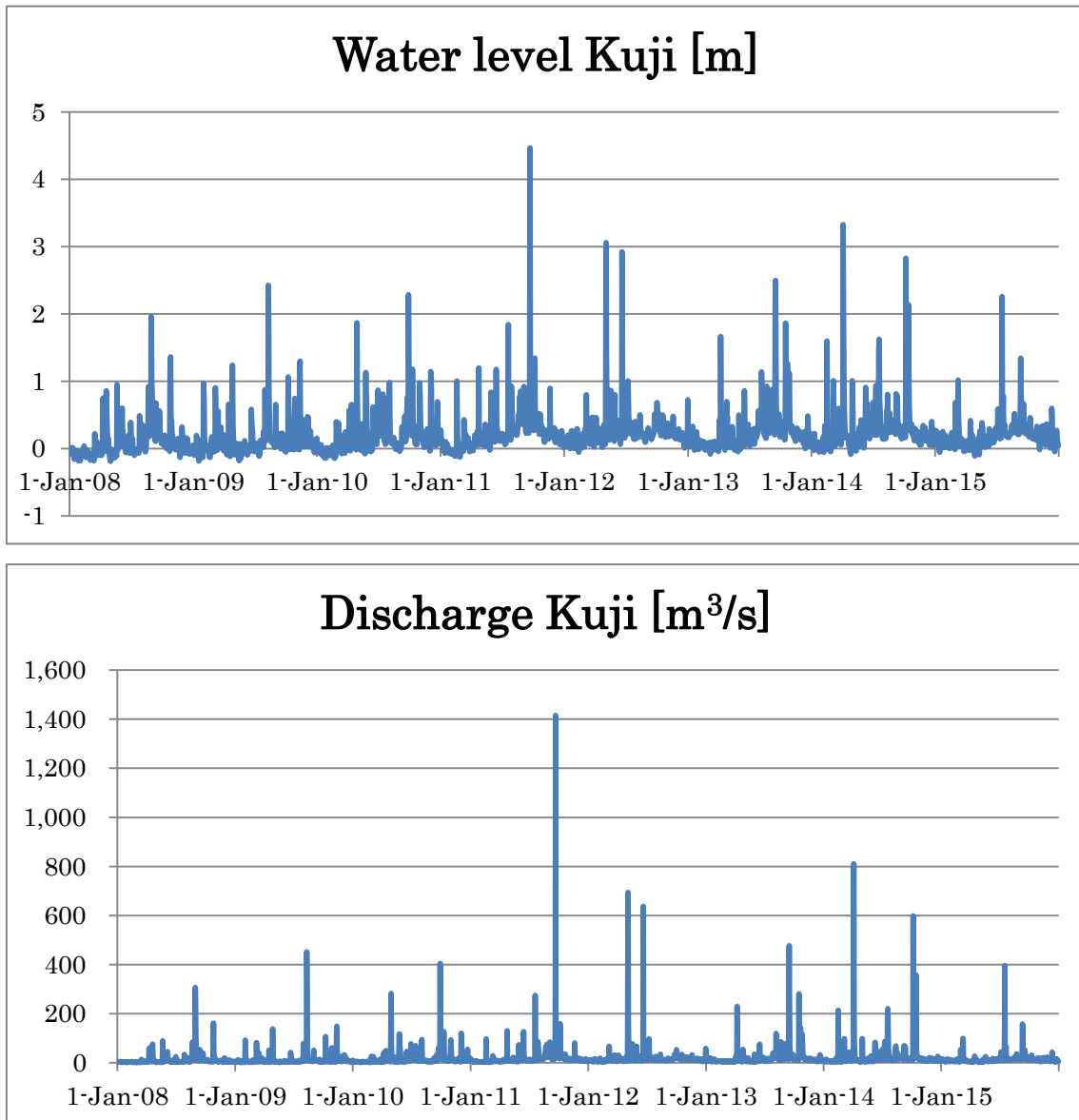


Figure 4.21 Water level and discharge data for Sakaki bridge station, Kuji river

4.5.8 Naka river

We collected both water level and discharge data from Suifu bridge station, which is located 12.4 km from the river mouth and have basin area of 2552 km². The available discharge data was from 1999 to 2001, and projected data from 2008 to 2015 based on observed water level data and Q-H curve. We obtained Q-H curve for the observed data period from 1999 to 2001 and got projected rating curve formula $y = 56.54x^2 + 11.293x + 266.43$ with $R^2 = 0.9558$ and used it to obtain remaining discharge data from 2008 to 2015. Figure 4.22 shows water level and discharge data for Suifu bridge station.

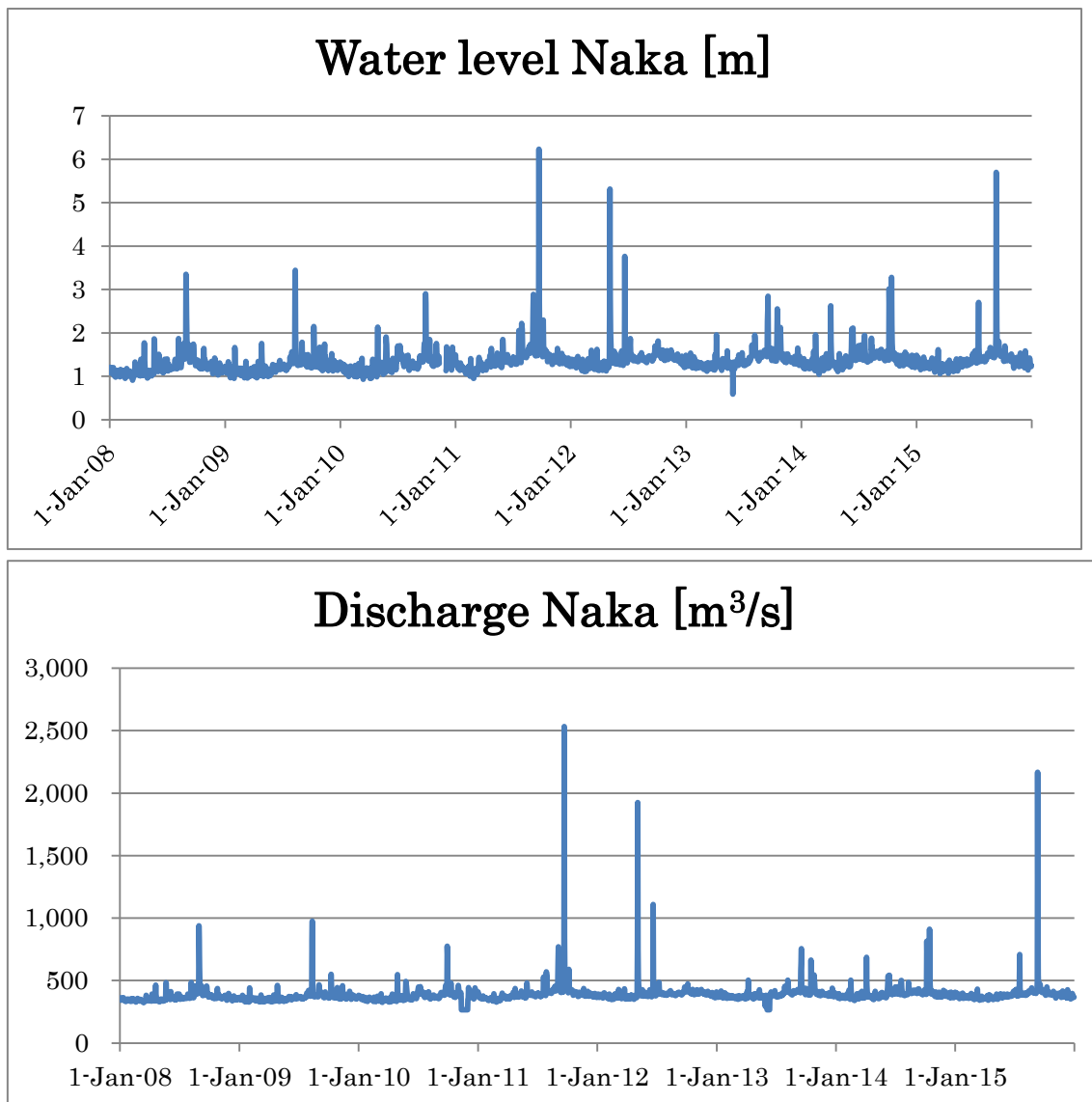


Figure 4.22 Water level and discharge data for Suifu bridge station, Naka river

4.5.9 Tone river

We collected both water level and discharge data from Nunokawa station, which is located 76.47 km from the river mouth and have basin area of 12458 km². The available discharge data was from 2000 to 2008, and projected data from 2009 to 2015 based on observed water level data and Q-H curve. We obtained Q-H curve for the observed data period from 2000 to 2008 and got projected rating curve formula $y = 47.171x^2 + 536.68x - 540.97$ with $R^2 = 0.9266$ and used it to obtain remaining discharge data from 2009 to 2015. Figure 4.23 shows water level and discharge data for Nunokawa station.

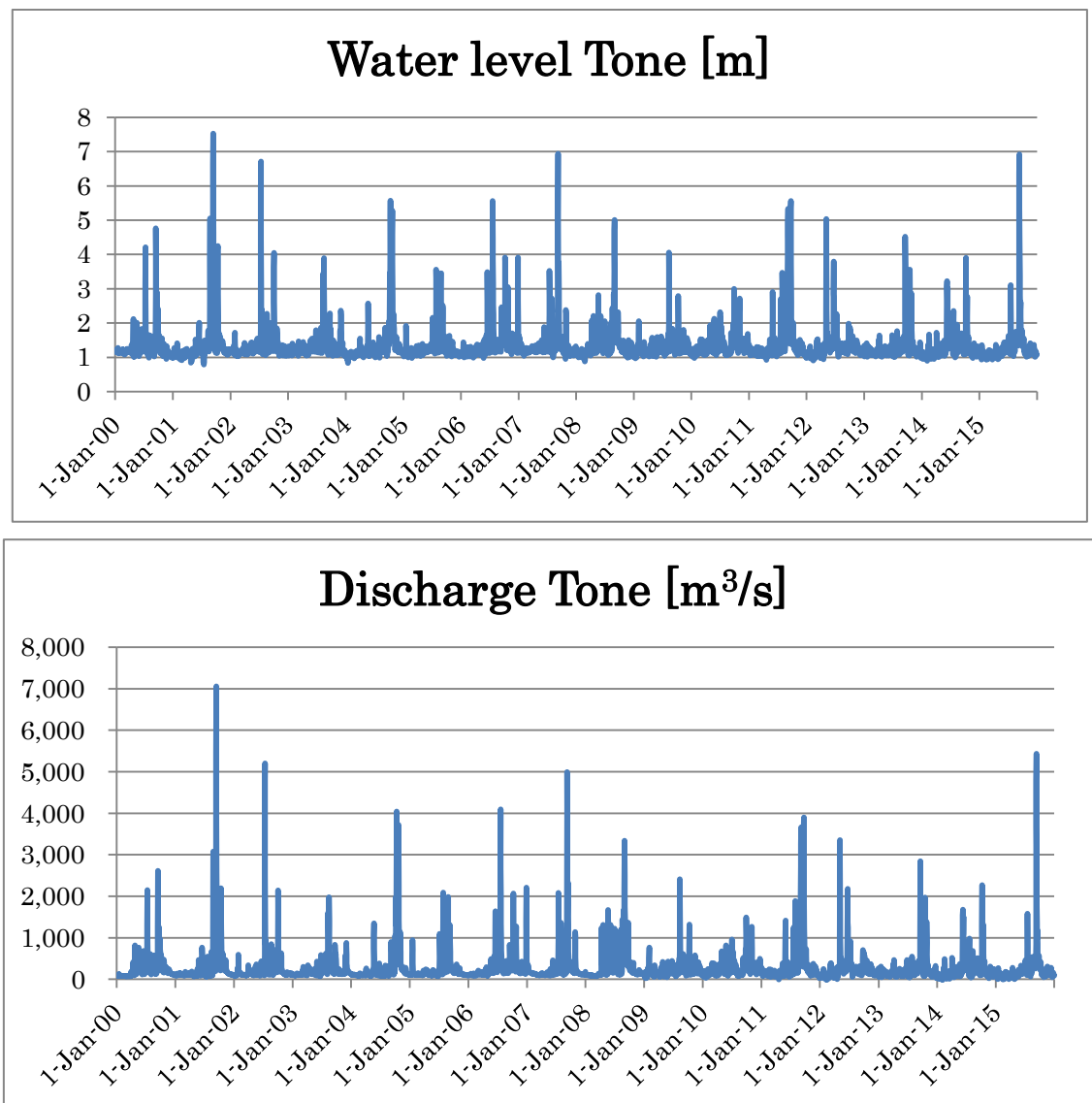


Figure 4.23 Water level and discharge data for Nunokawa station, Tone river

4.6 Calculation conditions and methods

We simulated numerical prediction of total freshwater outflow at river mouths from all of 9 first class river basins flowing from eastern Japanese coast to western Pacific ocean for targeted event typhoons Roke from 19/09/2011 at noon to 26/09/2011 at noon and Chataan from 8/07/2002 at noon to 15/07/2002 at noon.

For 2 rivers (Takase, Tone) the simulation was not made at river mouth but on the most downstream available discharge stations Ueno and Nunokawa respectively, because we didn't have any discharge data available close to river mouth.

Observed rainfall data (hourly) was collected from online source of Japan Meteorological Agency (www.data.jma.go.jp/risk/obsdl/index.php#). Observed discharge and dam data was collected from online source of Ministry of Land, Infrastructure, Transport and Tourism (www1.river.go.jp/). When we didn't have observed discharge data for our targeted event, then we obtained it by using stage-discharge relationships (Q-H curves), as described in chapter 3.5 for each river.

We neglected tidal effect from the calculation and observations. We chose observation station to be enough close to the river mouth to accurately represent river mouth discharge but enough far from river mouth to not be affected by tides. For example, for Naruse river we didn't choose the most downstream Yuriage II station because its data were too much affected by tides.

For Tone, Kitakami and Abukuma rivers we calculated dam effect using observed dam data, with conditions that if inflow to the dam is bigger than maximum observed outflow, then outflow from the dam becomes maximum observed outflow.

We assumed a uniform landuse because most of the area was covered by forest and its soil depth equals to 1000 mm. The other model parameters (soil roughness coefficient N_{slo} , river roughness coefficient N_{riv} , effective porosity θ_a , saturated hydraulic conductivity k_a , effective rainfall FI) were optimized by using SCE-UA method. We optimized parameters based on typhoon Roke data and validated with typhoon Chataan data and vice versa. We were searching which optimization (Roke or Chataan) shows better optimized and validated accuracy evaluation NS coefficients. Optimized parameters for input to SCE-UA algorithm were chosen as follows:

(initial; minimum; maximum)

N_{slo} : 0.6; 0.1; 1

N_{riv} : 0.03; 0.01; 0.1

θ_a : 0.4; 0.1; 0.7

k_a [m/s]: 0.05; 0.005; 0.5

FI : 1; 0.6 (0.4 for Tone); 1

Parameters which were not optimized (constant value used):

$$\theta m: 0$$

$$\beta: 4 \text{ (Value of } \beta \text{ is not important when } \theta m = 0 \text{)}$$

We chose $\theta m = 0$ in order to simplify SCE-UA optimization by conducting optimization in respect to 5 instead of 7 parameters. By choosing $\theta m = 0$, we neglected influence of capillary subsurface flow but we thought it is justified given the conditions that we simulate extreme discharge event which quickly becomes surface flow so we assumed influence of capillary subsurface flow to be negligible for our type of study and our goals.

We extended the range of usage of the model by applying simulated data to joint hydrological-oceanographic model JCOPE-T-NEDO (Varlamov et al., 2015) from Japan Agency for Marine-Earth Science and Technology (JAMSTEC) for modeling of coastal processes, in order to show an example of further studies and applicability of the present study.

4.6.1 Initial data preparation

We used ArcGIS software version 10.2.2. (ESRI, 2016) for comprehensively managing and processing the data with information about the position (spatial data), visually display the data, and use a technology that enables sophisticated data analysis. ArcGIS has been used in wide range of fields for urban planning and resource management in recent years. By using ArcGIS, we made it possible to make effective use of a computer geographic information. The following steps were applied to prepare initial topography and rainfall data for the model:

a) Hydrosheds datasets for Digital Elevation Model (DEM), Flow Accumulation (ACC) and Flow Direction (DIR) were downloaded from U.S. Geological Survey (<http://hydrosheds.cr.usgs.gov/index.php>). We downloaded 15 arc-seconds (about 500 m resolution) GRID data for DEM, ACC and DIR datasets.

b) Based on global DIR data with ending point at the river mouth, we delineated targeted river basin by using "Watershed" ArcGIS function. DIR data compares the altitude of neighboring eight directions in each cell, which is tracking the steepest gradient direction through which the rain that falls in the basin travels.

c) Based on delineated watershed, we extracted DEM, ACC and DIR data from global Hydrosheds dataset applied to the targeted basin. For later input to the model, we convert these data and all other data produced by ArcGIS from raster to ASCII format.

d) Based on collected rainfall data, we input the latitudinal and longitudinal position

of each rainfall station to the ArcGIS. From these information, we create Thiessen polygon by using "Create Thiessen Polygon" tool. We convert the data format from polygon to raster and from raster to ASCII.

e) By inputting DIR data and coordinates of river mouth into cell distributed sub-model mkbsn.exe, we produce order.txt and bsndir.txt files in proper format to be used for the model simulation. Order.txt file provides the model with information about order of calculation for every cell in the basin, while bsndir.txt provides flow direction data but in format proper for usage in the simulation.

f) At this step, we manually change cell size within files from 0.0041666667 degree to 460 meters because cell distributed model calculated slope and length of each slope with using metrics system. By inputting DEM and bsndir.txt into cell distributed sub-model mkslp.exe, we produce slope.txt and length.txt files which contain data about slope gradient and length respectively for the whole basin.

g) We produce landuse.txt file, by putting value "1" to all cells within the file, which needs to be equal like total number of cells for the targeted basin.

h) Before inputting the data to the model, we manually change cell size within files from 0.0041666667 degree to 460 meters because cell distributed model uses metrics system for simulation. We input the topography and rainfall data and produced model files into the cell distributed model. With using these data, we perform discharge simulation and identify parameters. Furthermore, we optimize identified parameters by using SCE-UA method.

4.6.1.1 Takase

The most downstream discharge station Ueno (27.60 km from the river mouth, basin area 344.2 km²) is separated from the ocean with lake Ogawara so we optimized parameters for data from the cell where is the station instead of from river mouth cell, and later with optimized parameters simulated discharge on the river mouth.

Figure 4.24 shows delineated Flow Accumulation data, with position of rainfall stations (blue dots) with belonging Thiessen polygons and observation station Ueno (red dot) for the Takase basin.

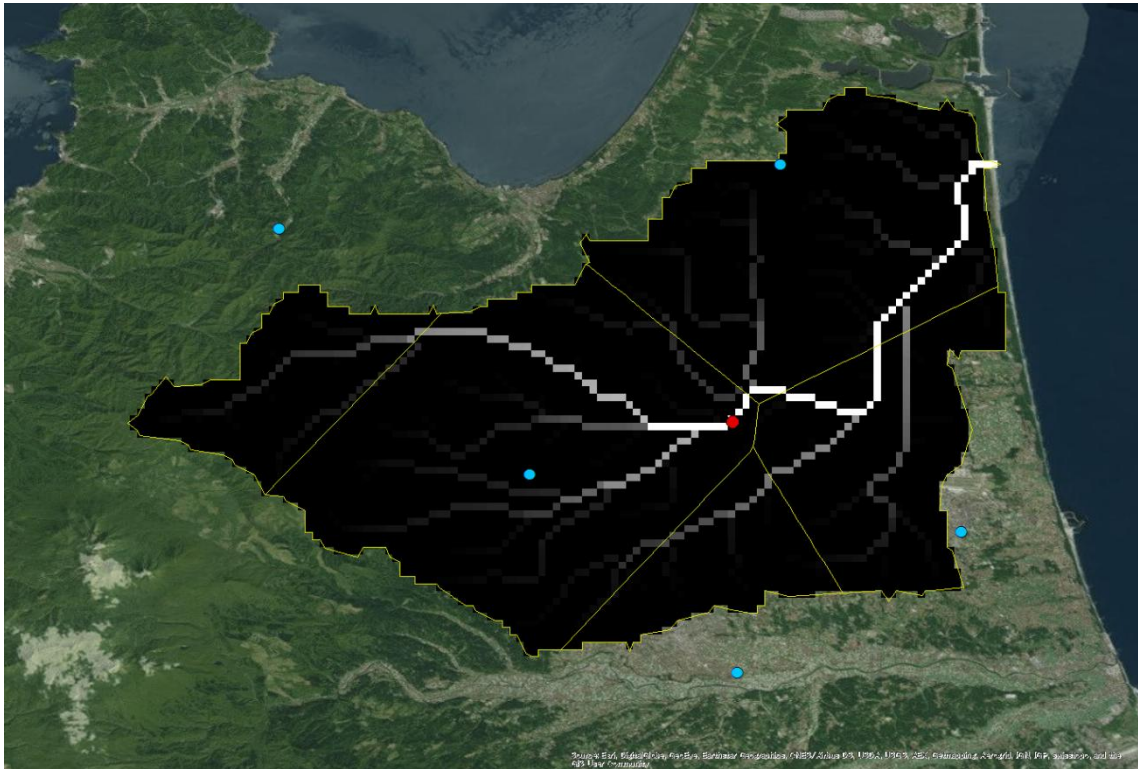


Figure 4.24 Delineated Flow Accumulation data, with position of rainfall stations (blue dots) with belonging Thiessen polygons and observation station Ueno (red dot) for the Takase basin

Figure 4.25 shows delineated Digital Elevation Model (DEM) with spatial resolution of 460 m, while Figure 4.26 shows delineated Flow Direction map for the Takase basin.

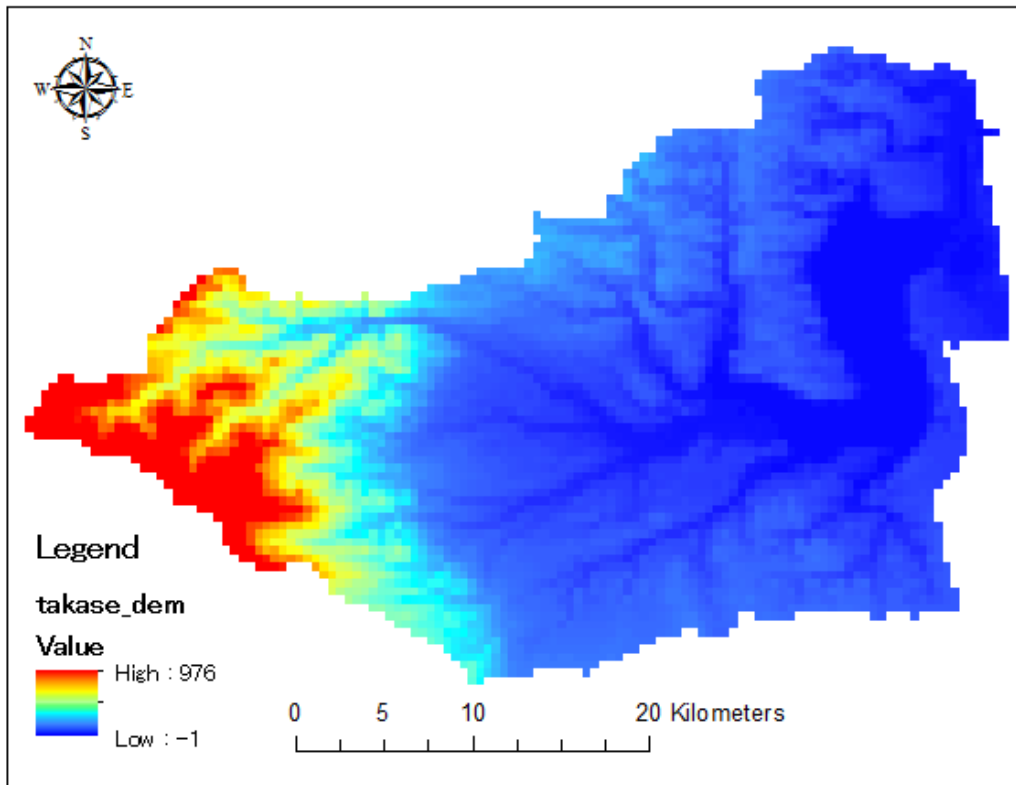


Figure 4.25 Digital Elevation Model (DEM) for the Takase basin (460 m resolution)

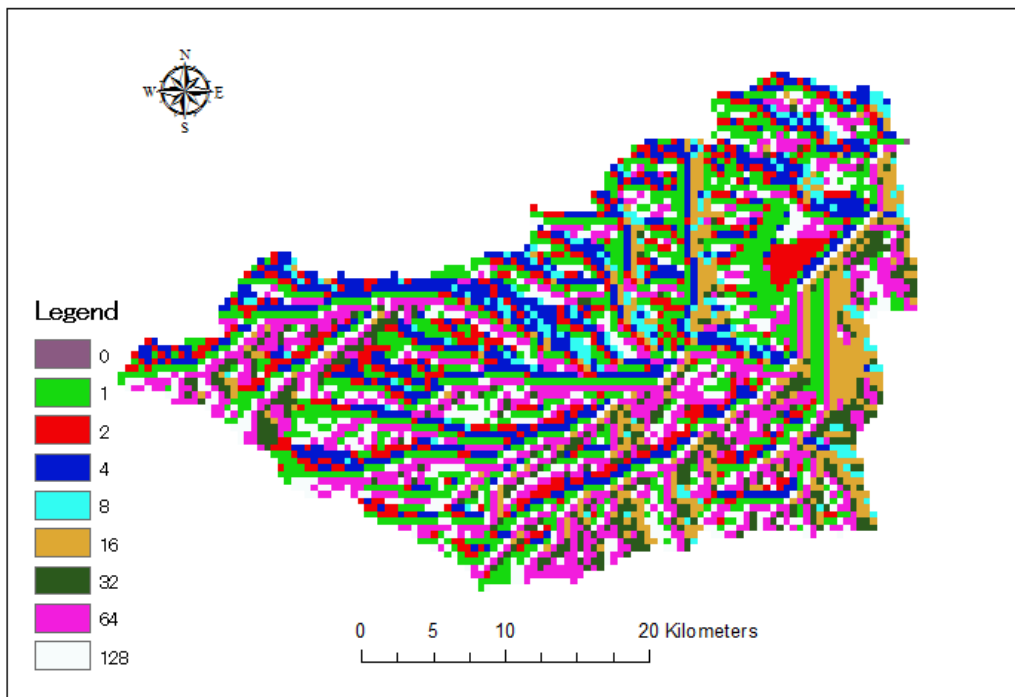


Figure 4.26 Delineated Flow Direction map for the Takase basin

4.6.1.2 Mabechi

Parameters for data from the most downstream discharge station Bridge (4 km from the river mouth, basin area 2024 km²) were optimized with simulated discharge on the river mouth.

Figure 4.27 shows delineated Flow Accumulation data, with position of rainfall stations (blue dots) with belonging Thiessen polygons and observation station Bridge (red dot) for the Mabechi basin.

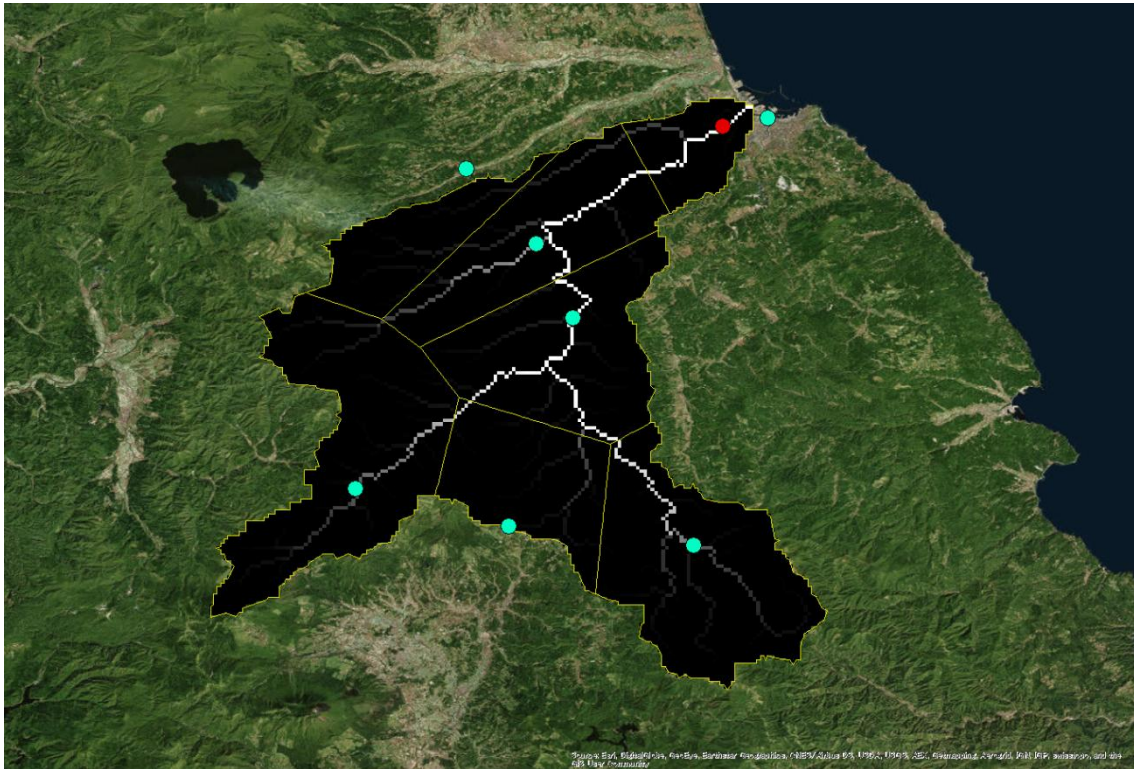


Figure 4.27 Delineated Flow Accumulation data, with position of rainfall stations (blue dots) with belonging Thiessen polygons and observation station Bridge (red dot) for the Mabechi basin

Figure 4.28 shows delineated Digital Elevation Model (DEM) with spatial resolution of 460 m, while Figure 4.29 shows delineated Flow Direction map for the Mabechi basin.

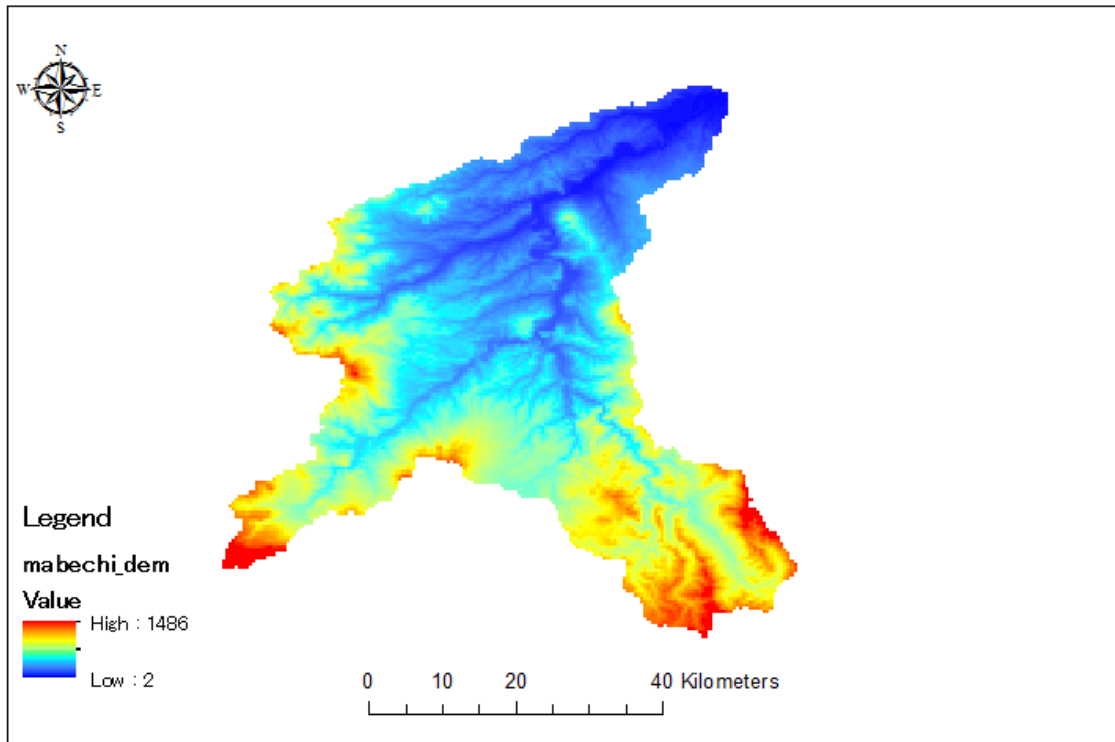


Figure 4.28 Digital Elevation Model (DEM) for the Mabeche basin (460 m resolution)

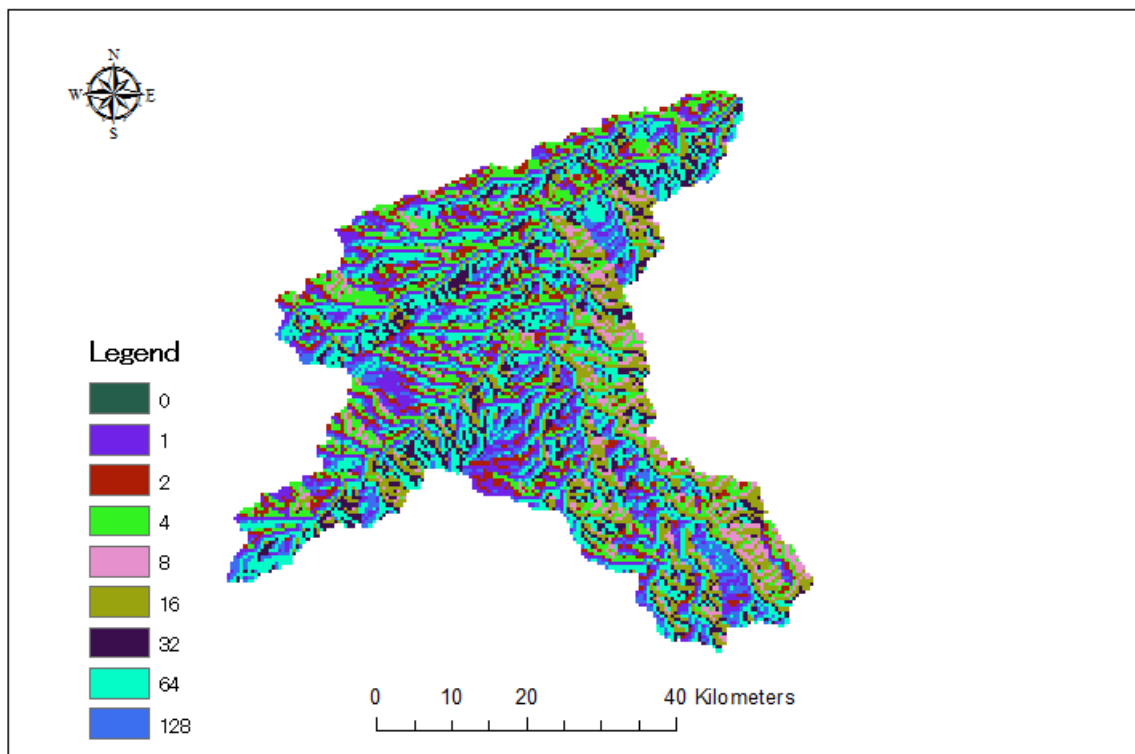


Figure 4.29 Delineated Flow Direction map for the Mabeche basin

4.6.1.3 Kitakami

Parameters for summarized discharge values from stations Tome (32.07 km from the river mouth, basin area 7896.4 km²) and the most downstream station Wabuchi (21.78 km from the river mouth, basin area 1846.5 km²) were optimized with simulated discharge on the old river mouth (Ishinomaki). Later on, we obtained the simulated results for station Tome and used those as representative of new river mouth, while difference between river mouth simulation and Tome simulation values were used as representative simulated values for Wabuchi station and old river mouth. Figure 4.30 shows delineated Flow Accumulation data, with position of rainfall stations (blue dots) with belonging Thiessen polygons and observation stations Tome and Wabuchi (red dots) for the Kitakami basin. Green dot shows separation point between old river mouth (Wabuchi station) and new river mouth (Tome station).

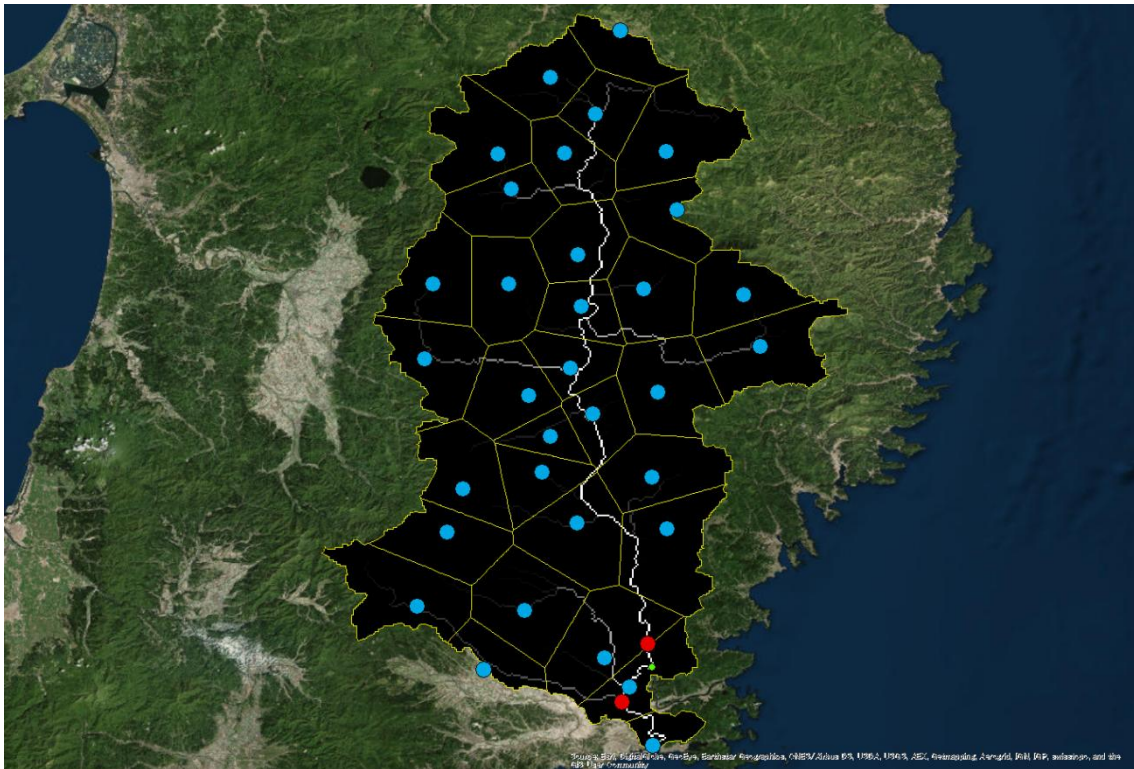


Figure 4.30 Delineated Flow Accumulation data, with position of rainfall stations (blue dots) with belonging Thiessen polygons and observation stations Tome and Wabuchi (red dots) for the Kitakami basin

Figure 4.31 shows delineated Digital Elevation Model (DEM) with spatial resolution of 460 m, while Figure 4.32 shows delineated Flow Direction map for the Kitakami basin.

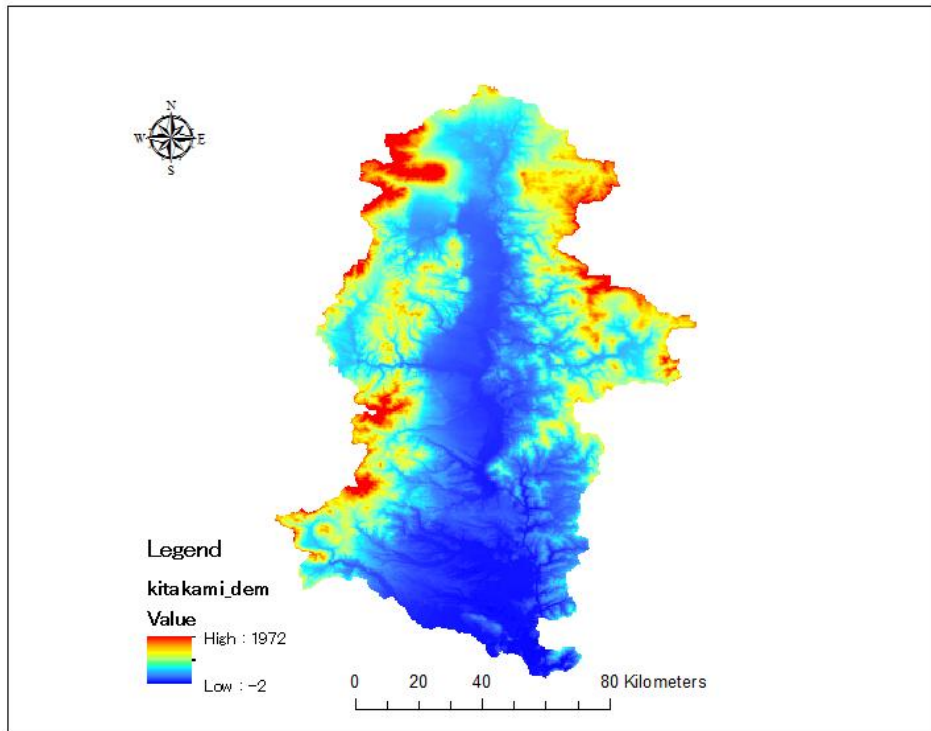


Figure 4.31 Digital Elevation Model (DEM) for the Kitakami basin (460 m resolution)

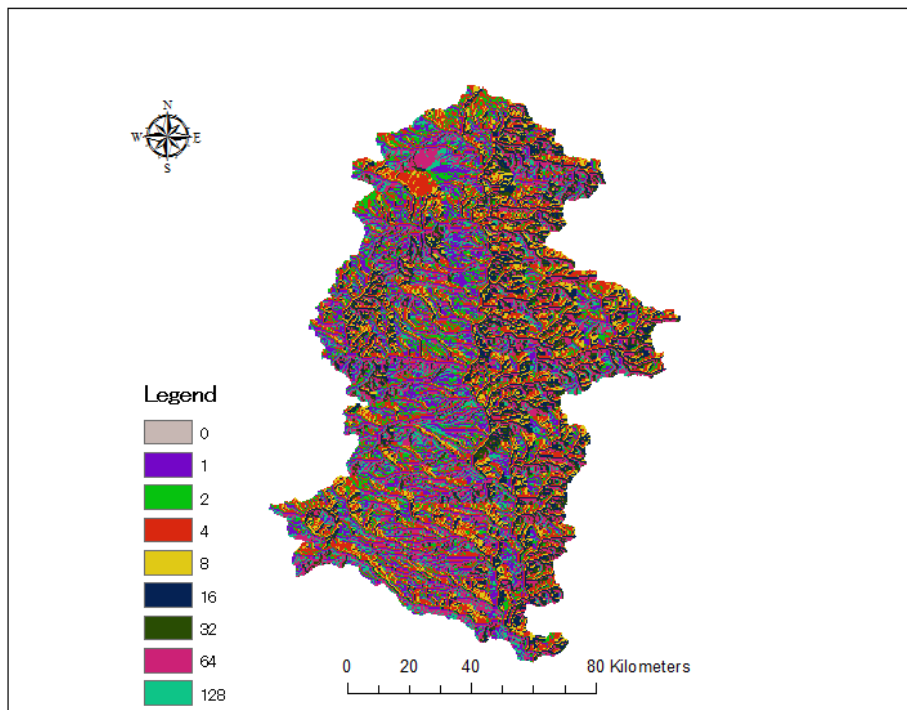


Figure 4.32 Delineated Flow Direction map for the Kitakami basin

4.6.1.4 Naruse

Parameters for summarized discharge values from stations of two main tributaries Noda (24.6 km from the river mouth, basin area 707 km²) and Hataya (13.6 km from the river mouth, basin area 335 km²) were optimized with simulated discharge on the river mouth. Figure 4.33 shows delineated Flow Accumulation data, with position of rainfall stations (blue dots) with belonging Thiessen polygons and observation stations Noda and Hataya (red dots) for the Naruse basin.

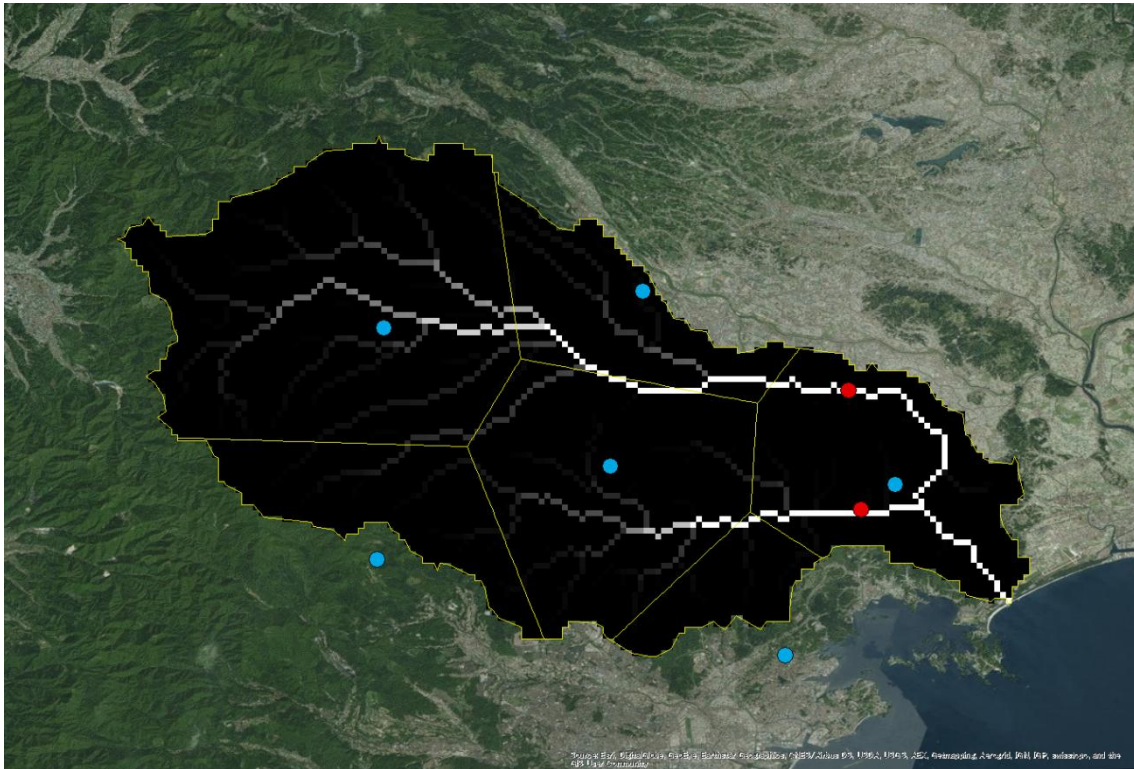


Figure 4.33 Delineated Flow Accumulation data, with position of rainfall stations (blue dots) with belonging Thiessen polygons and observation stations Noda and Hataya (red dots) for the Naruse basin

Figure 4.34 shows delineated Digital Elevation Model (DEM) with spatial resolution of 460 m, while Figure 4.35 shows delineated Flow Direction map for the Naruse basin.

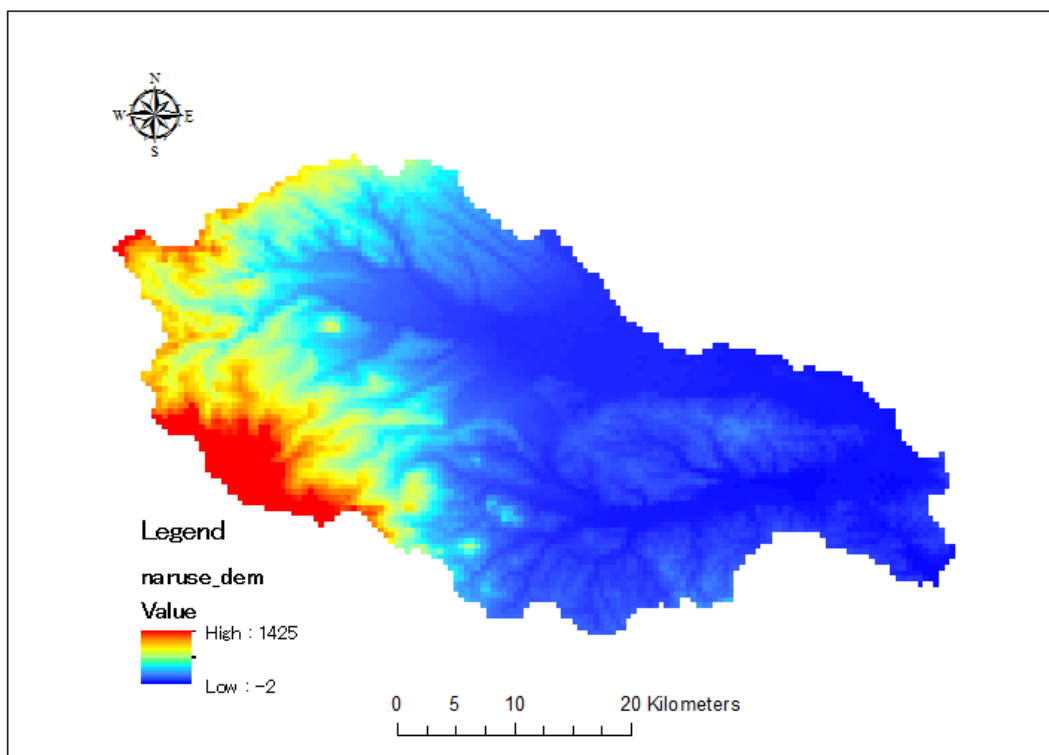


Figure 4.34 Digital Elevation Model (DEM) for the Naruse basin (460 m resolution)

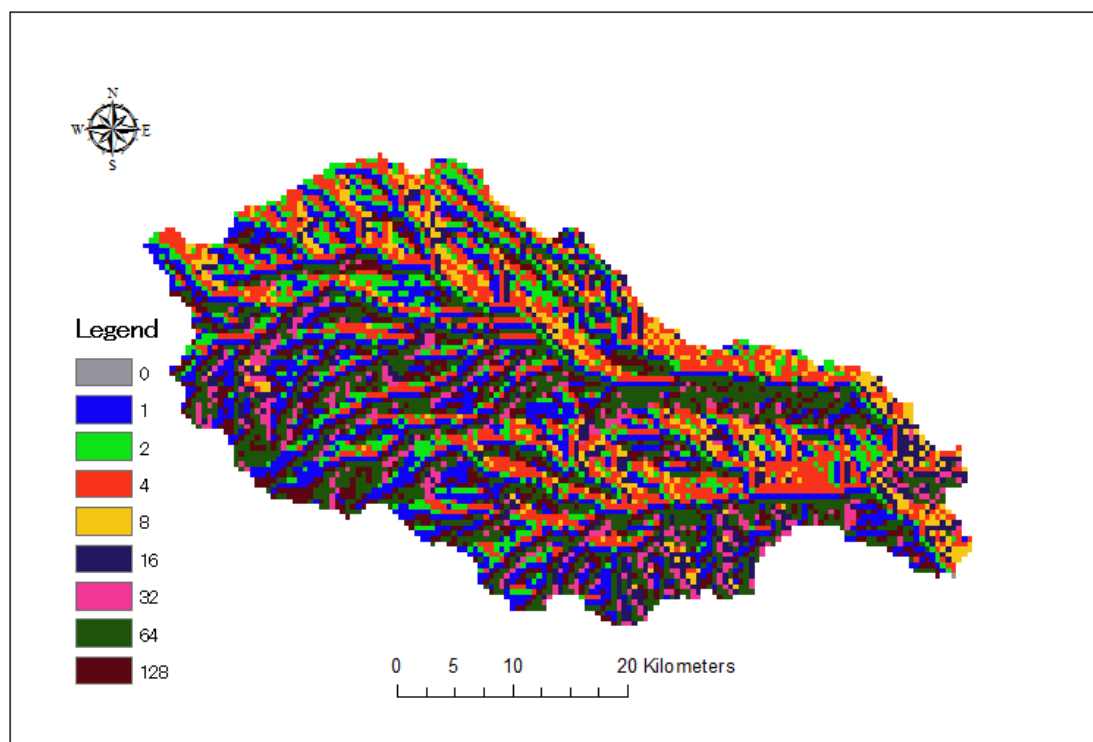


Figure 4.35 Delineated Flow Direction map for the Naruse basin

4.6.1.5 Natori

Parameters for summarized discharge values from stations of two main tributaries Natoribashi (8.26 km from the river mouth, basin area 431 km²) and Hirosebashi (3.55 km from the river mouth, basin area 309 km²) were optimized with simulated discharge on the river mouth. Figure 4.36 shows delineated Flow Accumulation data, with position of rainfall stations (blue dots) with belonging Thiessen polygons and observation stations Natoribashi and Hirosebashi (red dots) for the Natori basin.

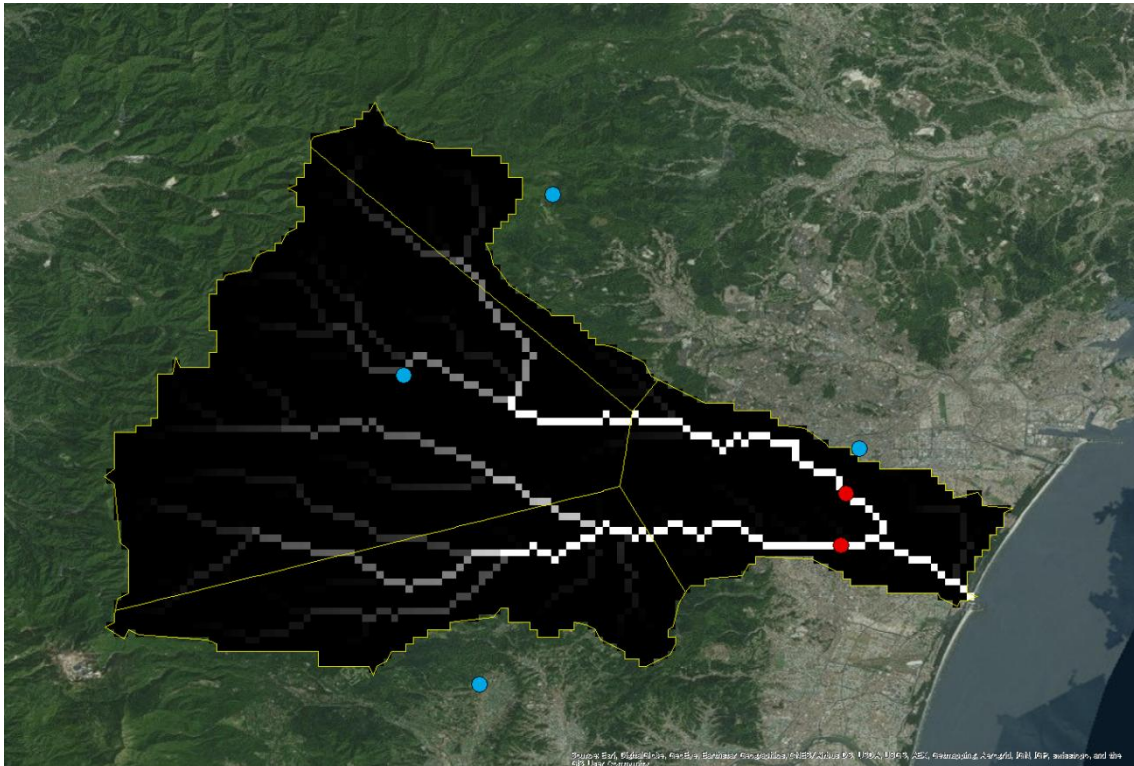


Figure 4.36 Delineated Flow Accumulation data, with position of rainfall stations (blue dots) with belonging Thiessen polygons and observation stations Natoribashi and Hirosebashi (red dots) for the Natori basin

Figure 4.37 shows delineated Digital Elevation Model (DEM) with spatial resolution of 460 m, while Figure 4.38 shows delineated Flow Direction map for the Natori basin.

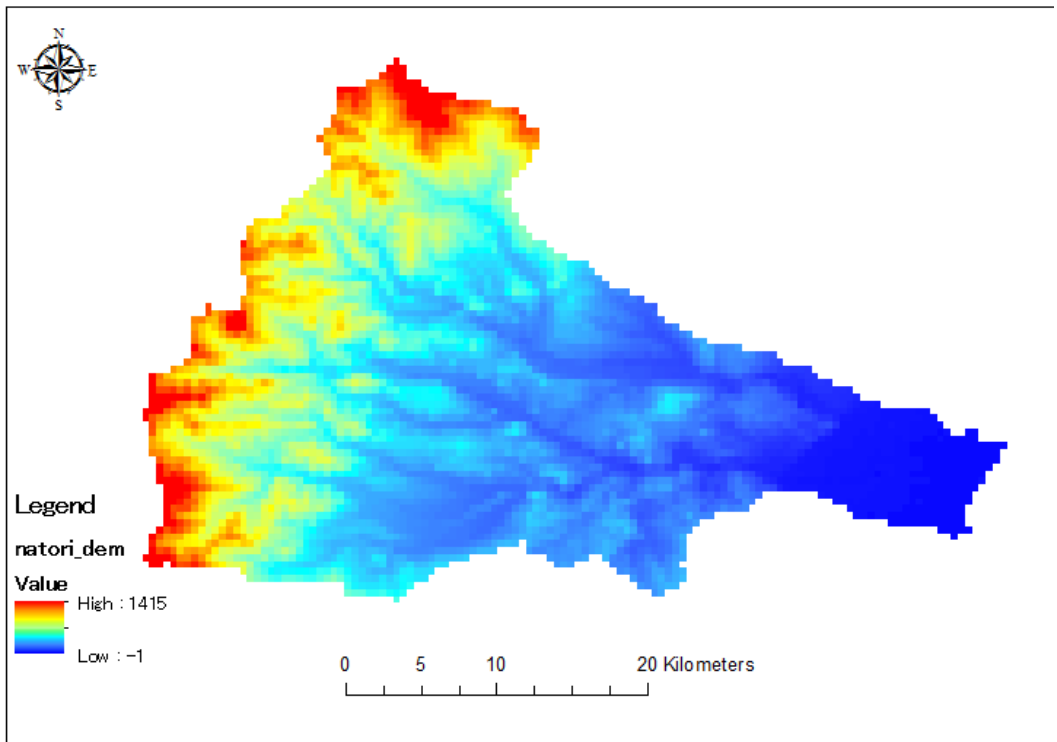


Figure 4.37 Digital Elevation Model (DEM) for the Natori basin (460 m resolution)

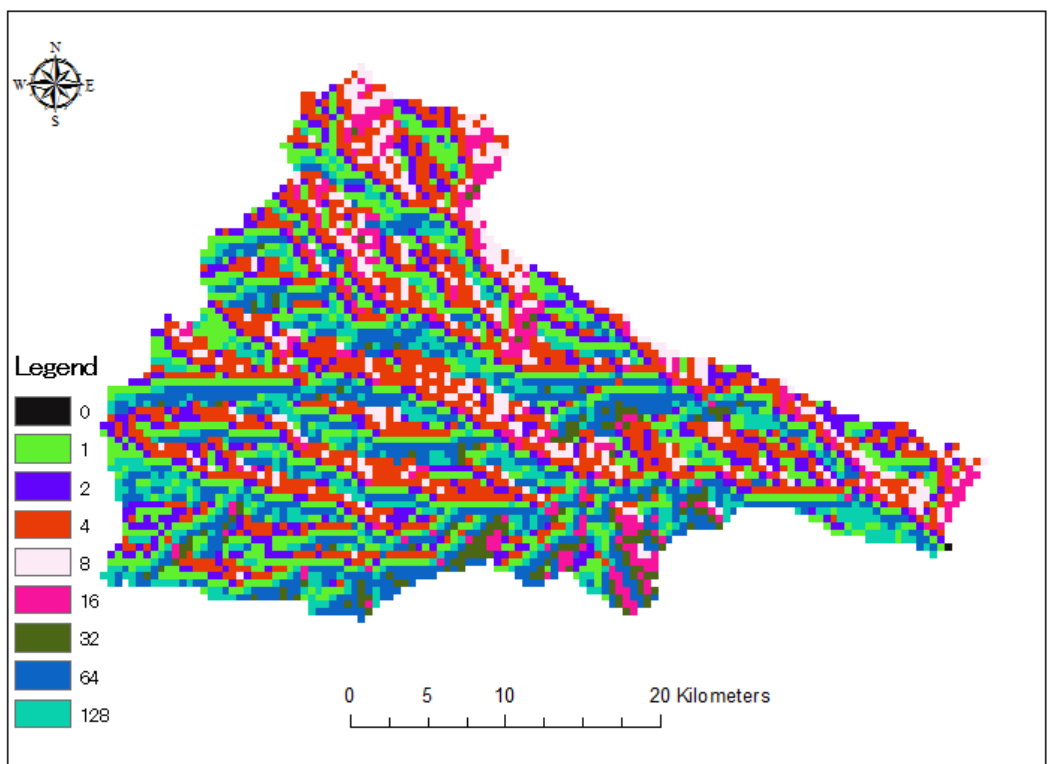


Figure 4.38 Delineated Flow Direction map for the Natori basin

4.6.1.6 Abukuma

Parameters for data from the most downstream discharge station Iwanuma (8.07 km from the river mouth, basin area 5625 km²) were optimized with simulated discharge on the river mouth. Figure 4.39 shows delineated Flow Accumulation data, with position of rainfall stations (blue dots) with belonging Thiessen polygons and observation station Iwanuma (red dot) for the Abukuma basin.

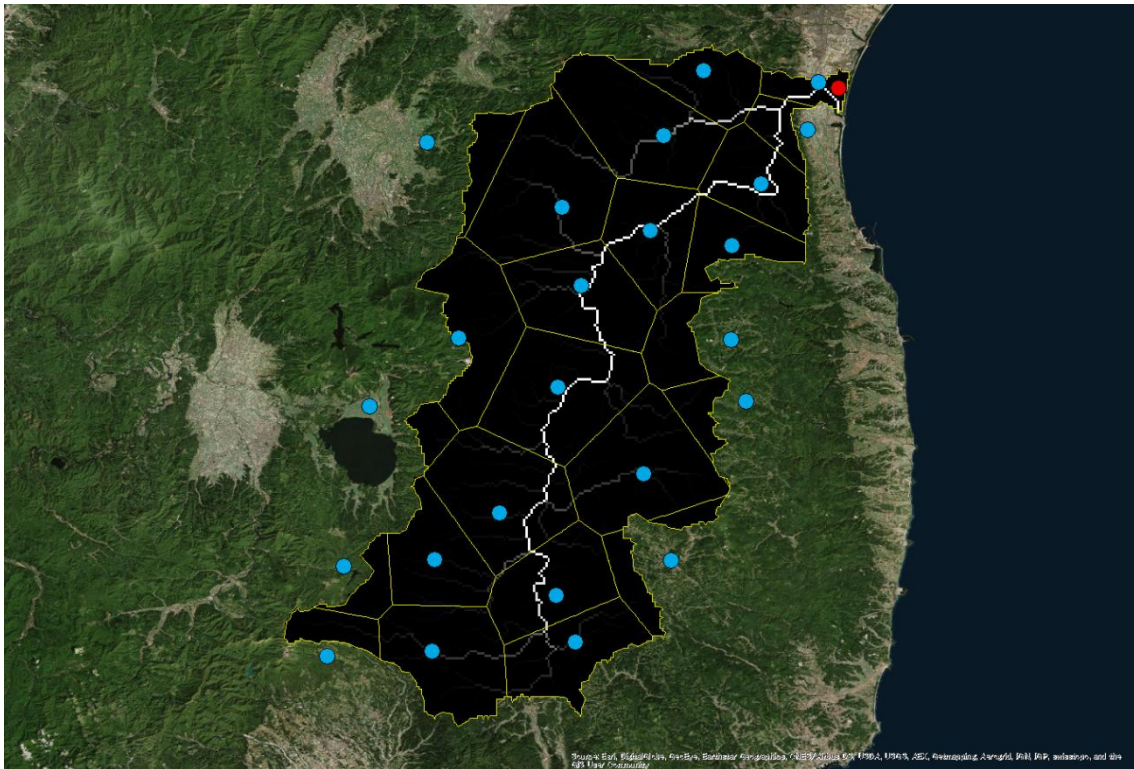


Figure 4.39 Delineated Flow Accumulation data, with position of rainfall stations (blue dots) with belonging Thiessen polygons and observation station Iwanuma (red dot) for the Abukuma basin.

Figure 4.40 shows delineated Digital Elevation Model (DEM) with spatial resolution of 460 m, while Figure 4.41 shows delineated Flow Direction map for the Abukuma basin.

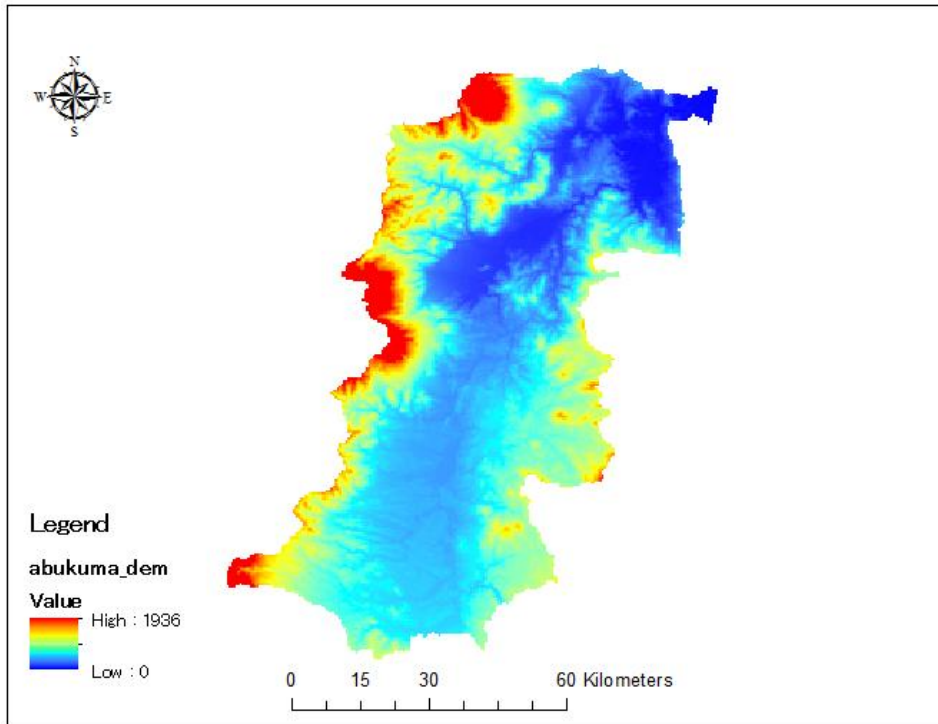


Figure 4.40 Digital Elevation Model (DEM) for the Abukuma basin (460 m resolution)

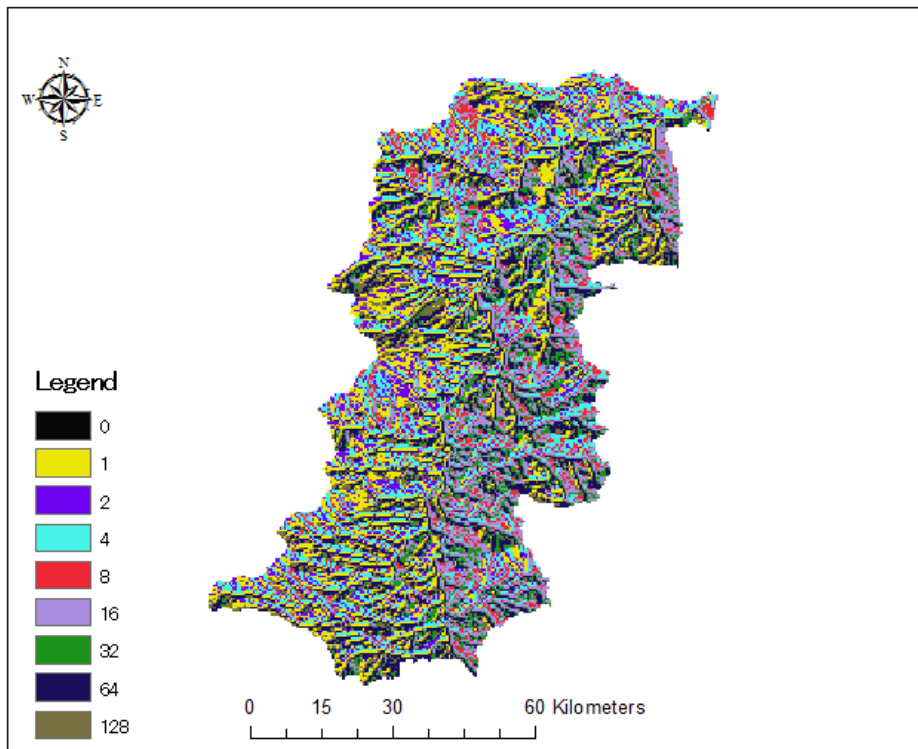


Figure 4.41 Delineated Flow Direction map for the Abukuma basin

4.6.1.7 Kuji

Parameters for data from the most downstream discharge station Sakaki bridge (4.5 km from the river mouth, basin area 1442 km²) were optimized with simulated discharge on the river mouth. Figure 4.42 shows delineated Flow Accumulation data, with position of rainfall stations (blue dots) with belonging Thiessen polygons and observation station Sakaki bridge (red dot) for the Kuji basin.

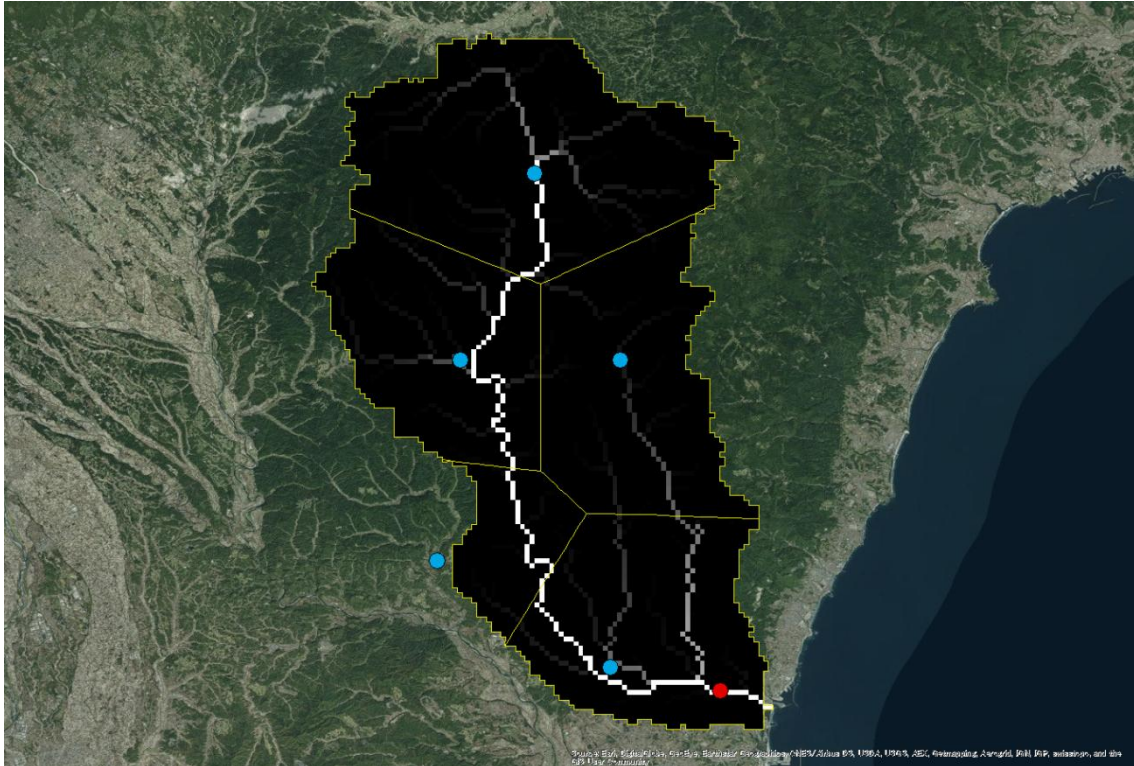


Figure 4.42 Delineated Flow Accumulation data, with position of rainfall stations (blue dots) with belonging Thiessen polygons and observation station Sakaki bridge (red dot) for the Kuji basin.

Figure 4.43 shows delineated Digital Elevation Model (DEM) with spatial resolution of 460 m, while Figure 4.44 shows delineated Flow Direction map for the Kuji basin.

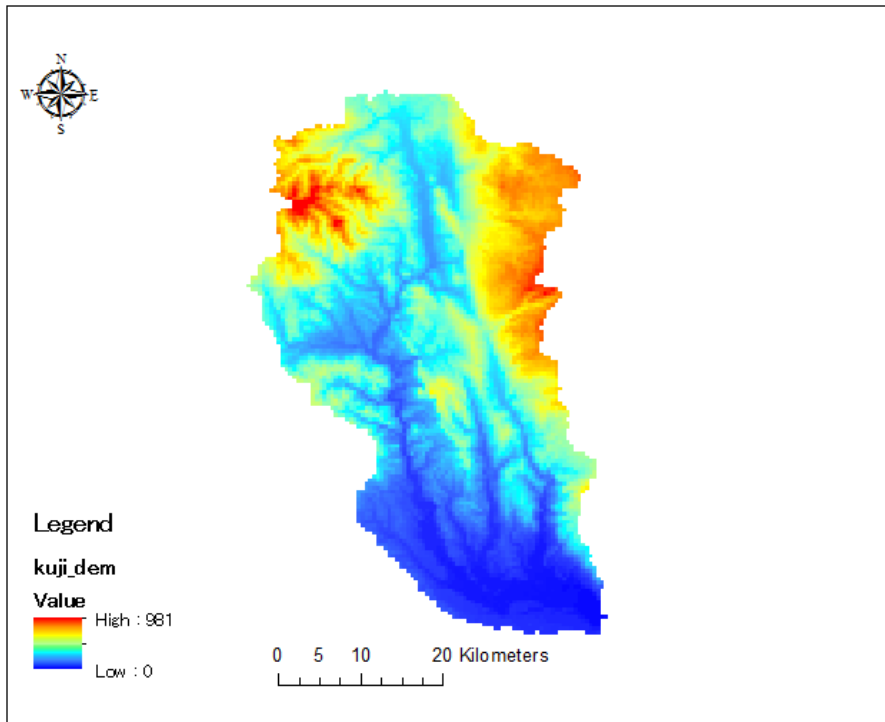


Figure 4.43 Digital Elevation Model (DEM) for the Kuji basin (460 m spatial resolution)

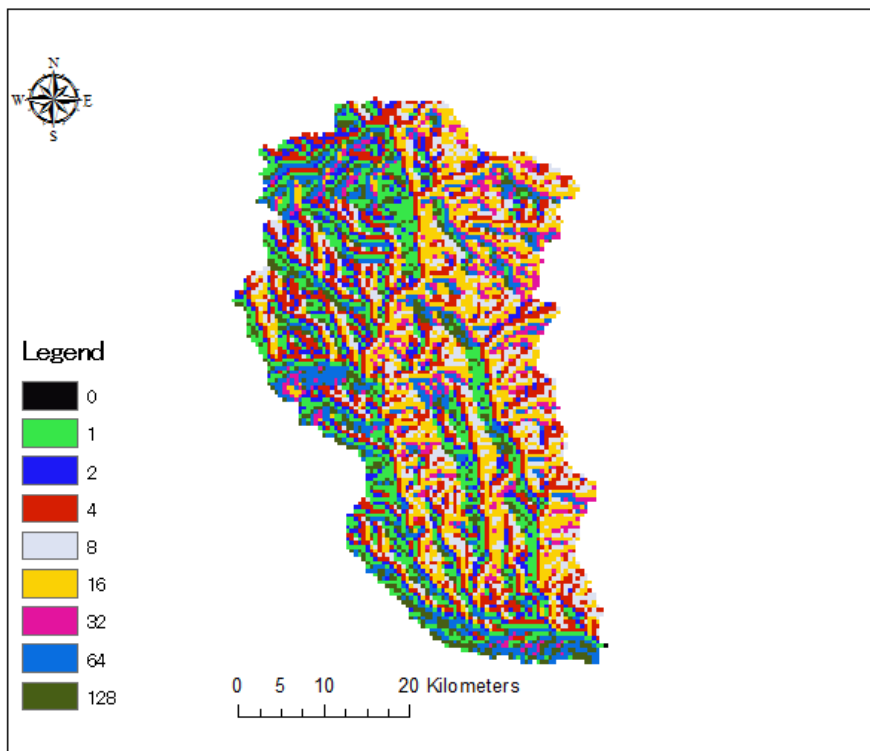


Figure 4.44 Delineated Flow Direction map for the Kuji basin

4.6.1.8 Naka

Parameters for data from the most downstream discharge station Suifu bridge (12.4 km from the river mouth, basin area 2552 km²) were optimized with simulated discharge on the river mouth. Figure 4.45 shows delineated Flow Accumulation data, with position of rainfall stations (blue dots) with belonging Thiessen polygons and observation station Suifu bridge (red dot) for the Naka basin.

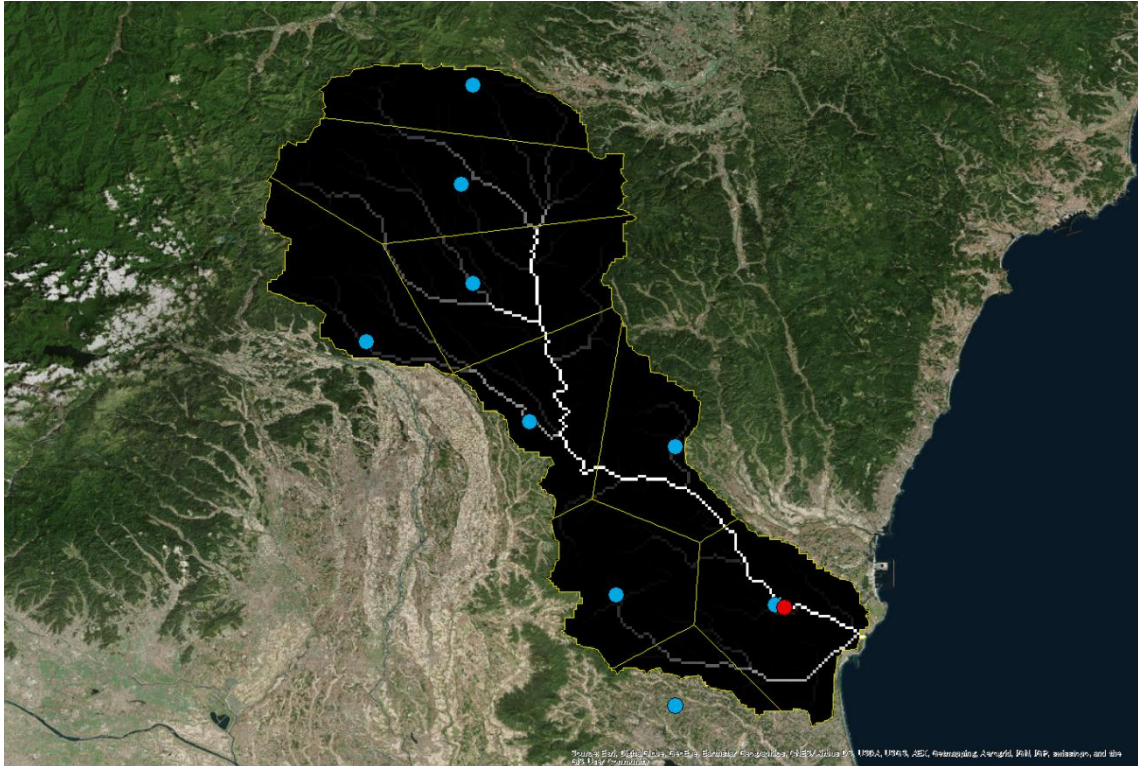


Figure 4.45 Delineated Flow Accumulation data, with position of rainfall stations (blue dots) with belonging Thiessen polygons and observation station Suifu bridge (red dot) for the Naka basin.

Figure 4.46 shows delineated Digital Elevation Model (DEM) with spatial resolution of 460 m, while Figure 4.47 shows delineated Flow Direction map for the Naka basin.

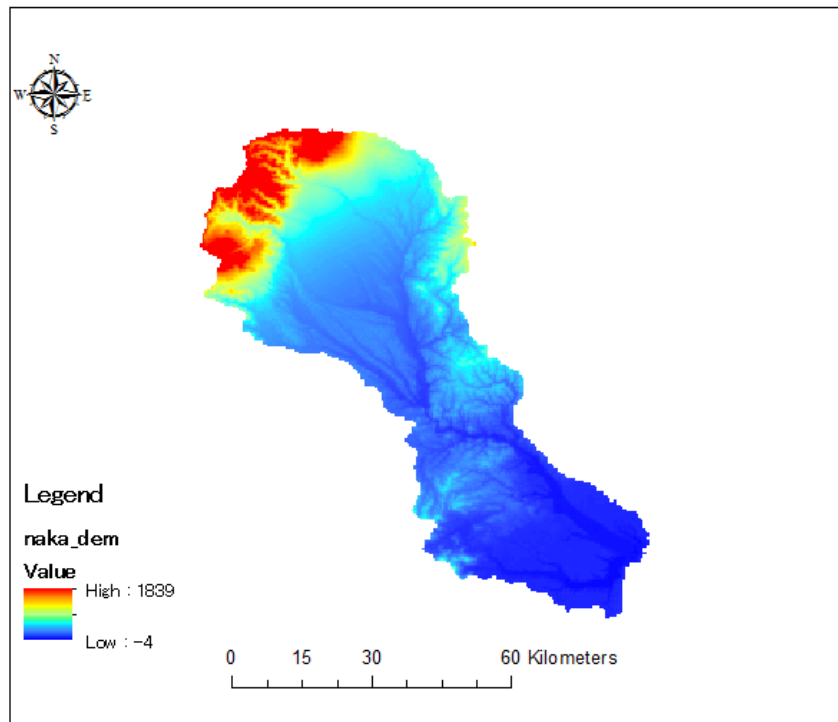


Figure 4.46 Digital Elevation Model (DEM) for the Naka basin (460 m resolution)

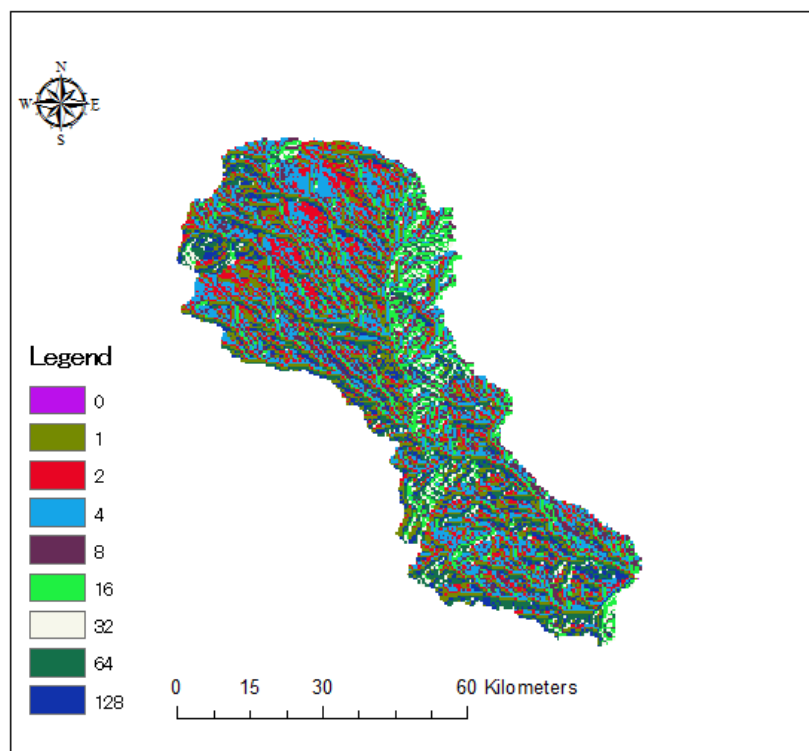


Figure 4.47 Delineated Flow Direction map for the Naka basin

4.6.1.9 Tone

The most downstream discharge station Nunokawa (76.47 km from the river mouth, basin area 12458 km²) is too far from the river mouth so we optimized parameters for data from the cell where is the station instead of from river mouth cell. River mouth discharge may be approximated by multiplying our simulated discharge with basins area ratio, as basin area of river mouth point is 15872 km². Figure 4.48 shows delineated Flow Accumulation data, with position of rainfall stations (blue dots) with belonging Thiessen polygons and observation station Nunokawa (red dot) for the Tone basin.

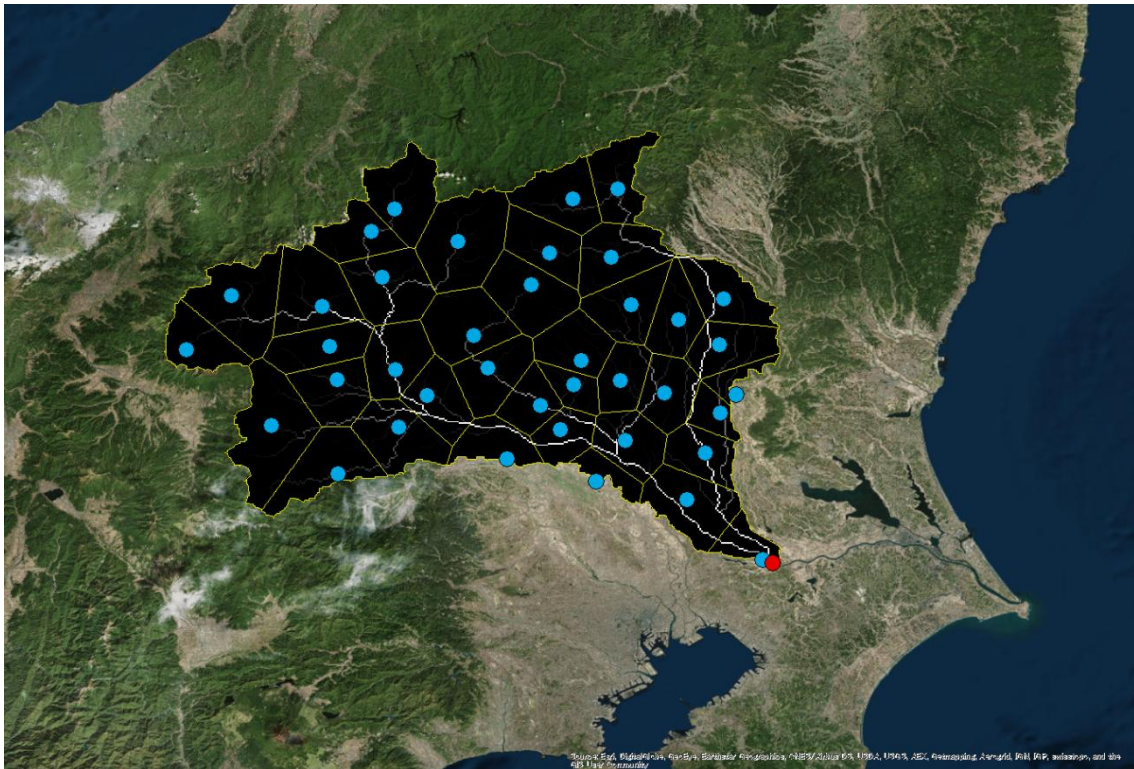


Figure 4.48 Delineated Flow Accumulation data, with position of rainfall stations (blue dots) with belonging Thiessen polygons and observation station Nunokawa (red dot) for the Tone basin.

Figure 4.49 shows delineated Digital Elevation Model (DEM) with spatial resolution of 460 m, while Figure 4.50 shows delineated Flow Direction map for the Tone basin.

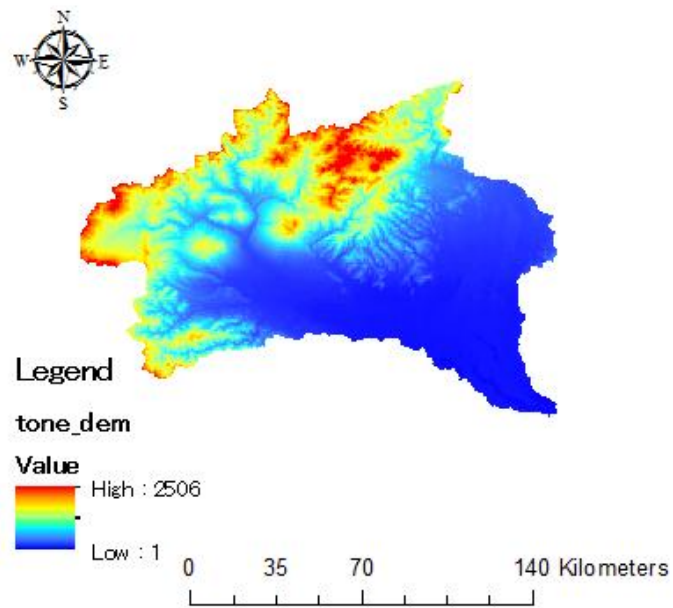


Figure 4.49 Digital Elevation Model (DEM) for the Tone basin (460 m spatial resolution)

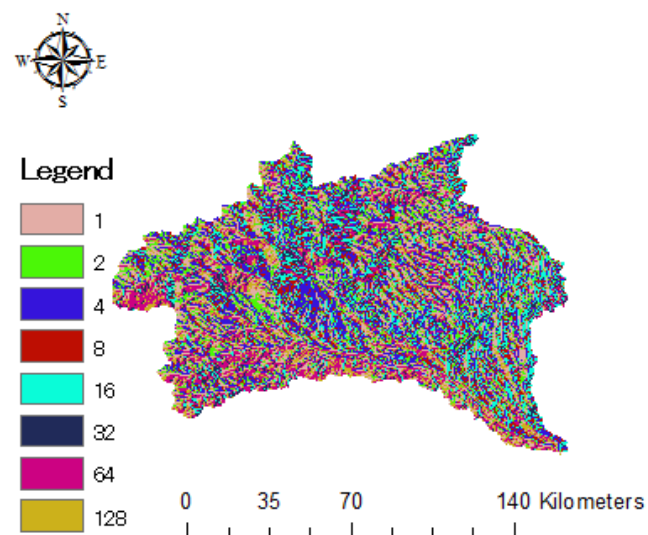


Figure 4.50 Delineated Flow Direction map for the Tone basin

4.7 Results and discussions

4.7.1 Takase

Chataan optimization showed better results ($NS = 0.981$ for calibration and for 0.807 validation). Roke optimization showed $NS = 0.972$ for calibration and 0.691 for validation. Figure 4.51 shows calibrated results for typhoon Chataan and Figure 4.52 shows validated results for typhoon Roke, while Figure 4.53 shows calibrated results for typhoon Roke and Figure 4.54 shows validated results for typhoon Chataan. Table 4.1 shows calibrated parameters of the best optimization for typhoon Chataan, and Table 4.2 for typhoon Roke.

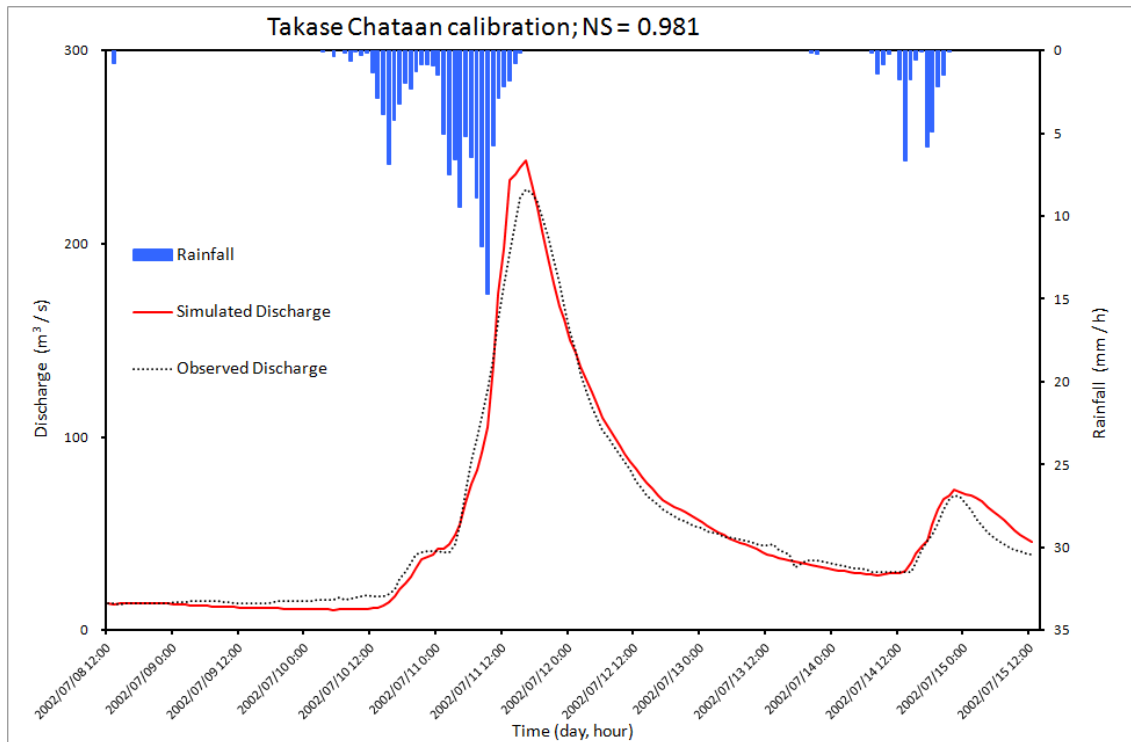


Figure 4.51 Calibrated results for typhoon Chataan (8/07/2002 13:00 - 15/07/2002 12:00)

Table 4.1 Calibrated parameters of the best optimization for typhoon Chataan

Calibrated parameters (Takase)	
N_{slo} [$m^{-1/3}s$]	0.364
N_{riv} [$m^{-1/3}s$]	0.025
ka [ms^{-1}]	0.266
θa	0.484
F1	0.628

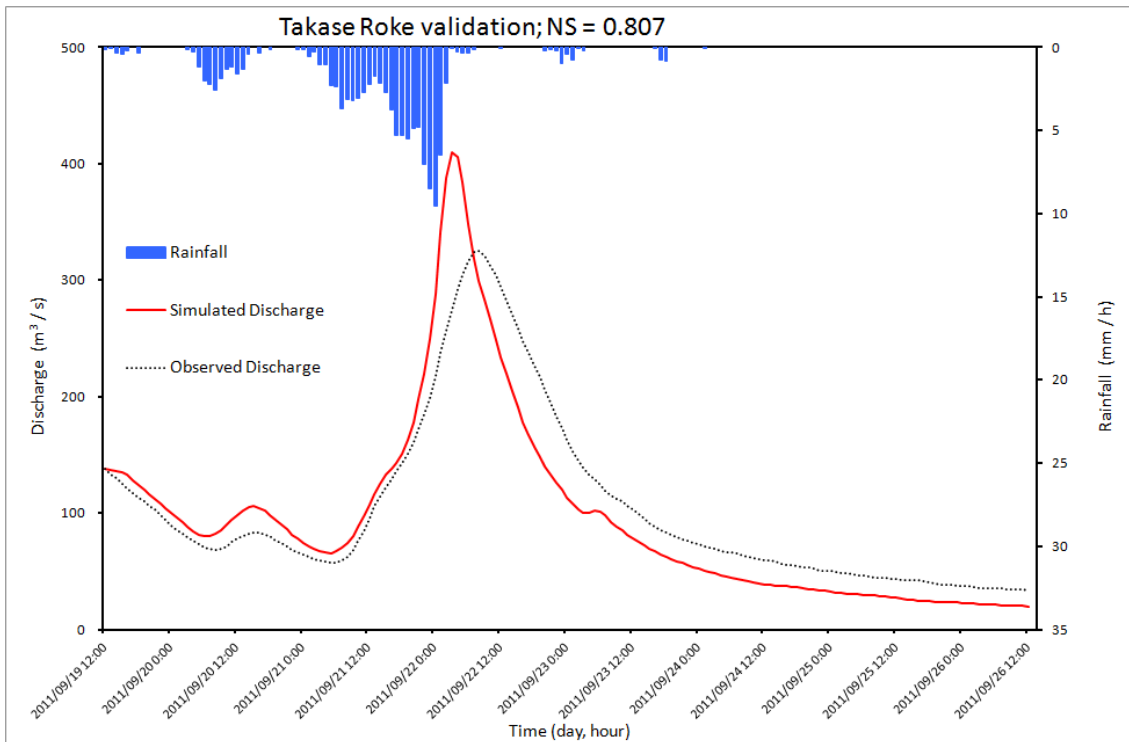


Figure 4.52 Validated results for typhoon Roke (19/09/2011 13:00 - 26/09/2011 12:00)

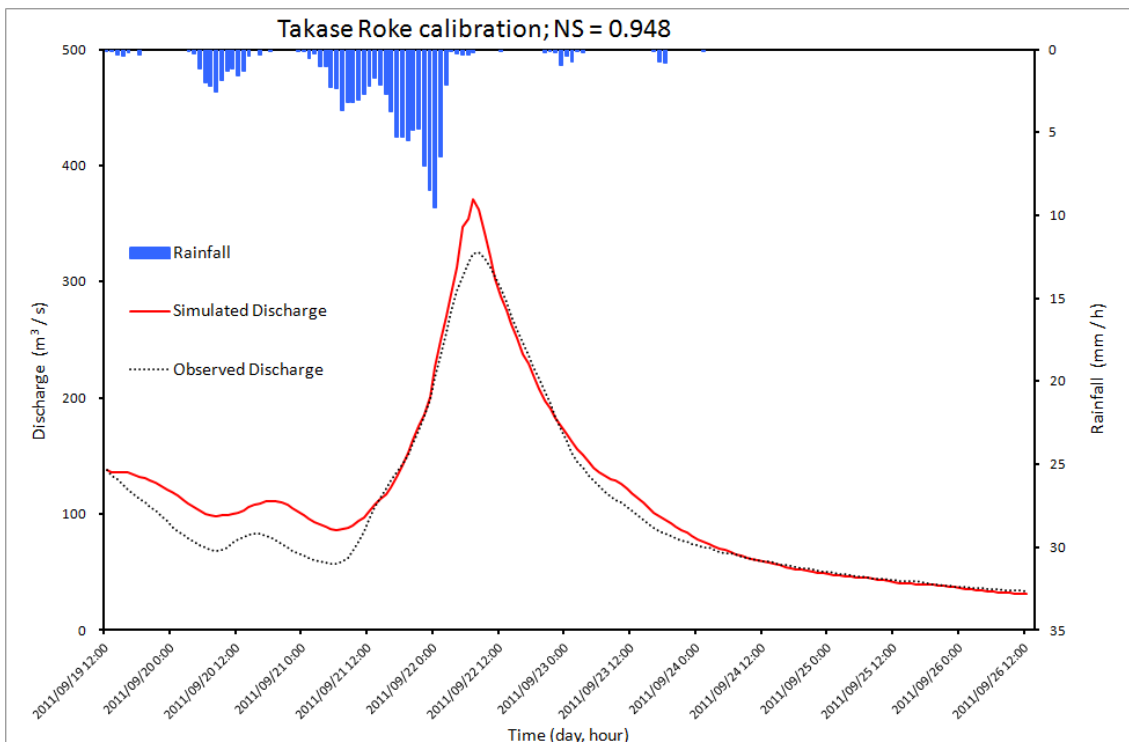


Figure 4.53 Calibrated results for typhoon Roke (19/09/2011 13:00 - 26/09/2011 12:00)

Table 4.2 Calibrated parameters of the best optimization for typhoon Roke

Optimized parameters:	
N_slo [$m^{-1/3}s$]	0.563
N_riv [$m^{-1/3}s$]	0.070
ka [ms^{-1}]	0.432
θ_a	0.454
F1	0.719

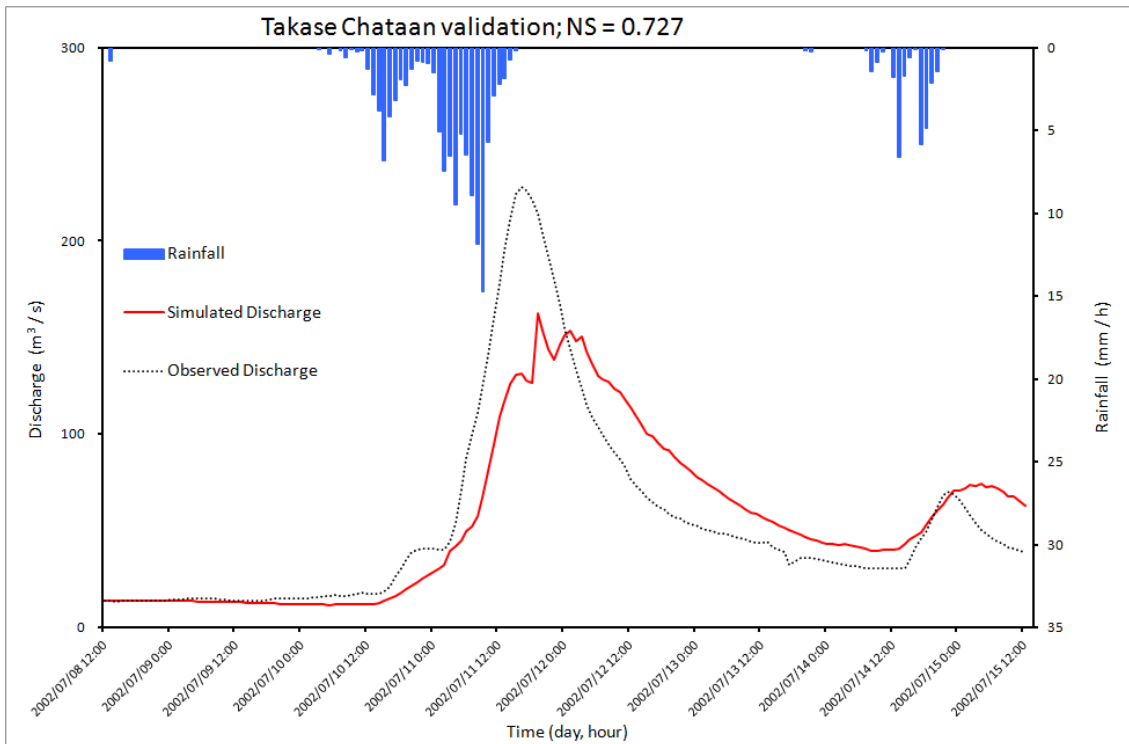


Figure 4.54 Validated results for typhoon Chataan (8/07/2002 13:00 - 15/07/2002 12:00)

4.7.2 Mabechi

Chataan optimization showed better results ($NS = 0.897$ for calibration and for 0.742 validation). Roke optimization showed $NS = 0.978$ for calibration and 0.113 for validation. Figure 4.55 shows calibrated results for typhoon Chataan and Figure 4.56 shows validated results for typhoon Roke, while Figure 4.57 shows calibrated results for typhoon Roke and Figure 4.58 shows validated results for typhoon Chataan. Table 4.3 shows calibrated parameters of the best optimization for typhoon Chataan, and Table 4.4 for typhoon Roke.

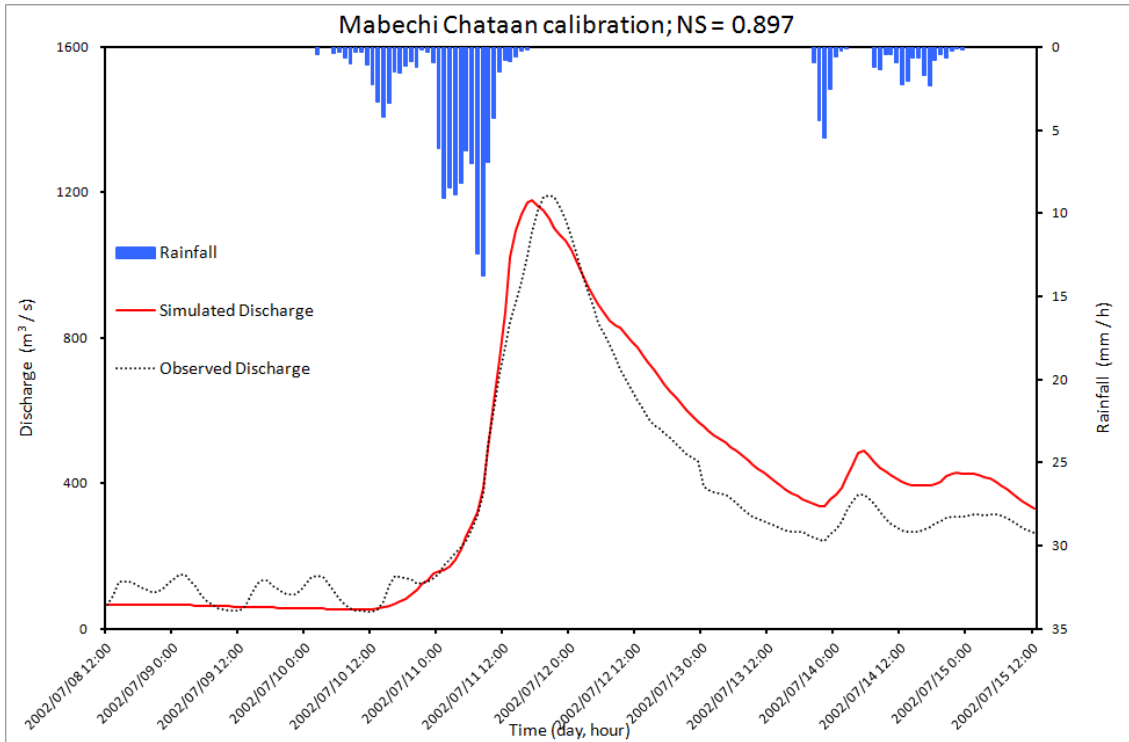


Figure 4.55 Calibrated results for typhoon Chataan (8/07/2002 13:00 - 15/07/2002 12:00)

Table 4.3 Calibrated parameters of the best optimization for typhoon Chataan

Optimized parameters:	
N_slo [$m^{-1/3}s$]	0.105
N_riv [$m^{-1/3}s$]	0.030
ka [ms^{-1}]	0.469
θ_a	0.400
F1	0.600

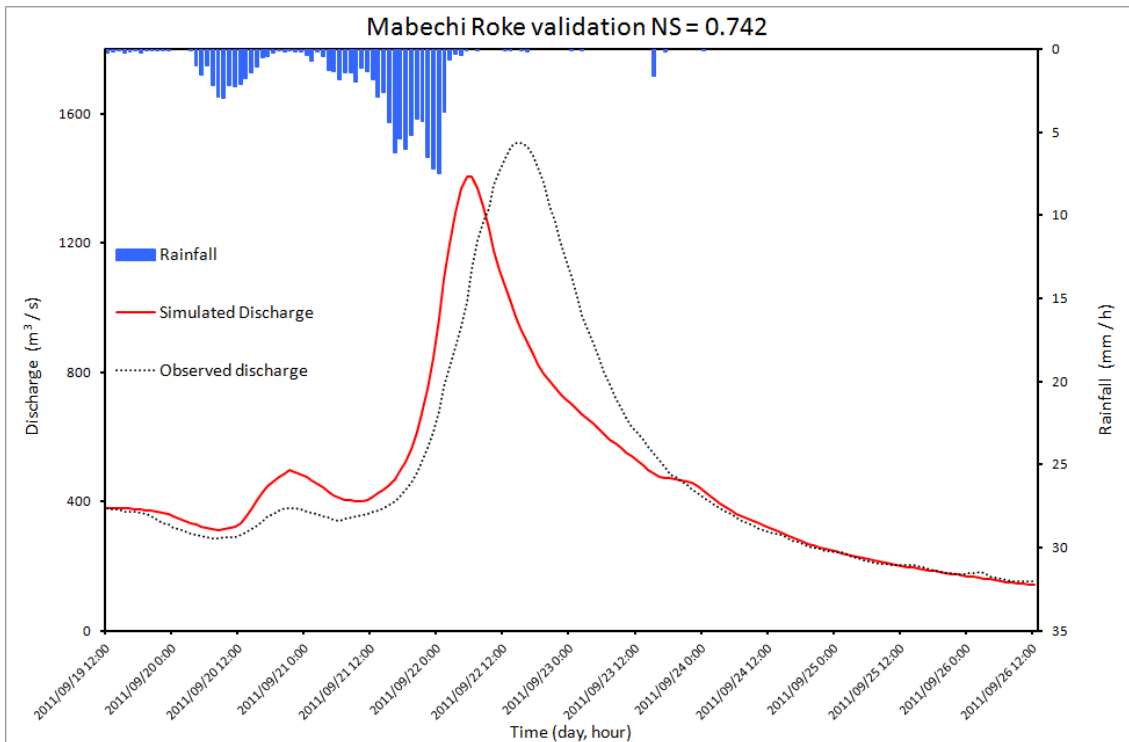


Figure 4.56 Validated results for typhoon Roke (19/09/2011 13:00 - 26/09/2011 12:00)

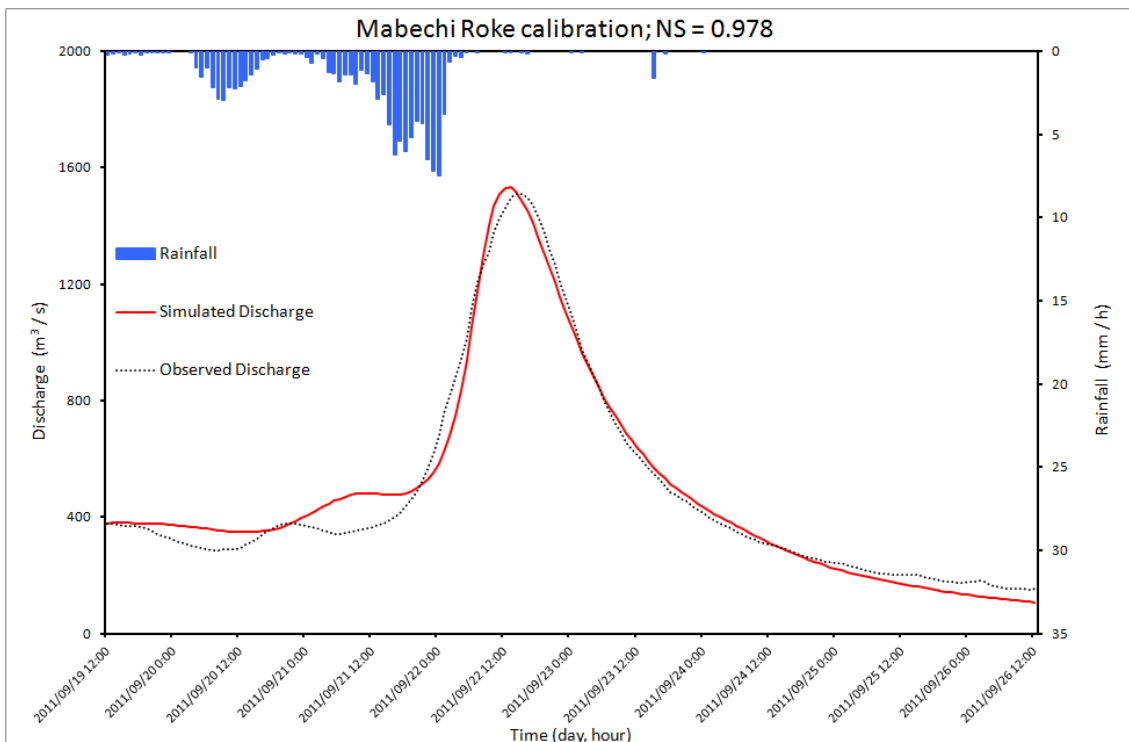


Figure 4.57 Calibrated results for typhoon Roke (19/09/2011 13:00 - 26/09/2011 12:00)

Table 4.4 Calibrated parameters of the best optimization for typhoon Roke

Optimized parameters:	
N_slo [$m^{-1/3}s$]	0.688
N_riv [$m^{-1/3}s$]	0.100
ka [ms^{-1}]	0.161
θ_a	0.279
F1	0.620

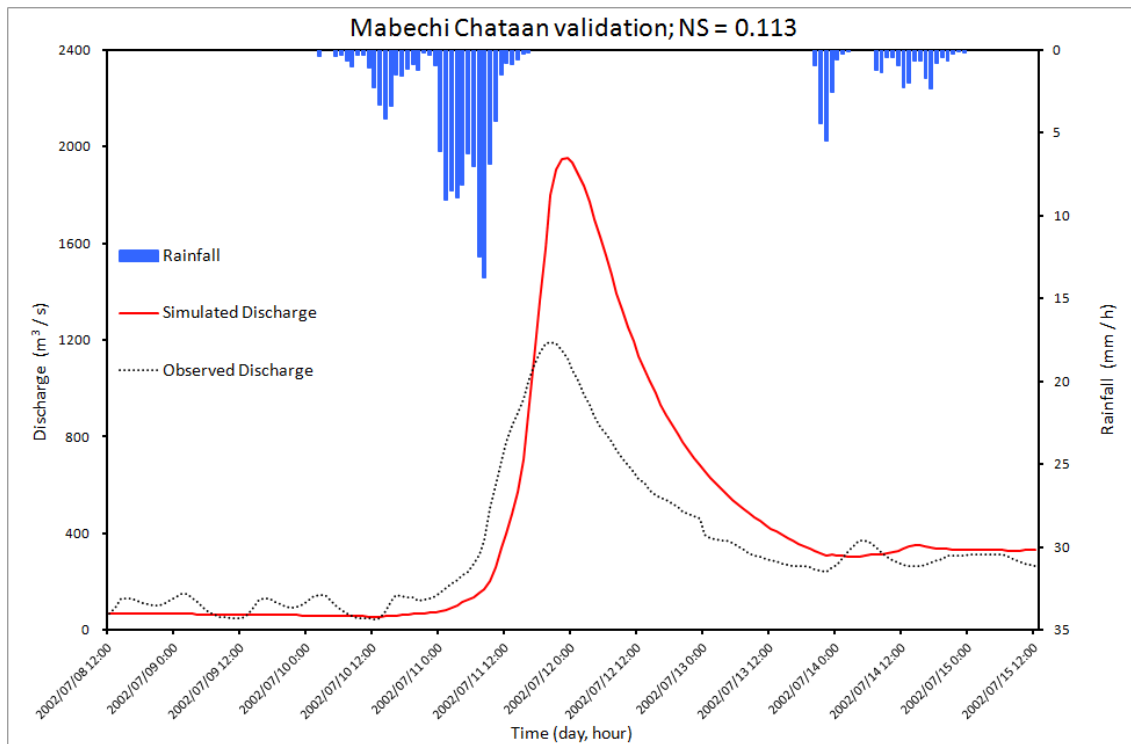


Figure 4.58 Validated results for typhoon Chataan (8/07/2002 13:00 - 15/07/2002 12:00)

4.7.3 Kitakami

Roke optimization showed better results ($NS = 0.966$ for calibration and for 0.819 validation). Chataan optimization showed $NS = 0.913$ for calibration and 0.752 for validation. Figure 4.59 shows calibrated results for typhoon Roke and Figure 4.60 shows validated results for typhoon Chataan, while Figure 4.61 shows calibrated results for typhoon Chataan and Figure 4.62 shows validated results for typhoon Roke. Table 4.5 shows calibrated parameters of the best optimization for typhoon Roke, and Table 4.6 for typhoon Chataan.

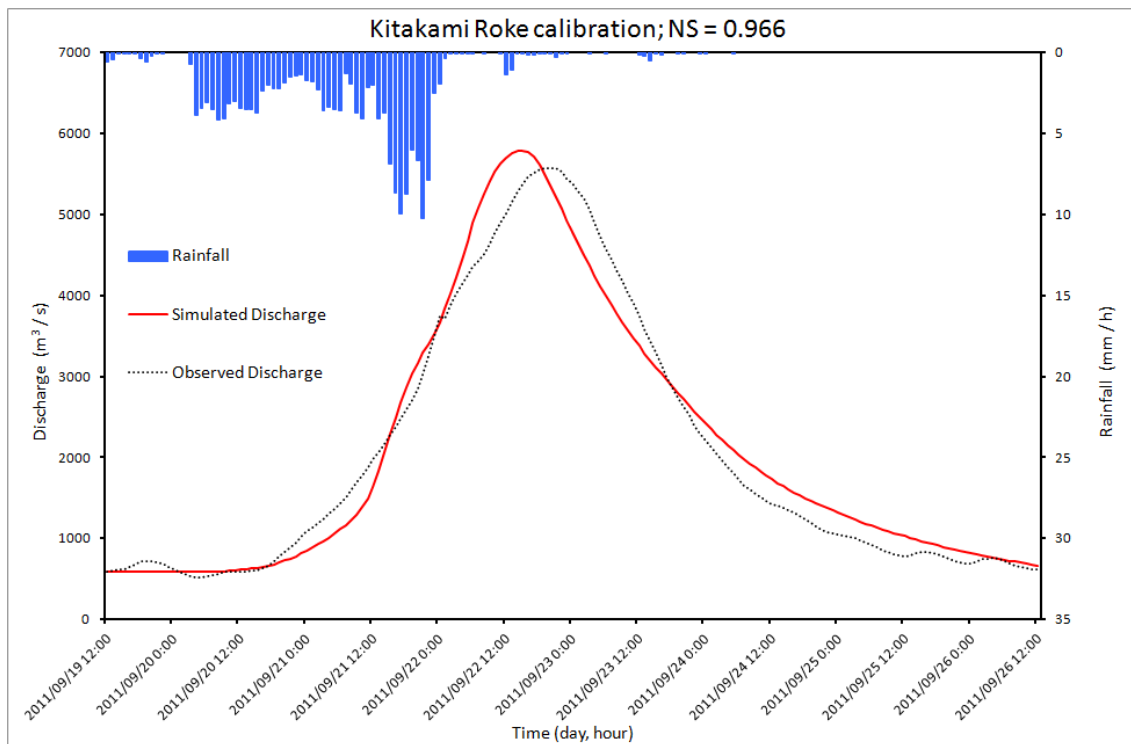


Figure 4.59 Calibrated results for typhoon Roke (19/09/2011 13:00 - 26/09/2011 12:00)

Table 4.5 Calibrated parameters of the best optimization for typhoon Roke

Optimized parameters:	
N_slo [$m^{-1/3}s$]	1.000
N_riv [$m^{-1/3}s$]	0.100
ka [ms^{-1}]	0.135
θ_a	0.287
F1	0.600

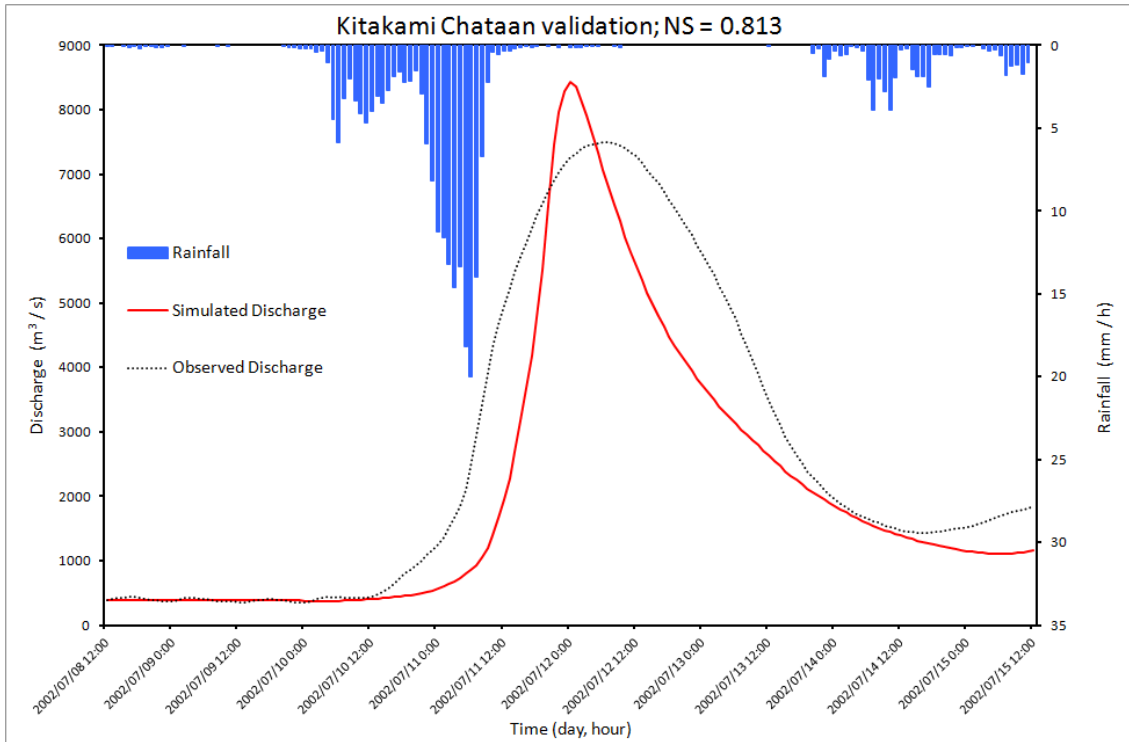


Figure 4.60 Validated results for typhoon Chataan (8/07/2002 13:00 - 15/07/2002 12:00)

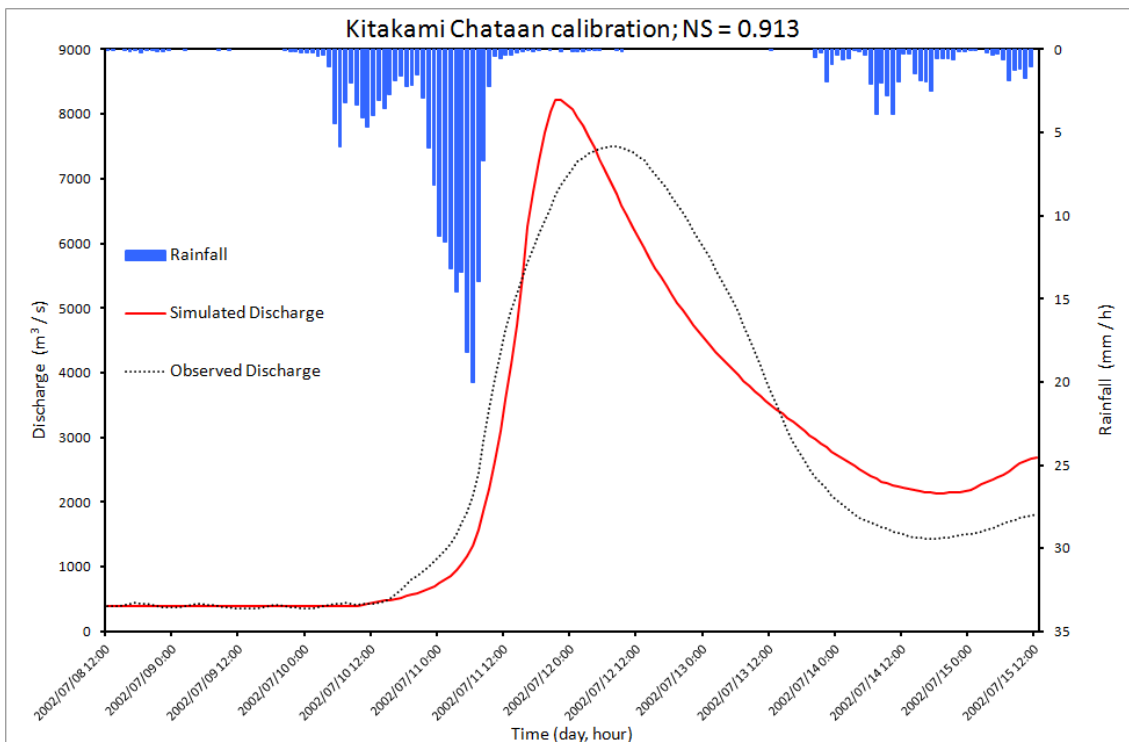


Figure 4.61 Calibrated results for typhoon Chataan (8/07/2002 13:00 - 15/07/2002 12:00)

Table 4.6 Calibrated parameters of the best optimization for typhoon Chataan

Optimized parameters:	
N_slo [$m^{-1/3}s$]	1.000
N_riv [$m^{-1/3}s$]	0.076
ka [ms^{-1}]	0.203
θa	0.098
F1	0.856

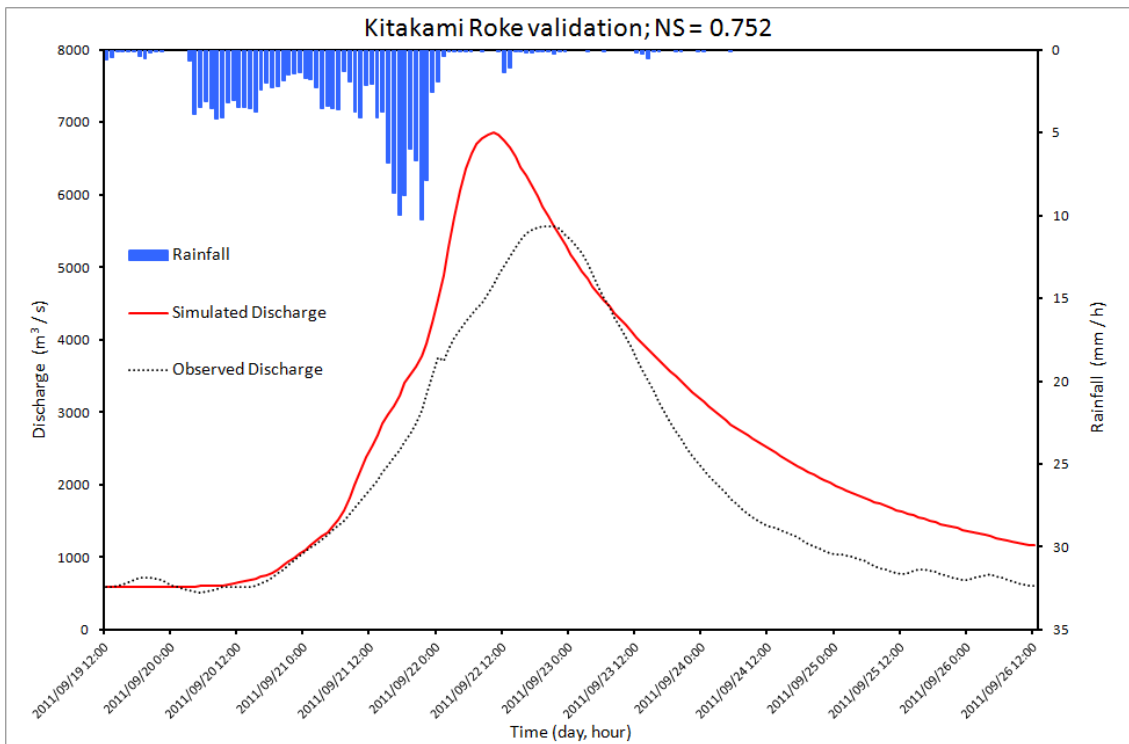


Figure 4.62 Validated results for typhoon Roke (19/09/2011 13:00 - 26/09/2011 12:00)

4.7.4 Naruse

Roke optimization showed better results ($NS = 0.957$ for calibration and for 0.808 validation). Chataan optimization showed $NS = 0.987$ for calibration and 0.662 for validation. Figure 4.63 shows calibrated results for typhoon Roke and Figure 4.64 shows validated results for typhoon Chataan, while Figure 4.65 shows calibrated results for typhoon Chataan and Figure 4.66 shows validated results for typhoon Roke. Table 4.7 shows calibrated parameters of the best optimization for typhoon Roke, and Table 4.8 for typhoon Chataan.

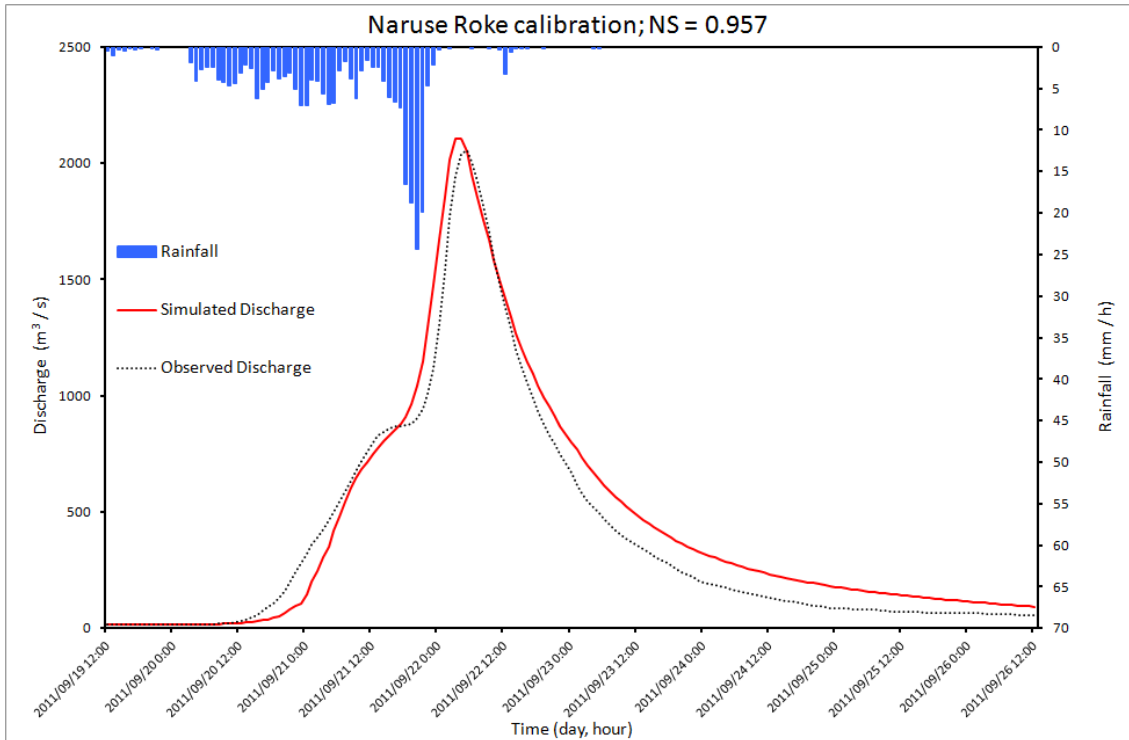


Figure 4.63 Calibrated results for typhoon Roke (19/09/2011 13:00 - 26/09/2011 12:00)

Table 4.7 Calibrated parameters of the best optimization for typhoon Roke

Optimized parameters:	
N_slo [$m^{-1/3}s$]	1.000
N_riv [$m^{-1/3}s$]	0.045
ka [ms^{-1}]	0.166
θ_a	0.305
F1	0.600

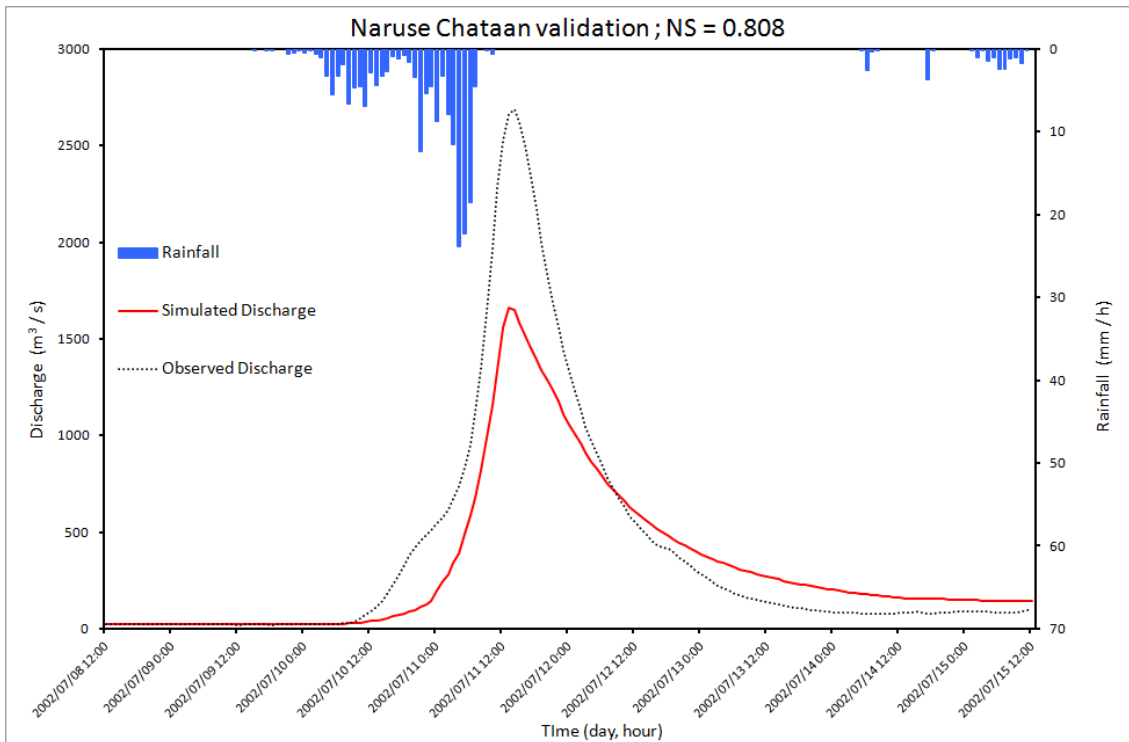


Figure 4.64 Validated results for typhoon Chataan (8/07/2002 13:00 - 15/07/2002 12:00)

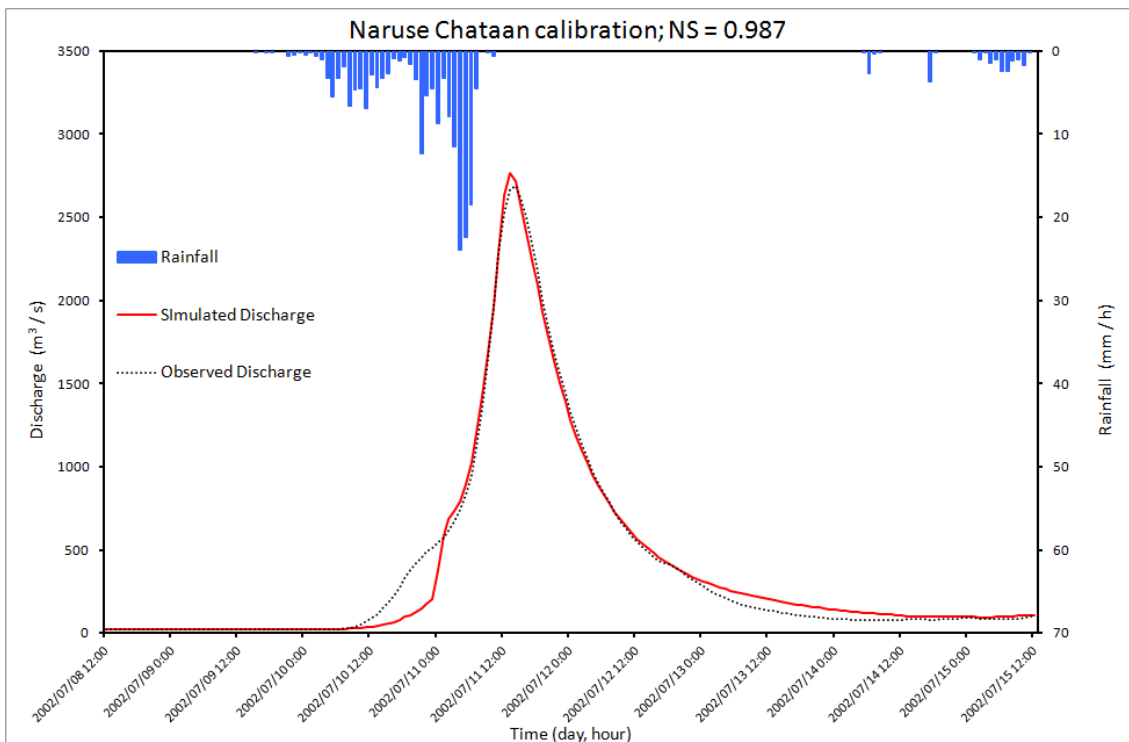


Figure 4.65 Calibrated results for typhoon Chataan (8/07/2002 13:00 - 15/07/2002 12:00)

Table 4.8 Calibrated parameters of the best optimization for typhoon Chataan

Optimized parameters:	
N_slo [$m^{-1/3}s$]	1.000
N_riv [$m^{-1/3}s$]	0.056
ka [ms^{-1}]	0.100
θ_a	0.476
F1	0.676

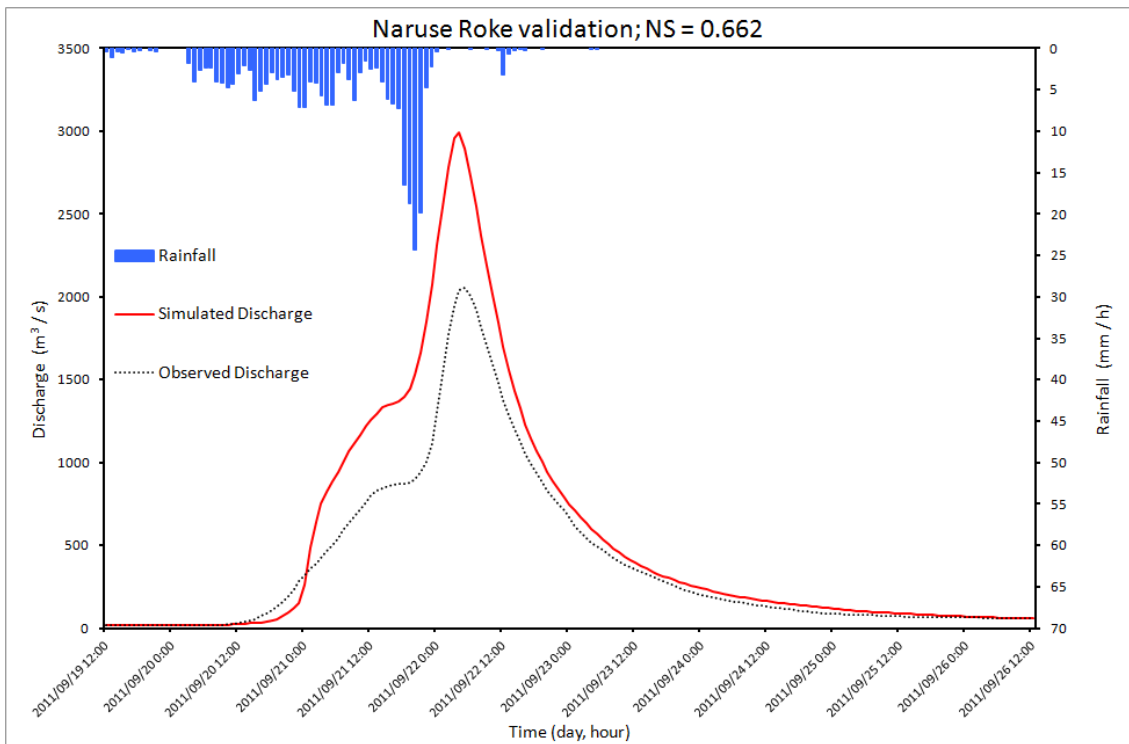


Figure 4.66 Validated results for typhoon Roke (19/09/2011 13:00 - 26/09/2011 12:00)

4.7.5 Natori

Roke optimization showed better results ($NS = 0.974$ for calibration and for 0.970 validation). Chataan optimization showed $NS = 0.986$ for calibration and 0.922 for validation. Figure 4.67 shows calibrated results for typhoon Roke and Figure 4.68 shows validated results for typhoon Chataan, while Figure 4.69 shows calibrated results for typhoon Chataan and Figure 4.70 shows validated results for typhoon Roke. Table 4.9 shows calibrated parameters of the best optimization for typhoon Roke, and Table 4.10 for typhoon Chataan.

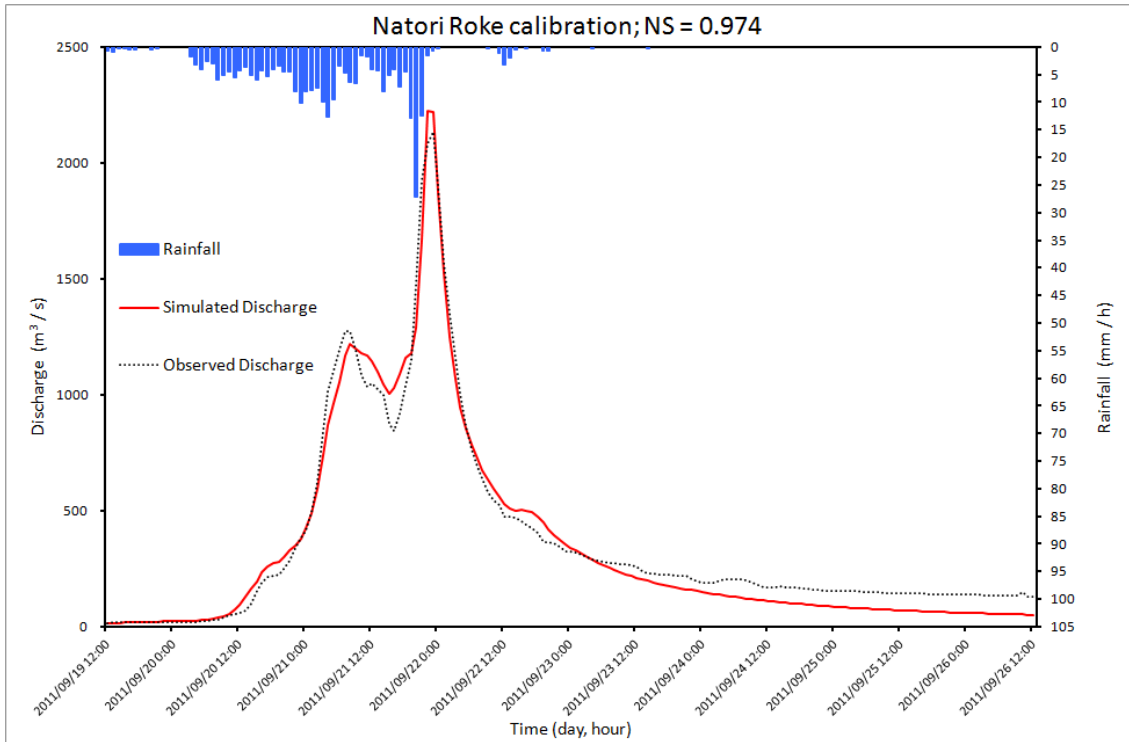


Figure 4.67 Calibrated results for typhoon Roke (19/09/2011 13:00 - 26/09/2011 12:00)

Table 4.9 Calibrated parameters of the best optimization for typhoon Roke

Optimized parameters:	
N_slo [$m^{-1/3}s$]	0.196
N_riv [$m^{-1/3}s$]	0.018
ka [ms^{-1}]	0.152
θ_a	0.102
F1	0.779

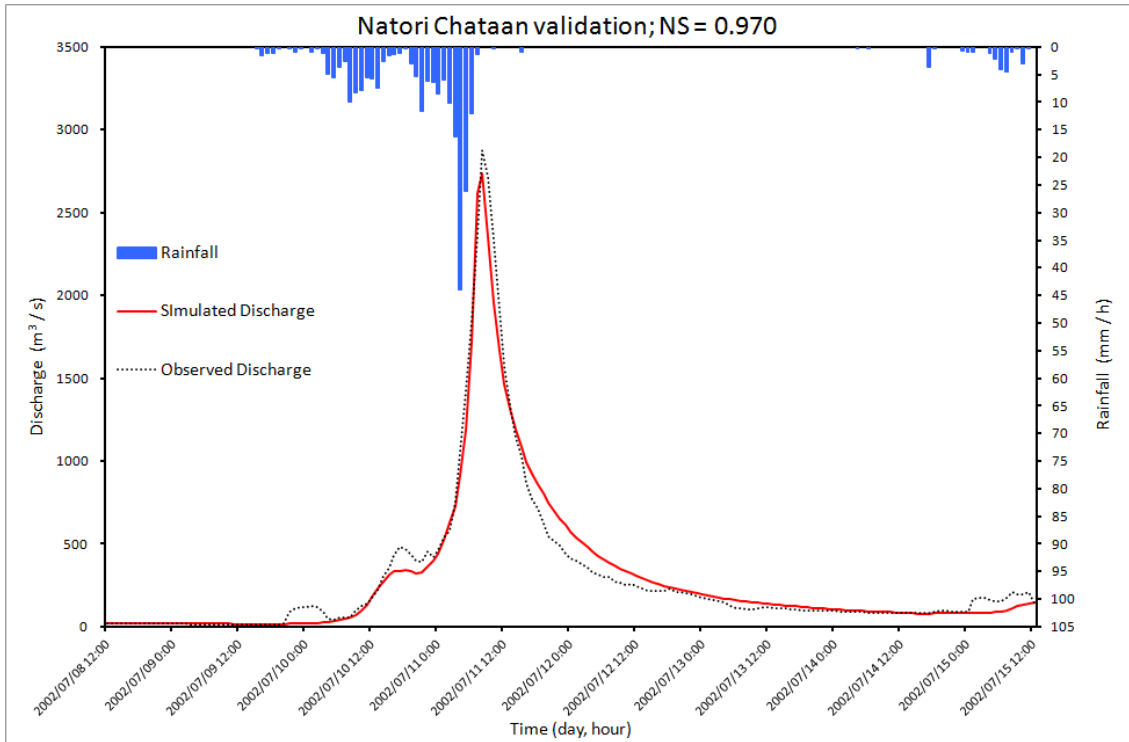


Figure 4.68 Validated results for typhoon Chataan (8/07/2002 13:00 - 15/07/2002 12:00)

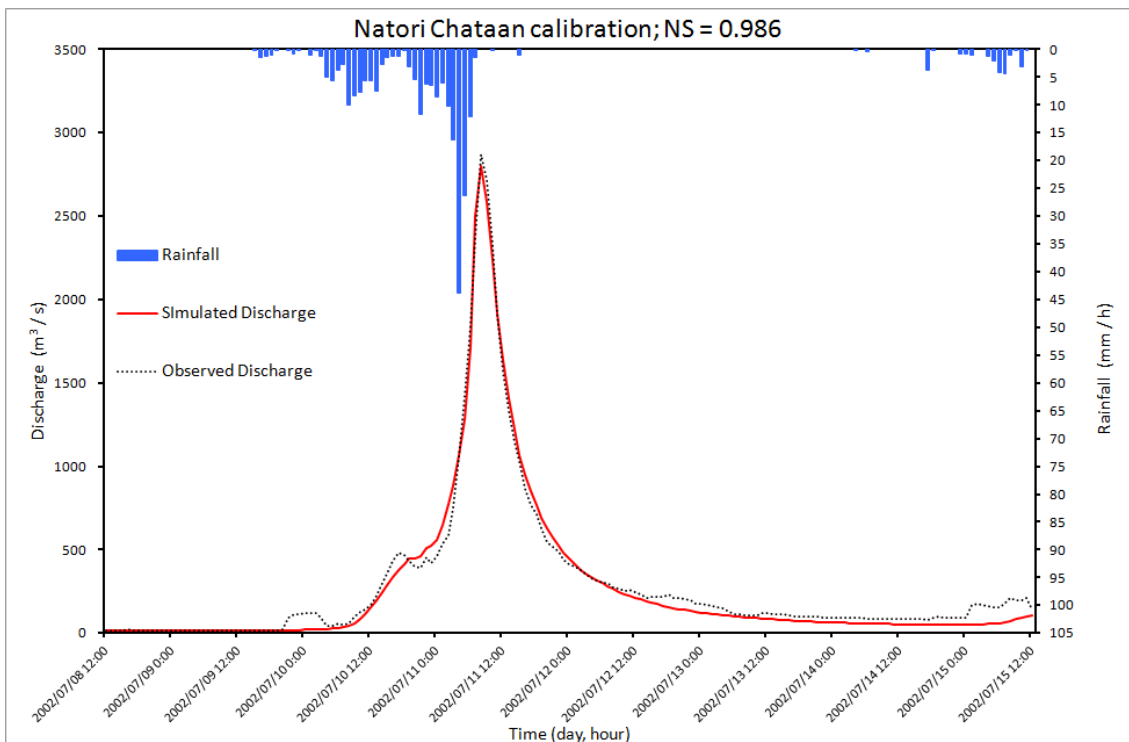


Figure 4.69 Calibrated results for typhoon Chataan (8/07/2002 13:00 - 15/07/2002 12:00)

Table 4.10 Calibrated parameters of the best optimization for typhoon Chataan

Optimized parameters:	
N_slo [$m^{-1/3}s$]	0.100
N_riv [$m^{-1/3}s$]	0.019
ka [ms^{-1}]	0.231
θ_a	0.499
F1	0.704

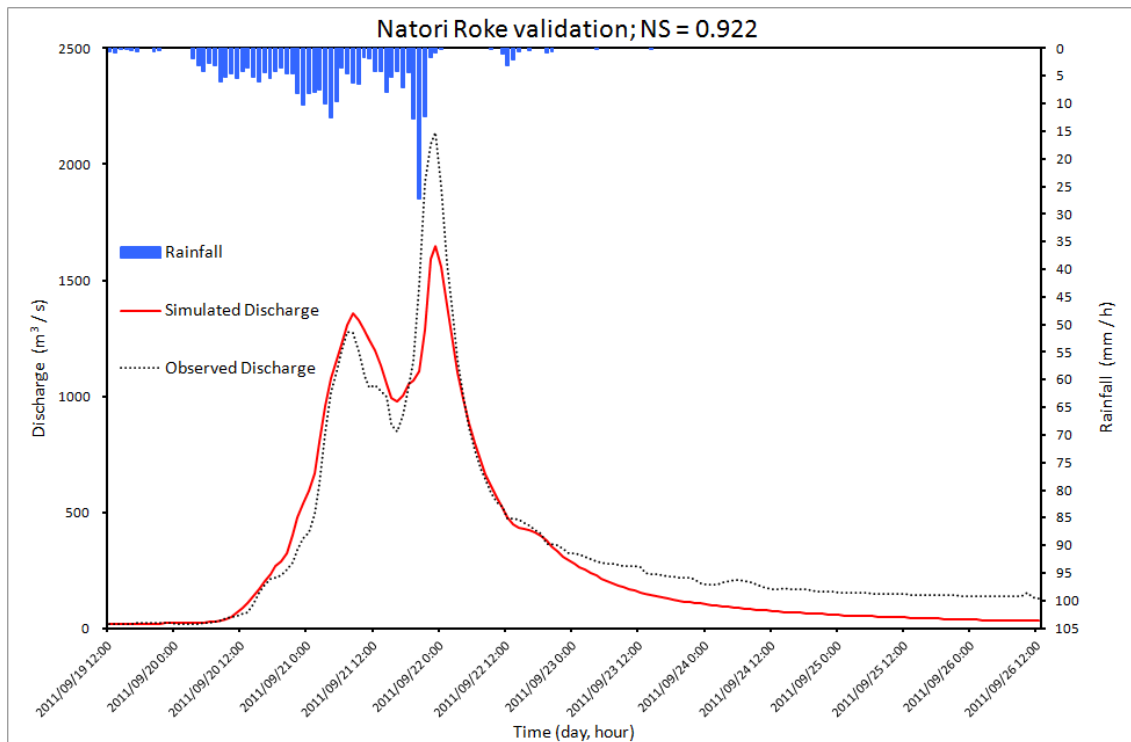


Figure 4.70 Validated results for typhoon Roke (19/09/2011 13:00 - 26/09/2011 12:00)

4.7.6 Abukuma

Roke optimization showed better results ($NS = 0.916$ for calibration and for 0.710 validation). Chataan optimization showed $NS = 0.957$ for calibration and 0.581 for validation. Figure 4.71 shows calibrated results for typhoon Roke and Figure 4.72 shows validated results for typhoon Chataan, while Figure 4.73 shows calibrated results for typhoon Chataan and Figure 4.74 shows validated results for typhoon Roke. Table 4.11 shows calibrated parameters of the best optimization for typhoon Roke, and Table 4.12 for typhoon Chataan.

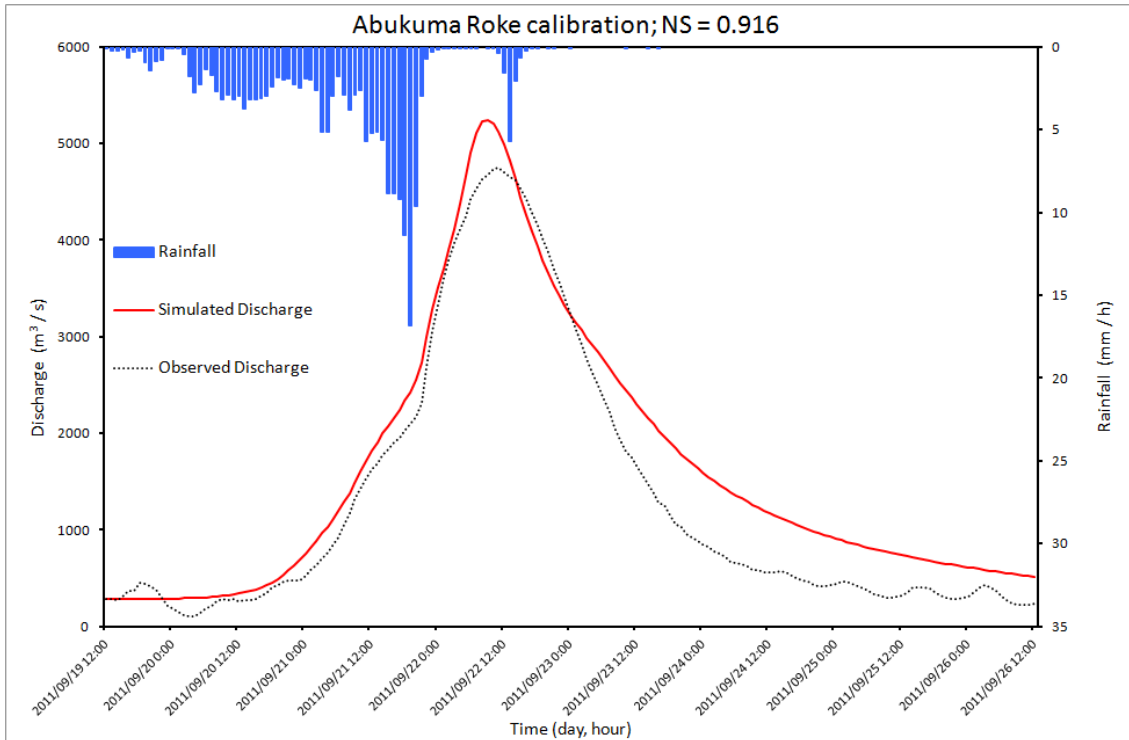


Figure 4.71 Calibrated results for typhoon Roke (19/09/2011 13:00 - 26/09/2011 12:00)

Table 4.11 Calibrated parameters of the best optimization for typhoon Roke

Optimized parameters:	
N_slo [$m^{-1/3}s$]	0.505
N_riv [$m^{-1/3}s$]	0.079
ka [ms^{-1}]	0.137
θ_a	0.109
F1	0.600

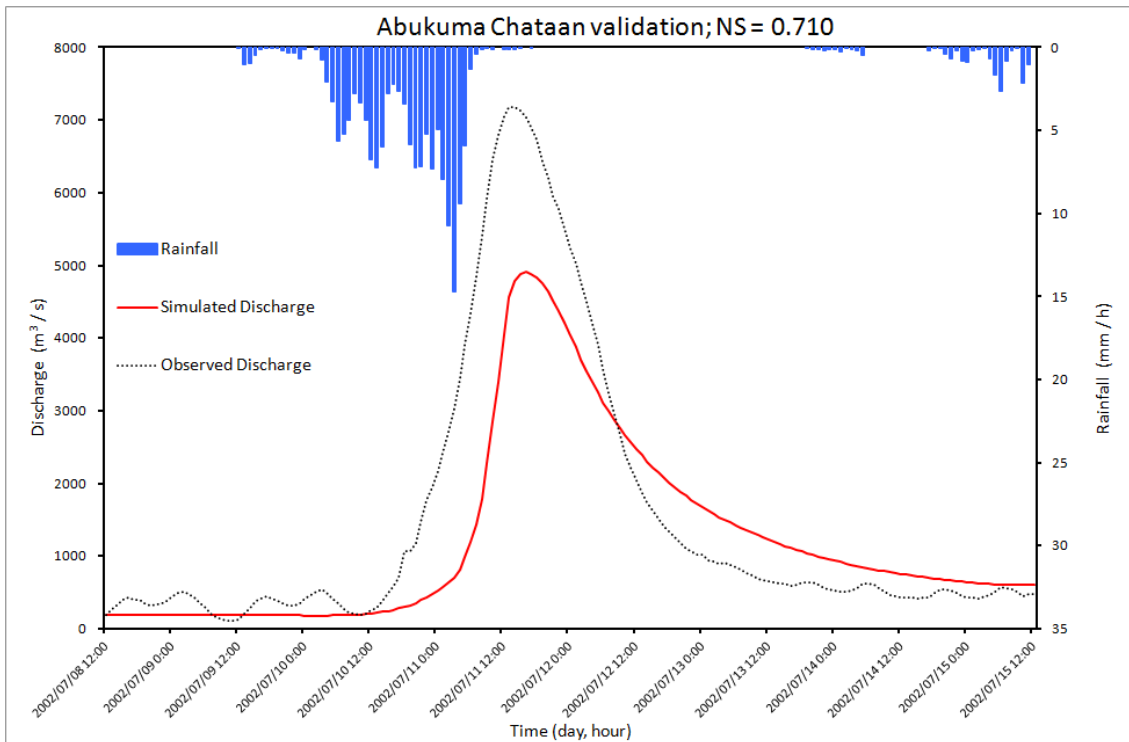


Figure 4.72 Validated results for typhoon Chataa (8/07/2002 13:00 - 15/07/2002 12:00)

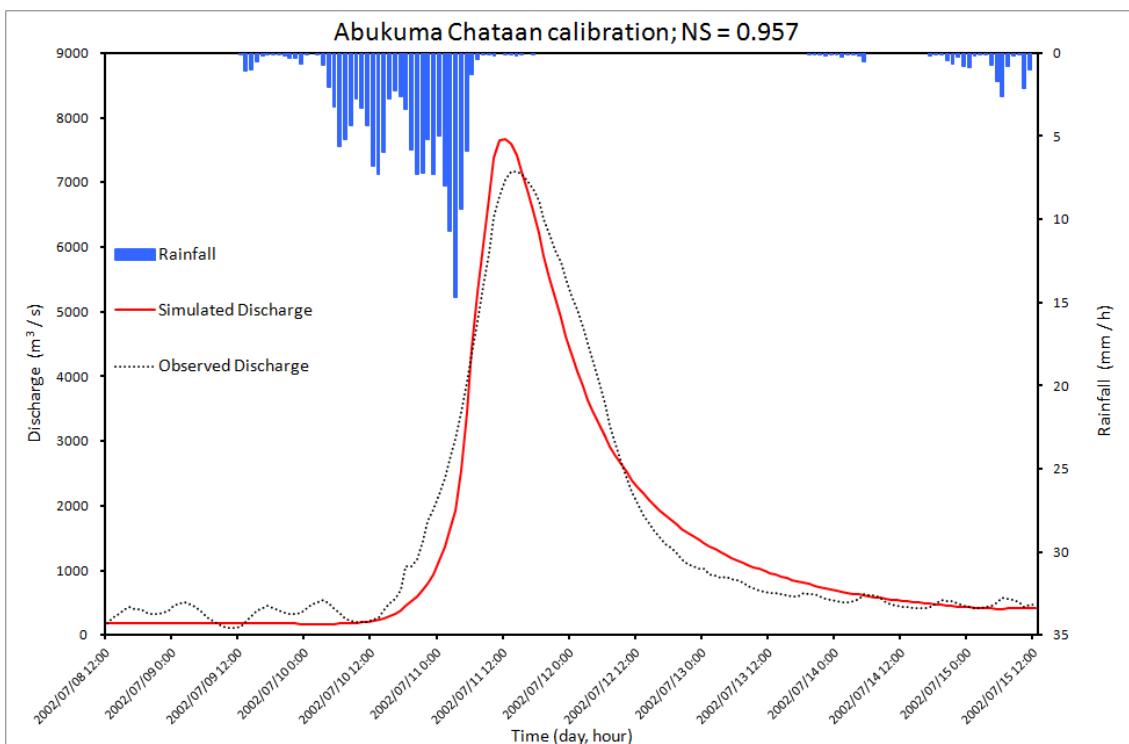


Figure 4.73 Calibrated results for typhoon Chataa (8/07/2002 13:00 - 15/07/2002 12:00)

Table 4.12 Calibrated parameters of the best optimization for typhoon Chataan

Optimized parameters:	
N_slo [$m^{-1/3}s$]	1.000
N_riv [$m^{-1/3}s$]	0.060
ka [ms^{-1}]	0.114
θ_a	0.258
F1	0.664

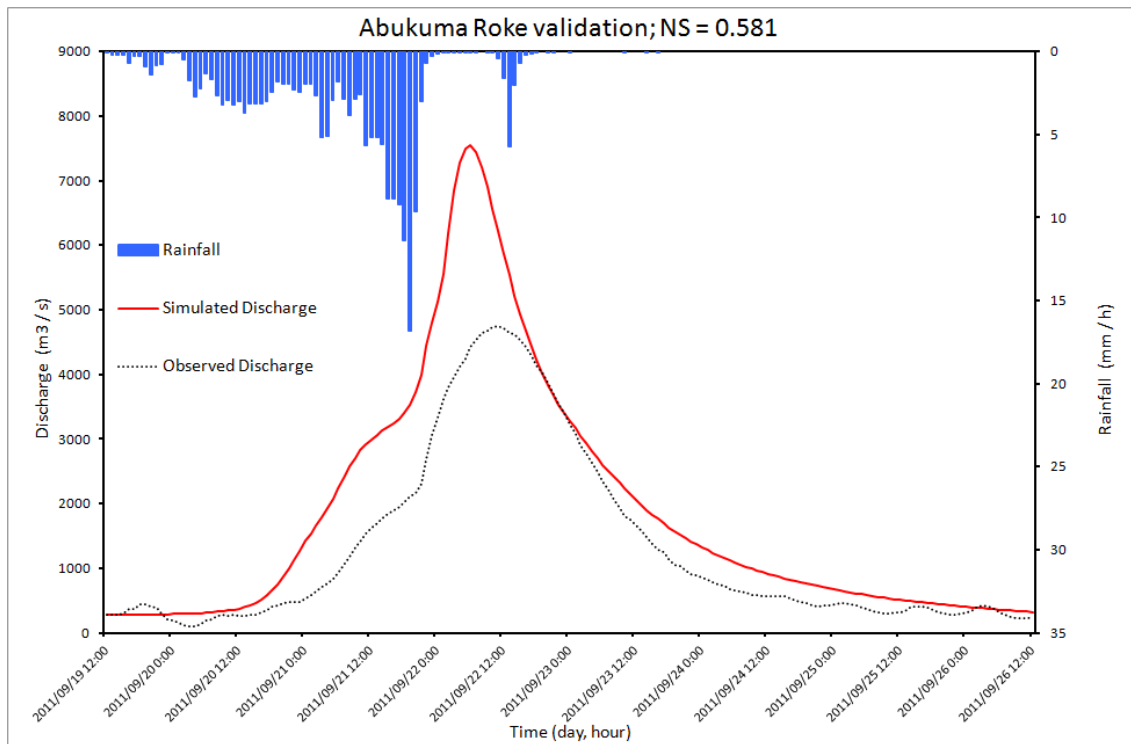


Figure 4.74 Validated results for typhoon Roke (19/09/2011 13:00 - 26/09/2011 12:00)

4.7.7 Kuji

Roke optimization showed better results ($NS = 0.899$ for calibration and for 0.900 validation). Chataan optimization showed $NS = 0.930$ for calibration and 0.797 for validation. Figure 4.75 shows calibrated results for typhoon Roke and Figure 4.76 shows validated results for typhoon Chataan, while Figure 4.77 shows calibrated results for typhoon Chataan and Figure 4.78 shows validated results for typhoon Roke. Table 4.13 shows calibrated parameters of the best optimization for typhoon Roke, and Table 4.14 for typhoon Chataan.

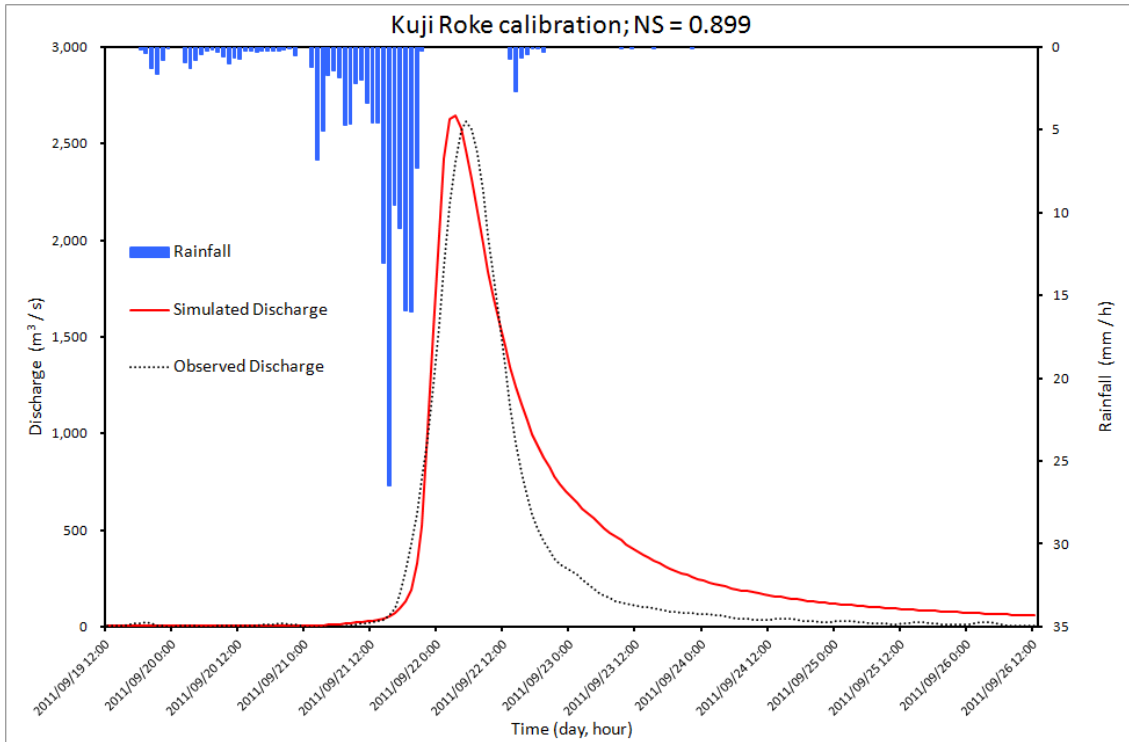


Figure 4.75 Calibrated results for typhoon Roke (19/09/2011 13:00 - 26/09/2011 12:00)

Table 4.13 Calibrated parameters of the best optimization for typhoon Roke

Optimized parameters:	
N_slo [$m^{-1/3}s$]	0.966
N_riv [$m^{-1/3}s$]	0.059
ka [ms^{-1}]	0.100
θ_a	0.257
F1	0.600

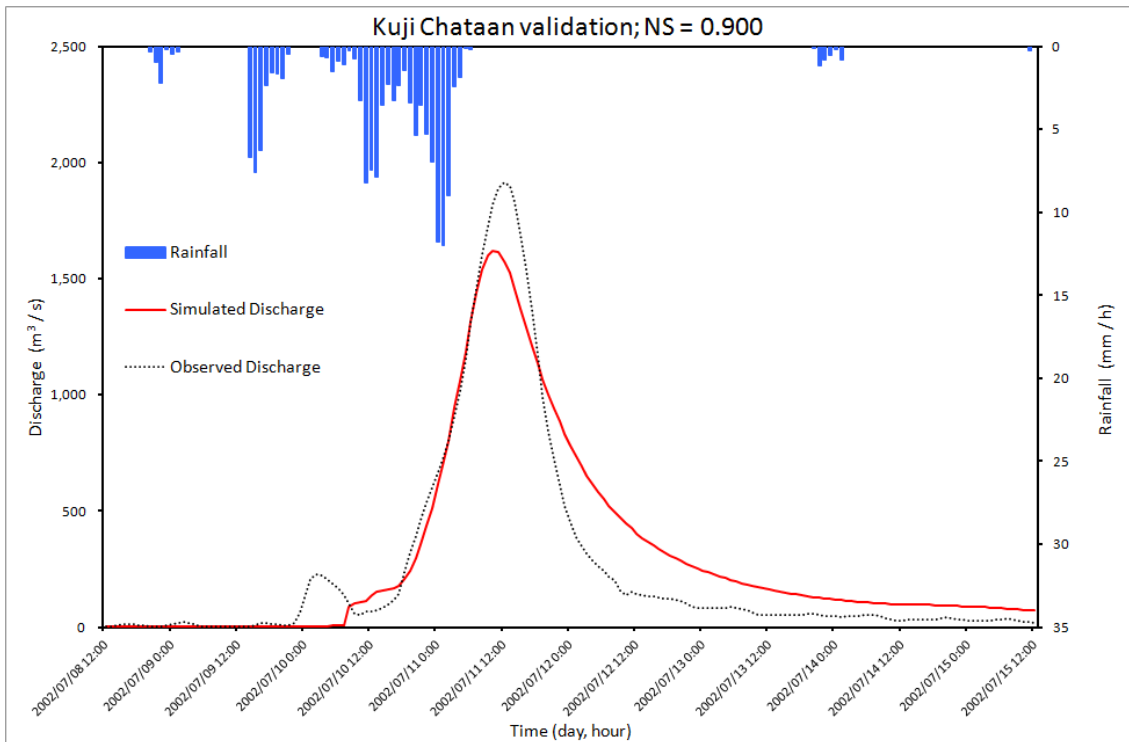


Figure 4.76 Validated results for typhoon Chataan (8/07/2002 13:00 - 15/07/2002 12:00)

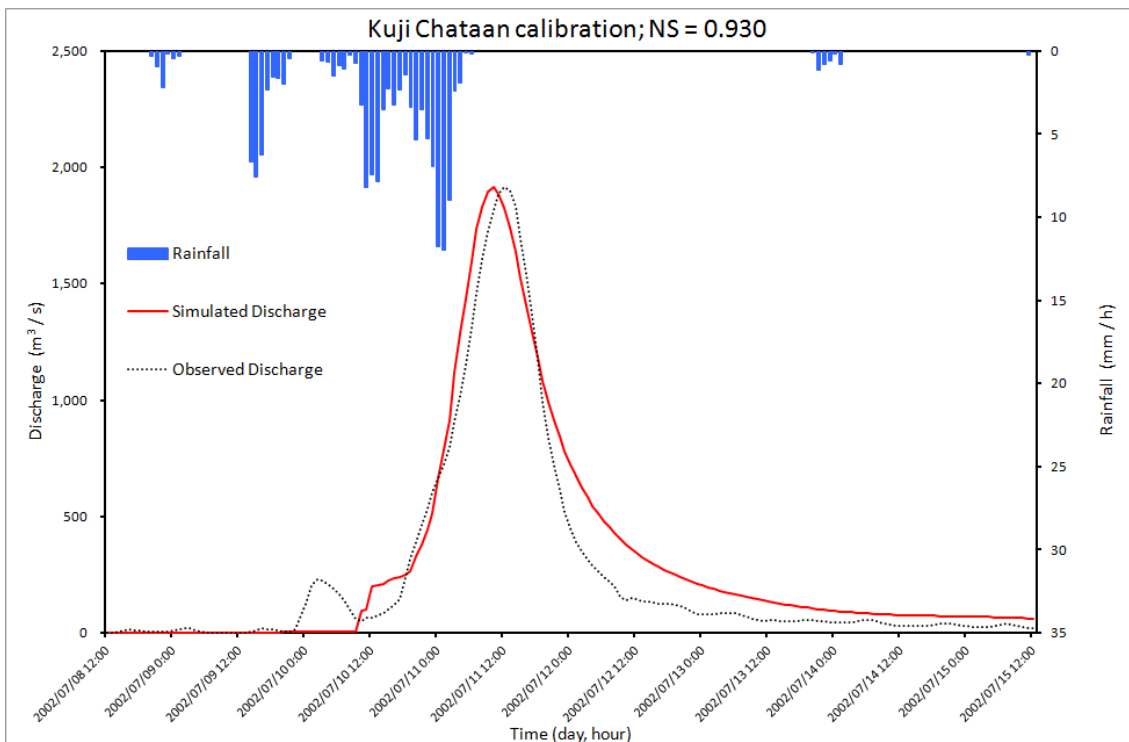


Figure 4.77 Calibrated results for typhoon Chataan (8/07/2002 13:00 - 15/07/2002 12:00)

Table 4.14 Calibrated parameters of the best optimization for typhoon Chataan

Optimized parameters:	
N_slo [$m^{-1/3}s$]	0.269
N_riv [$m^{-1/3}s$]	0.075
ka [ms^{-1}]	0.108
θ_a	0.492
F1	0.600

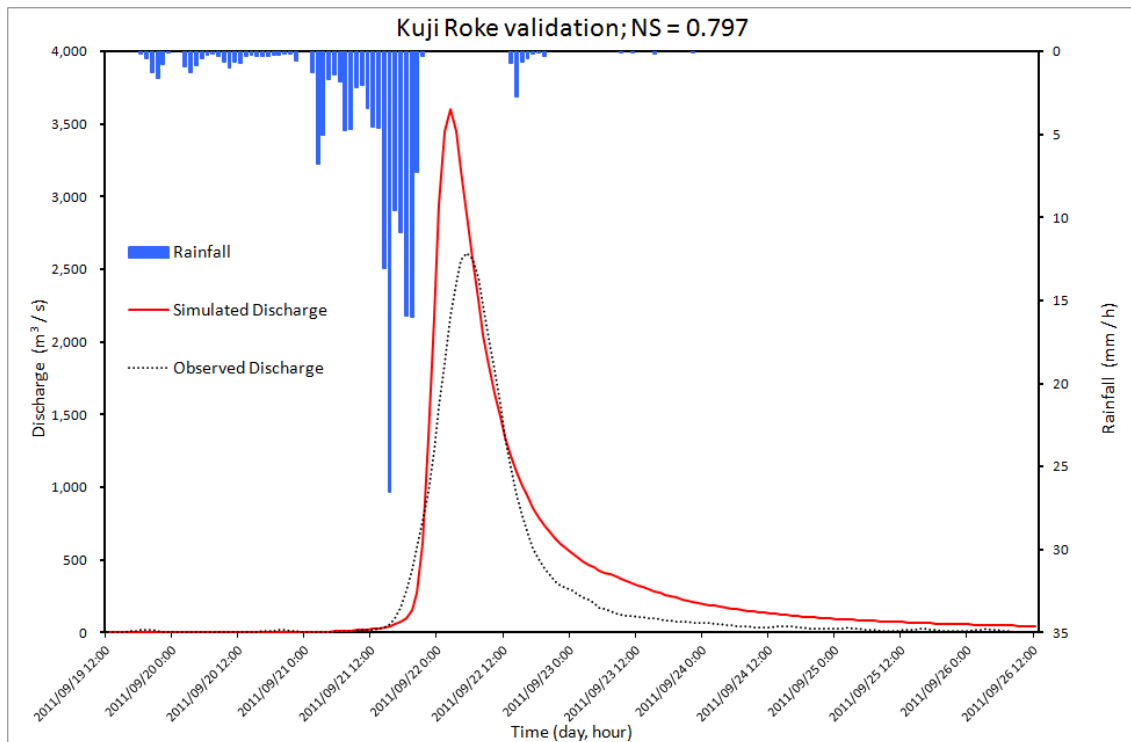


Figure 4.78 Validated results for typhoon Roke (19/09/2011 13:00 - 26/09/2011 12:00)

4.7.8 Naka

Roke optimization showed better results ($NS = 0.971$ for calibration and 0.895 for validation). Chataan optimization showed $NS = 0.876$ for calibration and 0.724 for validation. Figure 4.79 shows calibrated results for typhoon Roke and Figure 4.80 shows validated results for typhoon Chataan, while Figure 4.81 shows calibrated results for typhoon Chataan and Figure 4.82 shows validated results for typhoon Roke. Table 4.15 shows calibrated parameters of the best optimization for typhoon Roke, and Table 4.16 for typhoon Chataan.

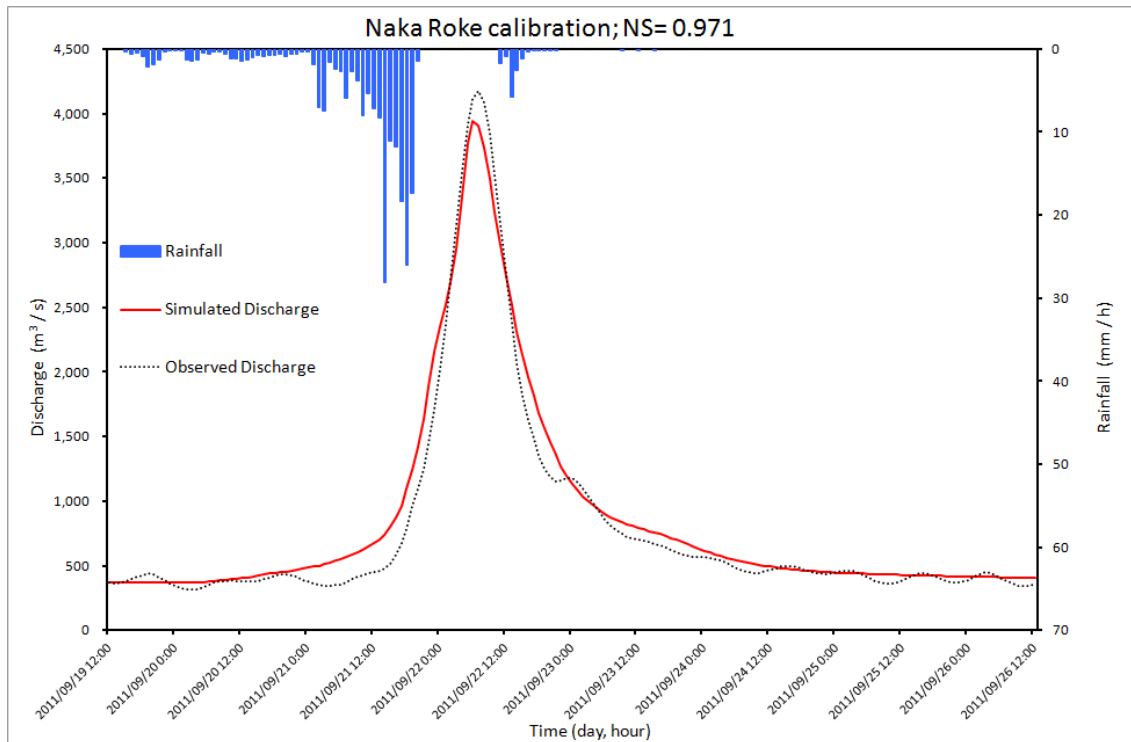


Figure 4.79 Calibrated results for typhoon Roke (19/09/2011 13:00 - 26/09/2011 12:00)

Table 4.15 Calibrated parameters of the best optimization for typhoon Roke

Optimized parameters:	
N_slo [$m^{-1/3}s$]	0.522
N_riv [$m^{-1/3}s$]	0.097
ka [ms^{-1}]	0.665
θ_a	0.005
F1	0.600

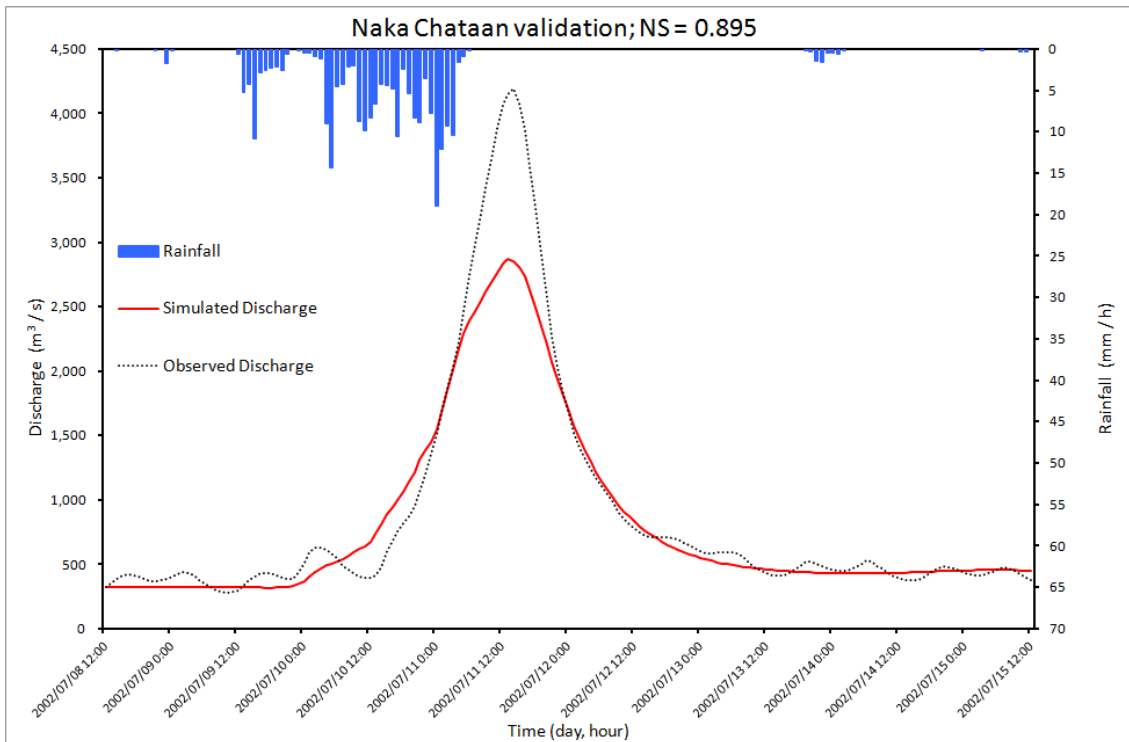


Figure 4.80 Validated results for typhoon Chataan (8/07/2002 13:00 - 15/07/2002 12:00)

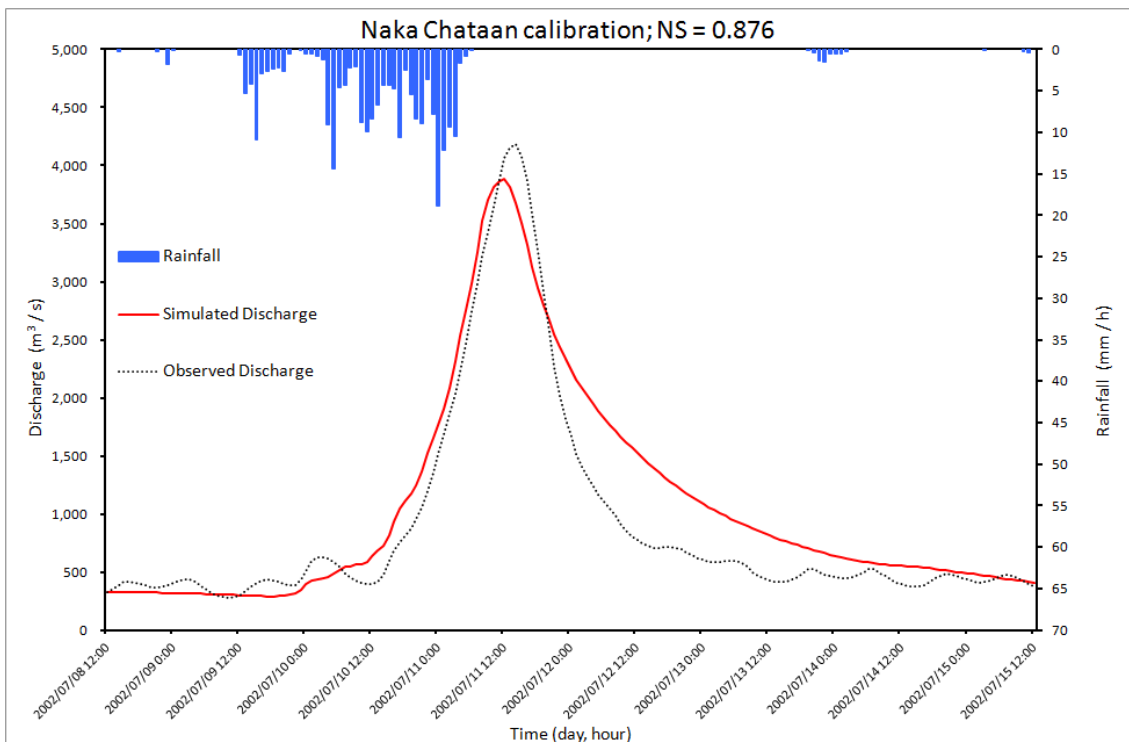


Figure 4.81 Calibrated results for typhoon Chataan (8/07/2002 13:00 - 15/07/2002 12:00)

Table 4.16 Calibrated parameters of the best optimization for typhoon Chataan

Optimized parameters:	
N_slo [$m^{-1/3}s$]	0.100
N_riv [$m^{-1/3}s$]	0.065
ka [ms^{-1}]	0.551
θa	0.499
F1	0.600

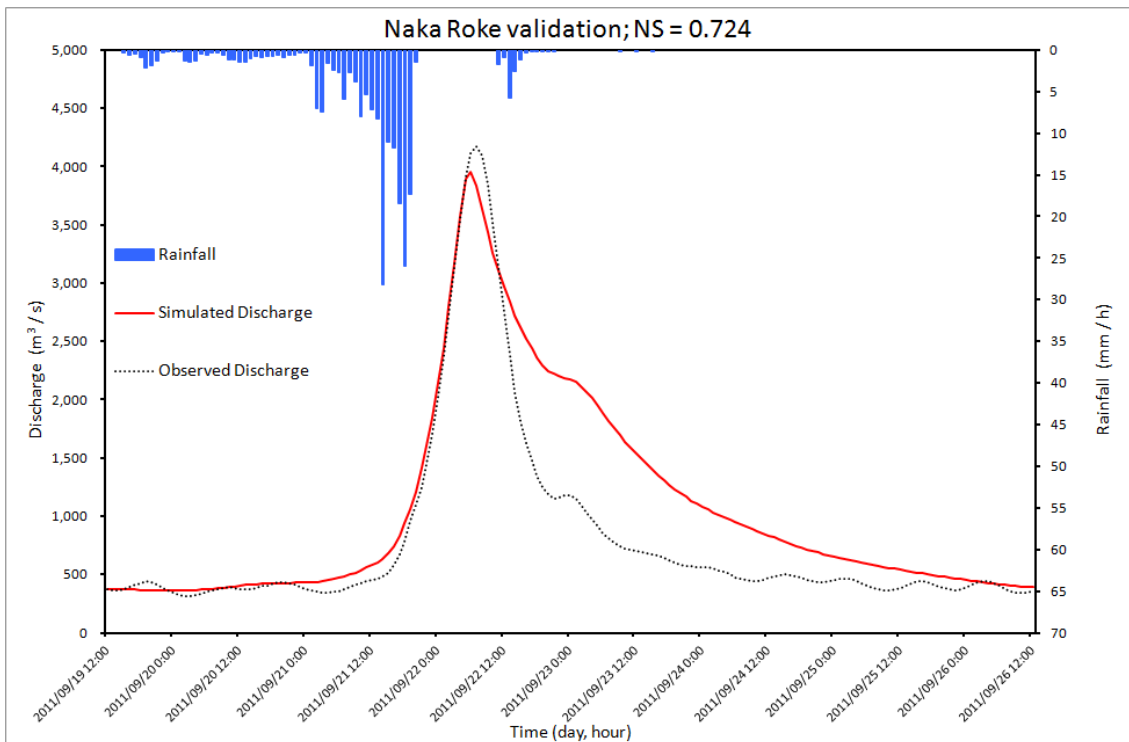


Figure 4.82 Validated results for typhoon Roke (19/09/2011 13:00 - 26/09/2011 12:00)

4.7.9 Tone

Roke optimization showed $NS = 0.967$ for calibration and 0.837 for validation. Chataan optimization showed $NS = 0.920$ for calibration and 0.915 for validation. Figure 4.83 shows calibrated results for typhoon Roke and Figure 4.84 shows validated results for typhoon Chataan, while Figure 4.85 shows calibrated results for typhoon Chataan and Figure 4.86 shows validated results for typhoon Roke. Table 4.17 shows calibrated parameters of the best optimization for typhoon Roke, and Table 4.18 for typhoon Chataan.

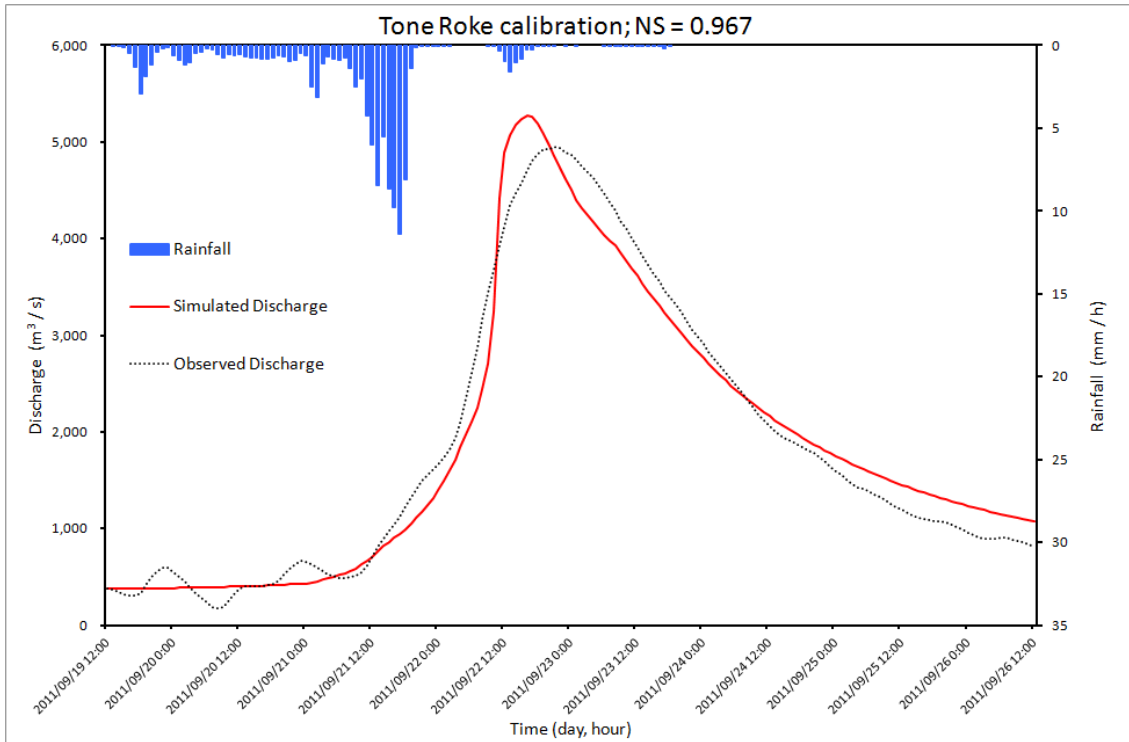


Figure 4.83 Calibrated results for typhoon Roke (19/09/2011 13:00 - 26/09/2011 12:00)

Table 4.17 Calibrated parameters of the best optimization for typhoon Roke

Optimized parameters:	
N_slo [$m^{-1/3}s$]	1.000
N_riv [$m^{-1/3}s$]	0.085
ka [ms^{-1}]	0.147
θ_a	0.045
F1	0.511

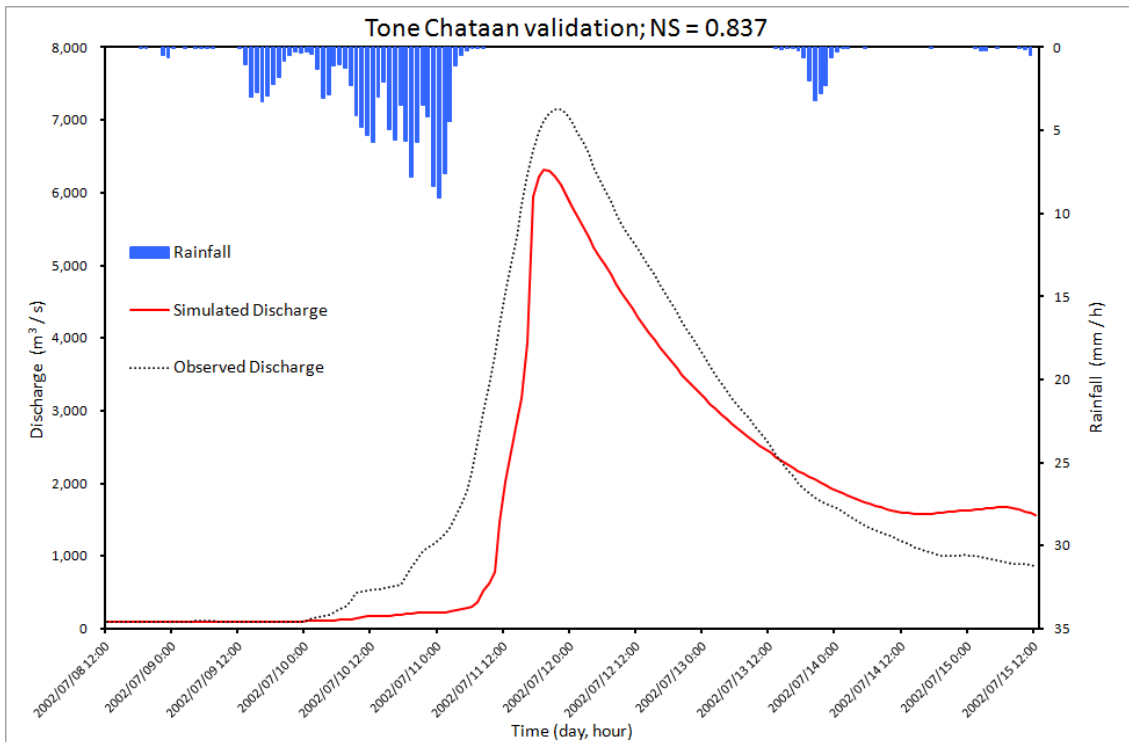


Figure 4.84 Validated results for typhoon Chataan (8/07/2002 13:00 - 15/07/2002 12:00)

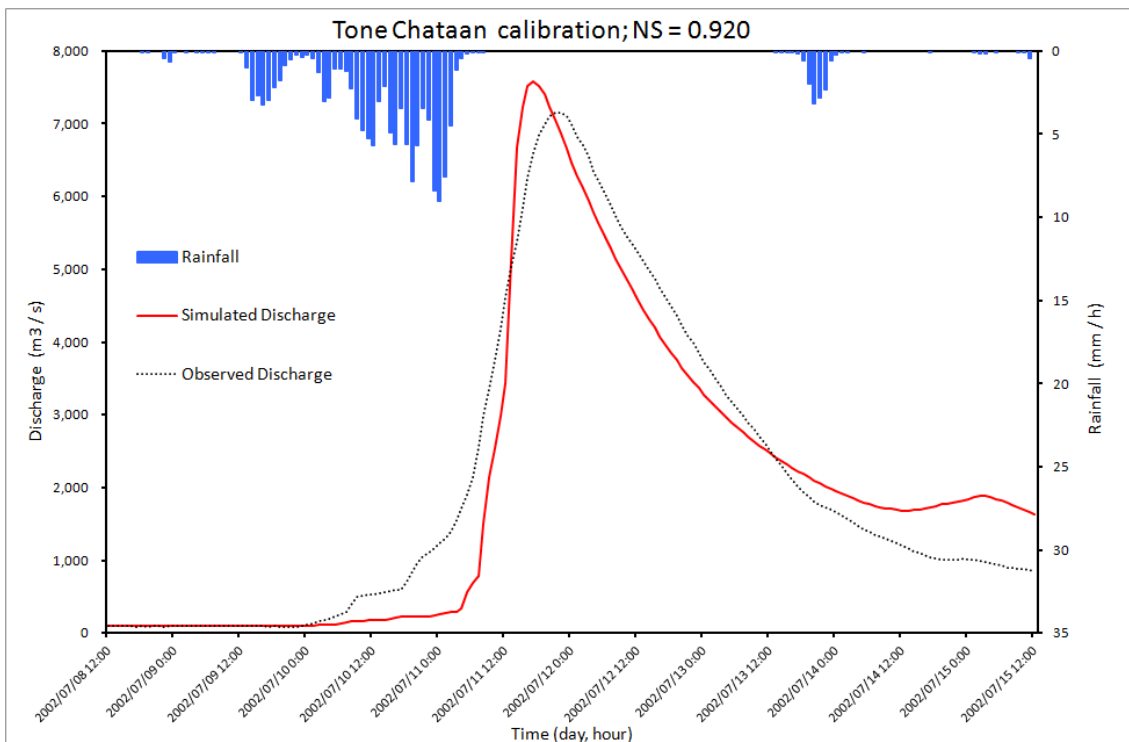


Figure 4.85 Calibrated results for typhoon Chataan (8/07/2002 13:00 - 15/07/2002 12:00)

Table 4.18 Calibrated parameters of the best optimization for typhoon Chataan

Optimized parameters:	
N_slo [$m^{-1/3}s$]	0.999
N_riv [$m^{-1/3}s$]	0.075
ka [ms^{-1}]	0.201
θ_a	0.068
F1	0.568

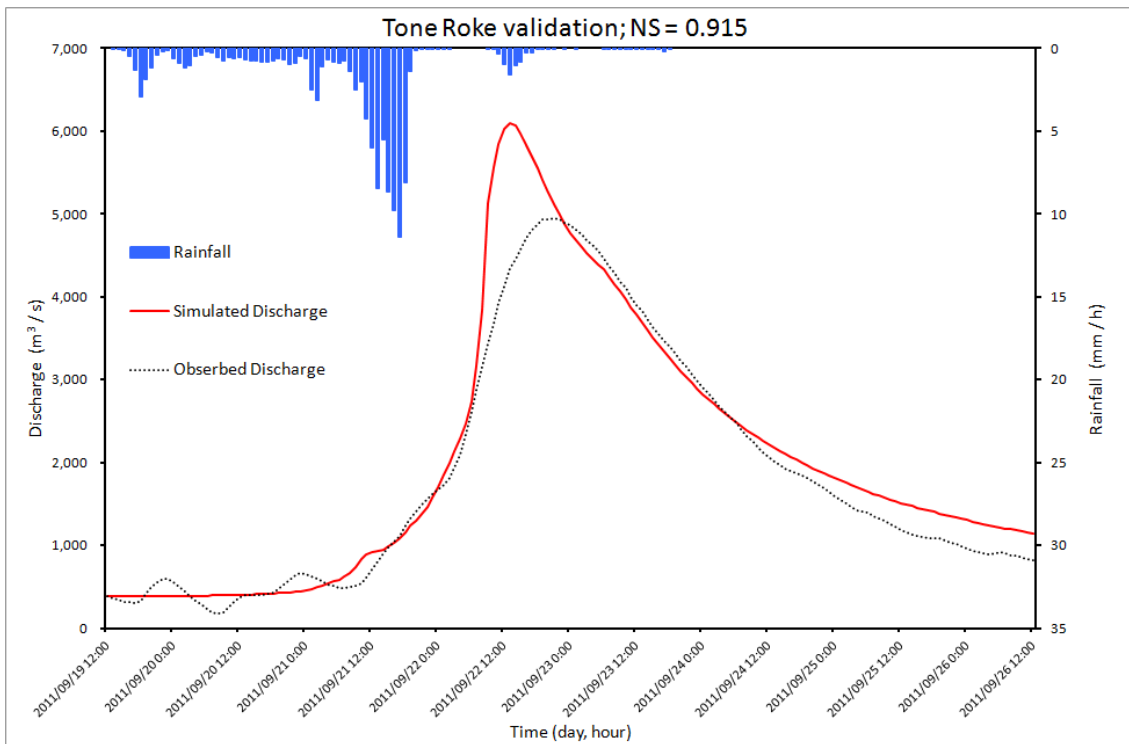


Figure 4.86 Validated results for typhoon Roke (19/09/2011 13:00 - 26/09/2011 12:00)

4.7.10 Total outflow from all basins

We summarized total outflow from all river basins in order to simulate total freshwater budget flowing from eastern Japanese coast to western Pacific ocean during typhoons Roke and Chataan. Roke optimization showed $NS = 0.985$ for calibration and 0.858 for validation while Chataan optimization showed slightly lower results $NS = 0.981$ for calibration and 0.872 for validation. Figure 4.87 shows calibrated results for typhoon Roke and Figure 4.88 shows validated results for typhoon Chataan, while Figure 4.89 shows calibrated results for typhoon Chataan and Figure 4.90 shows validated results for typhoon Roke.

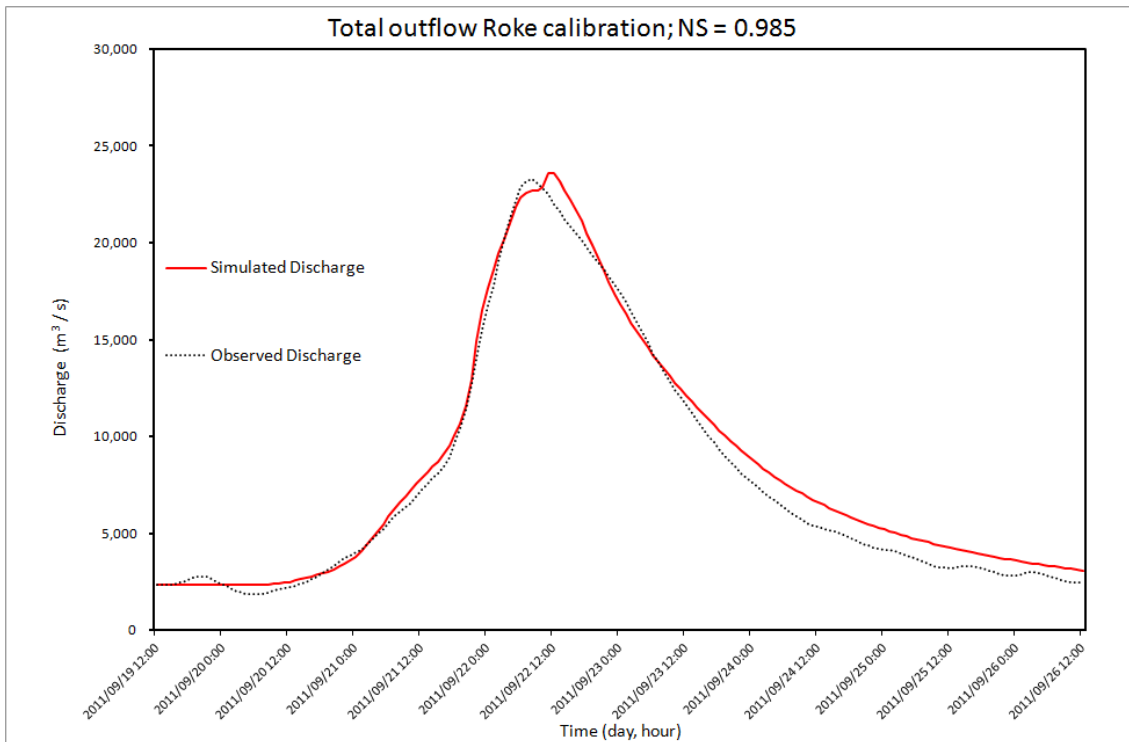


Figure 4.87 Calibrated results for typhoon Roke (19/09/2011 13:00 - 26/09/2011 12:00)

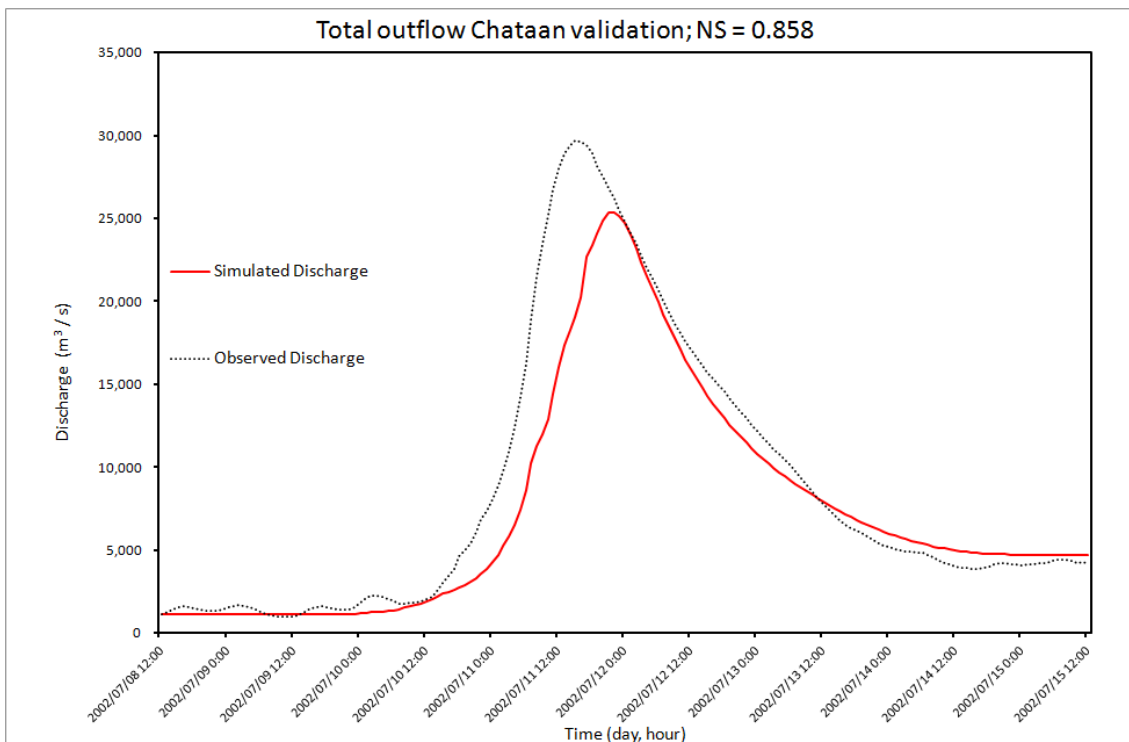


Figure 4.88 Validated results for typhoon Chataan (8/07/2002 13:00 - 15/07/2002 12:00)

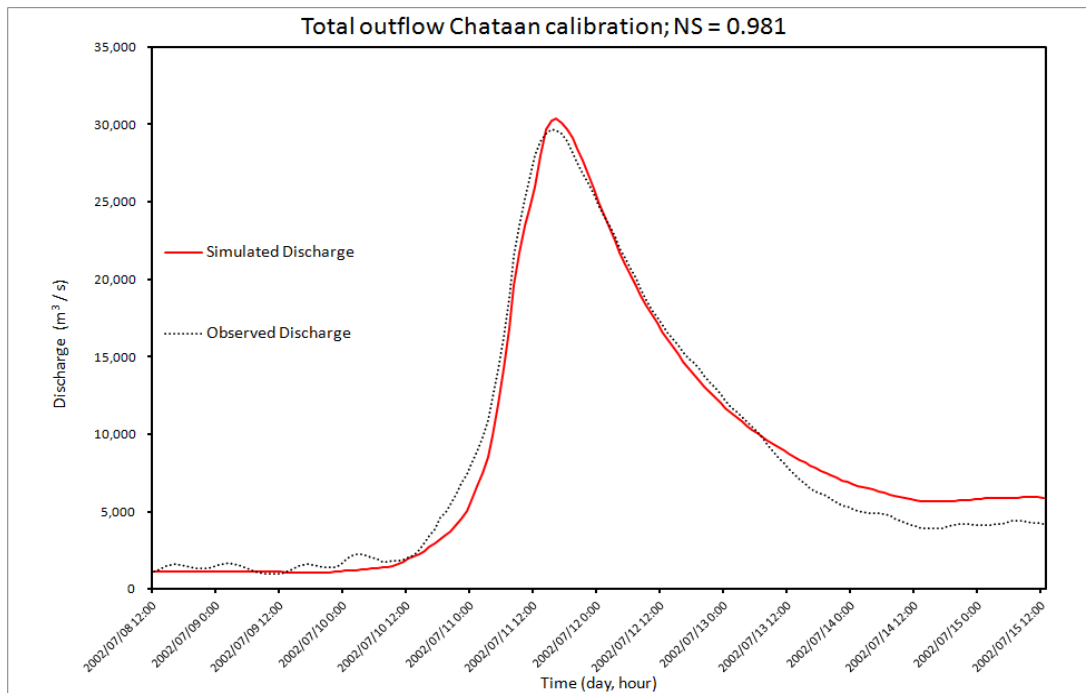


Figure 4.89 Calibrated results for typhoon Chataan (8/07/2002 13:00 - 15/07/2002 12:00)

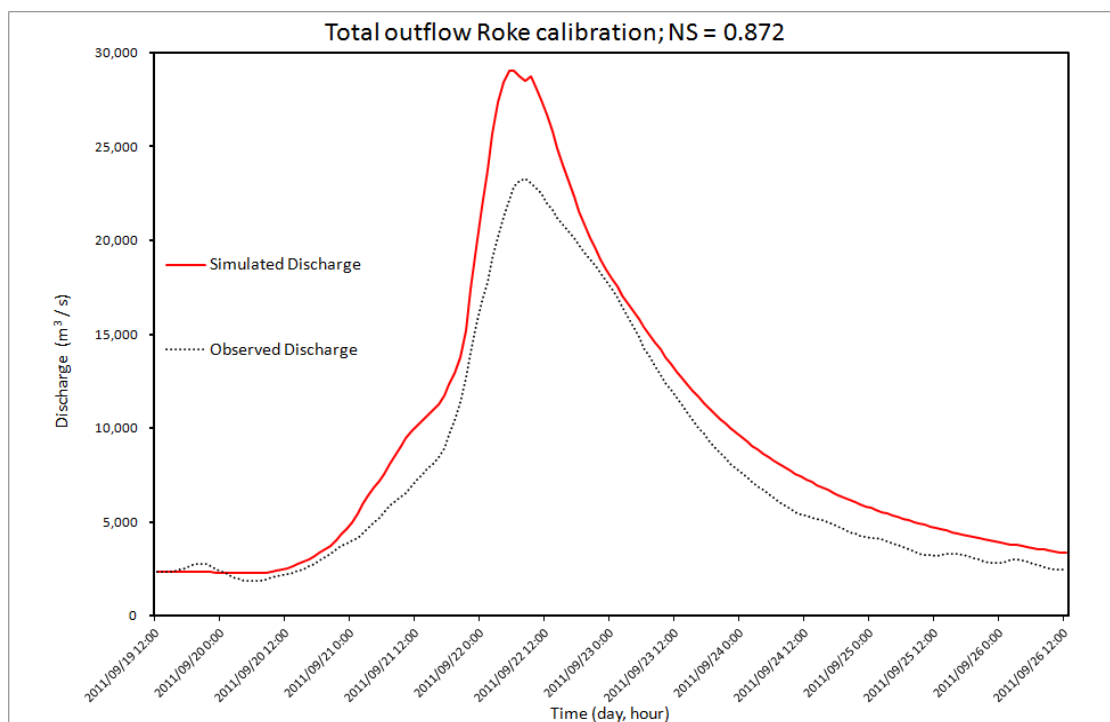


Figure 4.90 Validated results for typhoon Roke (19/09/2011 13:00 - 26/09/2011 12:00)

From the results we can see that maximum total outflow for typhoon Roke reached around 23.000 m³/s while for typhoon Chataan it reached 30.000 m³/s.

4.7.11 Joint hydrological and oceanographic calculation

Two coastal simulations were done, one with using climatological mean monthly discharges as freshwater input from 9 rivers and the other one using our model simulated discharges as a real time freshwater input from 9 rivers. Figure 4.91a shows sea surface salinity (PSU) in JCOPE-T model for September 26, 2011, 22:00 JST for climatological monthly discharges and Figure 4.91b for our model simulated discharges. We may observe significant difference of salinity in near-shore zone between the two cases, extending to almost the whole coast between Sendai bay and Tone river.

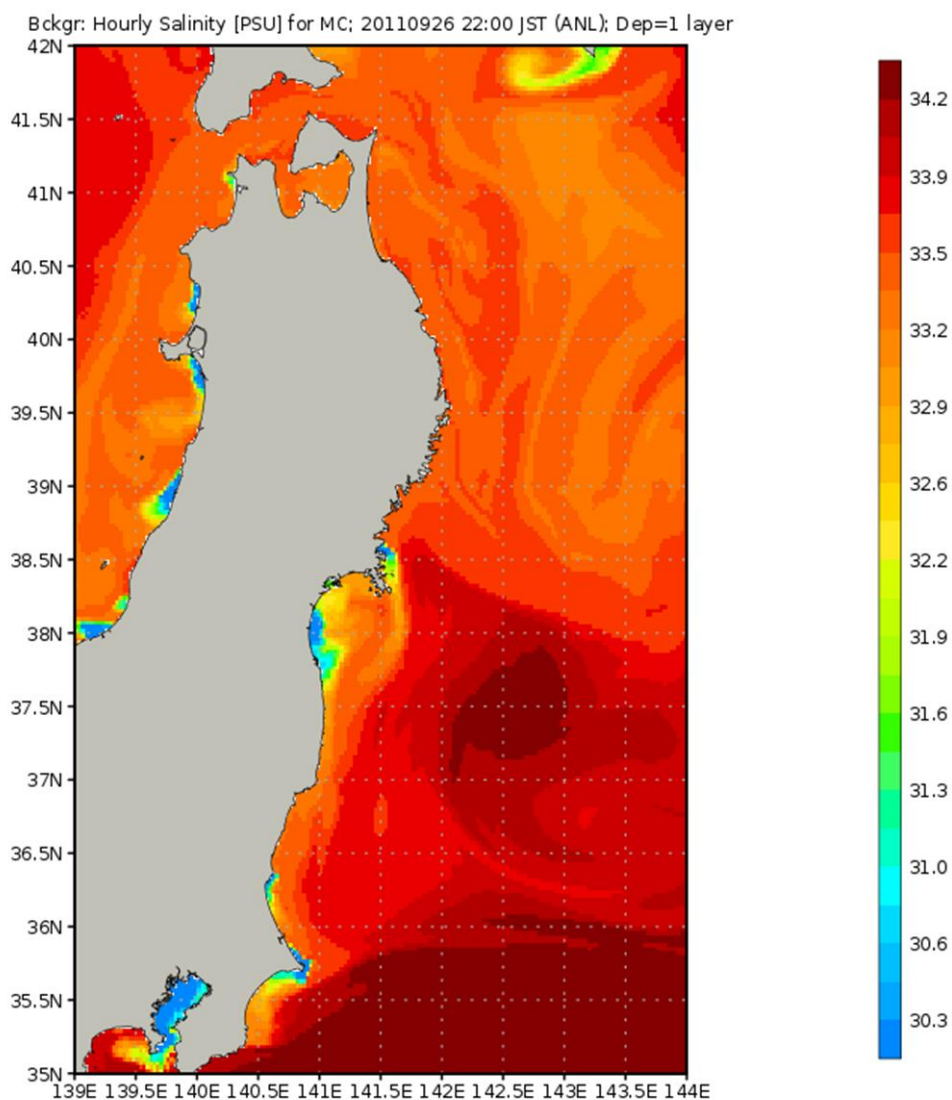


Figure 4.91a Sea surface salinity (PSU) in JCOPE-T model for September 26, 2011, 22:00 JST (climatological monthly discharges)

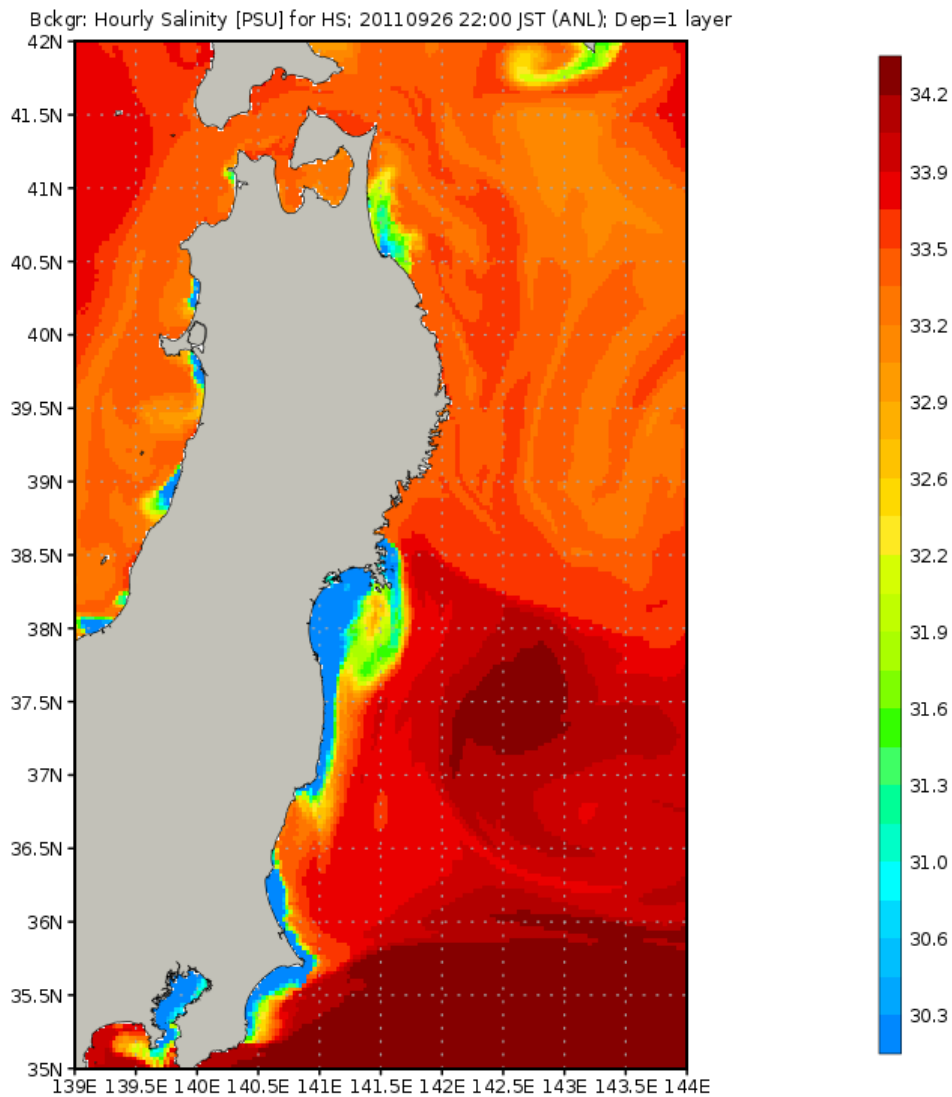


Figure 4.91b Sea surface salinity (PSU) in JCOPE-T model for September 26, 2011, 22:00 JST (our model discharges)

4.8 Conclusions

We found that typhoon Roke (2011) optimization and typhoon Chataan (2002) validation shows better results than Chataan optimization and Roke validation, except for the most northern rivers Mabechi and Takase, and for Tone both showed similar results. For all 9 considered rivers *NS* value for validated event was calculated above 0.7, and for calibrated event above 0.89.

For total river outflow from all basins, calculated Nash-Sutcliffe efficiency was

very high, 0.985 for calibrated typhoon Roke and 0.864 for validated typhoon Chataan, which shows that our model calibrated on typhoon Roke can be successfully used to predict other extreme precipitation events runoff. Results for Chataan calibration and Roke validation came similar but with a little lower value.

Effect of the dam for rivers Abukuma, Kitakami and Tone showed to be minor because dams are usually built in the upstream of the basins.

This study included SCE-UA optimization method which significantly improved calibrated results.

Our calibrated model can be used as nowcasting model for real time prediction of extreme flood events for flood defense disaster prevention management.

The model used in the study has capability of simulating extreme discharge events by optimization, and proper simulation of extreme discharge events can be used to improve coastal and ocean modeling, especially modeling which is sensitive to reproducibility of the salinity distribution in coastal areas, as shown by Figure 4.91b.

By having ability to simulate extreme discharge events at river mouths, the study can be extended to sediment and water quality modeling in coastal areas.

References

- Apip, Sayama T, Tachikawa Y, Takara K. 2011. Spatial lumping of a distributed rainfall-sediment-runoff model and its effective lumping scale, *Hydrological processes*.
- Carton JA. 1991. Effect of seasonal surface freshwater flux on sea surface temperature in the tropical Atlantic ocean, *Journal of geophysical research*.
- Dai A, Qian T, Trenberth KE. 2008. Changes in continental freshwater discharge from 1948-2004, *Journal of climate*.
- Dai A, Trenberth KE. 2003. New estimates of continental discharge and oceanic freshwater transport, *AMS symposium on observing and understanding the variability of water in weather and climate*.
- Dai A, Trenberth KE. 2002. Estimates of freshwater discharge from continents: latitudinal and seasonal variations, *Journal of hydrometeorology*.
- Duan W, Takara K, He B, Luo P, Nover D, Yamashiki Y. 2013. Spatial and temporal trends in estimates of nutrient and suspended sediment loads in the Ishikari river, Japan, 1985 to 2010, *Science of the total environment*.
- ESRI, ArcGIS Desktop: Release 10.2.2. 2016. Redlands, CA: *Environmental Systems Research Institute*.
- Faloon PD, Betts RA. 2006. The impact of climate change on global river flow in HadGEM1 simulations, *Atmospheric Science Letters*, 7, pp. 62-68, doi: 10.1002/asl.133.

- Fekete BM, Vorosmarty CJ. 2002. High-resolution fields of global runoff combining observed river discharge and simulated water balances, *Global biogeochemical cycles*.
- Harada Masayoshi, Mori Makito, Tasai Hideaki, Hiramatsu Kazuaki. 2006. Evaluation of Characteristics of TOPMODEL Parameters using SCE-UA Method, *Sci. Bull. Fac. Agr.*, Kyushu Uni., 61, pp. 261-272.
- Knowles N. 2002. Natural and management influences on freshwater inflows and salinity in the San Francisco Estuary at monthly to interannual scales, *Water Resources Research*, Vol. 38, No. 12, 1289, doi: 10.1029/2001WR000360.
- Kojima T, Takara K, Oka T, Chitose T. 1998. Resolution influence on the flood runoff analysis result of raster spatial information, *Water Engineering Papers*, Vol. 42, pp.157-162.
- Luo P, He B, Takara K, Razafindrabe BHN, Nover D, Yamashiki Y. 2011. Spatiotemporal trend analysis of recent river water quality conditions in Japan, *Journal of environmental monitoring*.
- Luo P, Takara K, Apip, He B, Nover D. 2014. Palaeoflood simulation of the Kamo river basin using a grid-cell distributed rainfall run-off model, *Journal of Flood Risk Management*, doi: 10.1111/jfr3.12038.
- Miller JR, Russel GL, Caliri G. 1994. Continental-scale river flow in climate models, *Journal of climate*.
- Milliman JD, Farnsworth KL, Jones PD, Xu KH, Smith LC. 2008. Climatic and anthropogenic factors affecting river discharge to the global ocean, 1951-2000, *Global and planetary change* 62 (3-4), pp. 187-194.
- Nash JE, Sutcliffe JV. 1970. River flow forecasting through conceptual models part1- a discussion of principles, *Journal of Hydrology*, Vol.10, pp. 282-290.
- Sasaki, T. 2014. A study on the method for analysis of radioactive cesium amount of Abukuma basin by distributed runoff model, unpublished
- Sayama, T and McDonell, JJ. 2009. A new time-space accounting scheme to predict stream water residence time and hydrograph source components at the watershed scale, *Water Resources Research*, 45, W07401, doi: 10.1029/2008WR007549.
- Shiklomanov IA. 2009. River runoff to oceans and lakes, *Hydrological cycle Vol II*.
- Tachikawa Y, Nagatani G, Takara K. 2004. The development of the flow stream product relationship that mechanism was introduced in the saturated or unsaturated flow, *Water Engineering Papers*, Vol. 48, pp.7-12.
- Talley LD. 2002. Salinity patterns in the ocean, *Encyclopedia of global environmental change*.
- Urakawa LS, Kurogi M, Yoshimura K, Hasumi H. 2015. Modeling low salinity waters

along the coast around Japan using a high-resolution river discharge dataset, *Journal of Oceanography* 71, pp. 715-739, doi: 10.1007/s10872-015-0314-4.

Varlamov SM, Guo X, Miyama T, Ichikawa K, Waseda T, Miyazawa Y. 2015. M2 baroclinic tide variability modulated by the ocean circulation south of Japan, *Journal of Geophysical Research*, doi:10.1002/2015JC010739.

Vijai Gupta, Qingyun Duan, Soroosh Sorooshian. 1992. Effective and Efficient Global Optimization for Conceptual Rainfall-Runoff Models, *Water Resources Research*, Vol.28, pp. 1015-1031, April.

Vijai Gupta, Qingyun Duan, Soroosh Sorooshian. 1993. Calibration of Rainfall-Runoff Models Application of Global Optimization to the Sacramento Soil Moisture Accounting Model, *Water Resources Research*, Vol.29, pp. 1185-1194.

Vijai Gupta, Qingyun Duan, Soroosh Sorooshian. 1994 Optimal use of the SCE-UA global optimization method for calibrating watershed models, *Journal of Hydrology*, Vol.158, pp. 265-284.

www.data.jma.go.jp/risk/obsdl/index.php#

www.flood.dpri.kyoto-u.ac.jp/previous_page/product/cellModel/cellModel.html

www.hydrosheds.cr.usgs.gov/index.php

www1.river.go.jp

Chapter 5 - Conclusions and future challenges

The doctoral thesis is composed of two major new contributions.

One contribution of the thesis (Chapter 3) is giving comprehensive overview of fluvial influence on estuarine sediment transport processes in order to introduce a new parameter, vertically differentiated unidirectional freshwater flux dQ , as a driving mechanism for suspended sediment transport in estuaries for high discharges in combination with occurrence of salt wedge.

The other contribution is linkage of fluvial outflow data to coastal modeling (Chapter 4) and including fluvial influence together with joint hydrological-oceanographic model in order to get more realistic salinity distribution results in coastal zone. The model used in the study has capability of simulating extreme discharge events by optimization.

Both contributions have in common fluvial influence on estuarine and coastal processes. The fluvial influence on estuarine and coastal processes is often neglected in oceanographic modeling due to its specific micro scale characteristics which make them hard to couple with macro scale characteristics of oceanographic modeling. We tried to challenge that problem and offer a feasible ways how the fluvial influence can be included in estuarine and coastal modeling. In Chapter 4 we applied joint hydrological-oceanographic modeling and found that surface salinity differences in coastal zone of Japan were significant after the typhoon Roke event. That finding shows the importance of including fluvial outflow to joint hydrological-oceanographic modeling because a river may affect a salinity distribution in a coastal region far away from its mouth. In Chapter 3 we focused on observed turbidity distributions in vicinity of river mouth and tried to find specific mechanism of suspended sediment transport which led to such an unexpected distribution. We found a new mechanism, named dQ , whose application showed good correlations with the observed turbidity distributions, so we proposed the dQ mechanism as an innovative way to approximate suspended sediment distributions in the middle of the water column for high discharges.

While in Chapter 4 we focused on hydrological and joint hydrological-oceanographic modeling of the watershed and coastal zone, in Chapter 3 we focused on hydrodynamic modeling and suspended sediment transport, in total giving a comprehensive overview of fluvial influence to processes occurring in estuarine and coastal zone.

In Chapter 3 we neglected tidal effects due to limitations of the model and our

goal to consider fluvial influence to ocean circulation. That assumption can be neglected in future studies in order to get more realistic physical processes in estuarine sediment transport. We provided comprehensive theoretical and qualitative analysis of the dQ phenomena but the study is also missing quantitative approach towards the linkage with suspended sediment transport.

By applying findings from the Chapter 4 to estuarine, coastal and in bigger scale climatological modeling, we can get more comprehensive meteorology, hydrology and oceanographic cycle, which is at this point unsolved the most often due to neglected connection between hydrologic and oceanographic cycle. Our calibrated model can be used as nowcasting model for real time prediction of extreme flood events for flood defense disaster prevention management. The study can also be extended to more rivers basins, hopefully including the whole Japanese coast, but can also be applied worldwide. The study can also be extended to sediment and water quality modeling in coastal areas, which would have environmental impact on flora and fauna in the nearshore zone, where is the most important environmental zone for people living close to estuaries, and any potential environmental disaster in that zone can consequently cause undesirable social and economical costs.